

Forschungsbericht 2022-05

Aerodynamic Design of Active Flow Control on the Vertical Tail

Anna Gebhardt

Deutsches Zentrum für Luft- und Raumfahrt
Institut für Aerodynamik und
Strömungstechnik
Braunschweig



**Deutsches Zentrum
DLR für Luft- und Raumfahrt**

Forschungsbericht 2022-05

Aerodynamic Design of Active Flow Control on the Vertical Tail

Anna Gebhardt

Deutsches Zentrum für Luft- und Raumfahrt
Institut für Aerodynamik und
Strömungstechnik
Braunschweig

106 Seiten
88 Bilder
2 Tabellen
101 Literaturstellen



Deutsches Zentrum
DLR für Luft- und Raumfahrt



Herausgeber:


Deutsches Zentrum
für Luft- und Raumfahrt e. V.
Wissenschaftliche Information
Linder Höhe
D-51147 Köln

ISSN 1434-8454
ISRN DLR-FB-2022-05


DOI: <https://doi.org/10.57676/5sz4-jw56>

Erklärung des Herausgebers

Dieses Werk ist unter einer Creative Commons Lizenz vom Typ Namensnennung – Nicht kommerziell – Weitergabe unter gleichen Bedingungen 3.0 Deutschland zugänglich.

 Um eine Kopie dieser Lizenz einzusehen, konsultieren Sie bitte <https://creativecommons.org/licenses/by-nc-sa/3.0/legalcode> oder wenden Sie sich brieflich an Creative Commons, Postfach 1866, Mountain View, California, 94042, USA.

Lizenz

 Creative Commons Lizenz vom Typ Namensnennung - Nicht kommerziell – Weitergabe unter gleichen Bedingungen 3.0 Deutschland

Active Strömungskontrolle, Aerodynamischer Entwurf, Seitenleitwerk

Anna GEBHARDT

DLR, Institut für Aerodynamik und Strömungstechnik, Braunschweig

***Entwurf von aktiver Strömungskontrolle an einem Seitenleitwerk
Dissertation Technische Universität Braunschweig***

In dieser Arbeit wird aktive Strömungskontrolle mit tangentialem Ausblasen untersucht, um die Strömungsablösung am Seitenleitwerk (SLW) eines modernen Passagierflugzeugs zu verzögern. Während die Effektivität von tangentialem Ausblasen an Flügelgeometrien bekannt ist, ist das Ziel dieser Arbeit der Entwurf des aerodynamischen Anteils eines Ausblausystems um zwei Dinge zu zeigen: Tangentiales Ausblasen kann auch an einem SLW effektiv sein und die Effizienz kann erhöht werden, wenn sich der Schlitz nicht über die gesamte Spannweite erstreckt. Der numerisch durchgeführte Entwurf basiert auf den Reynolds-gemittelten Navier-Stokes Gleichungen. Der Entwurfsfall für die Fläche des SLWs ist ein einseitiger Triebwerksausfall im Langsamflug bei kleinen bis mittleren Schiebewinkeln. Zum Ausgleich des asymmetrischen Schubs wird ein großer Ruderausschlag benötigt, um die notwendige hohe Seitenkraft zu erzeugen. Das Ziel ist hier die Erhöhung der Seitenkraft durch Verzögerung der Strömungsablösung, um die Seitenleitwerksfläche auf die Anforderungen für den Reiseflug reduzieren zu können und damit Widerstand sowie Gewicht einzusparen. Der erwähnte Entwurfsfall führt zu einem nicht linearen aerodynamischen Verhalten aufgrund teilweiser Strömungsablösung. Dieses unterscheidet sich von dem einer typischen Verkehrsflugzeug-Flügelgeometrie aufgrund der kleinen Streckung und hohen Pfeilung des SLWs.

Daher ist das Verständnis der zugrundeliegenden komplexen dreidimensionalen Strömung um das SLW die Basis dieser Arbeit. Darauf aufbauend wird der tangentielle Schlitz in drei Schritten entwickelt. Zuerst werden an einem 2D-Profil die Effekte von geometrischen Änderungen im Schlitzbereich untersucht. Im nächsten Schritt wird dies zu einer 2,5D-Geometrie erweitert, die eine konstante Profiltiefe und eine Ausdehnung in Spannweitenrichtung hat. Damit können zusätzlich zu einem durchgehenden Schlitz diskrete Schlitze und der große Pfeilwinkel des SLW berücksichtigt werden. Diese führen zur Erzeugung eines Wirbelsystems über dem Ruder, welches hilft die Strömung nicht nur im Pfad des Strahls sondern auch dazwischen in Spannweitenrichtung anliegend zu halten. Zur Optimierung des Wirbelsystems werden die Schlitzbreite und der Abstand zwischen den Schlitzen variiert. In einem letzten Schritt werden die gewonnenen Erkenntnisse auf das 3D-Seitenleitwerk übertragen. Durch die Verringerung der spannwitigen Schlitzausdehnung konnte eine erhebliche Einsparung im Massenstrom von etwa 50% für die gleiche Erhöhung des Seitenkraftbeiwerts erreicht werden. Es konnte also gezeigt werden, dass der Seitenkraftbeiwert durch tangentiales Ausblasen signifikant erhöht werden kann, wobei dies mit diskreten Schlitzen effizienter möglich ist.

Active Flow Control, Aerodynamic Design, Vertical Tail

(Published in English)

Anna GEBHARDT

DLR, Institute of Aerodynamics and Flow Technology, Braunschweig

***Aerodynamic Design of Active Flow Control on the Vertical Tail
Doctoral Thesis Technische Universität Braunschweig***

In this work the application of active flow control with tangential blowing is investigated to delay flow separation on the vertical tailplane (VTP) of a modern passenger transport aircraft. While tangential blowing is known to be effective on wing geometries, the aim of this work is to design the aerodynamic part of a blowing system in order to show two things: That tangential blowing can be effective on a VTP as well and that its efficiency can be increased when deviating from a full span slot. The design is done using numerical methods based on the Reynolds-averaged Navier-Stokes equations. The sizing case for the area of the VTP is a one-sided engine failure at low speed accompanied by small-to-medium sideslip angles. To compensate the asymmetric thrust, a large rudder deflection is needed to achieve the high side force required. The objective here is to increase the side force by delaying the flow separation to allow reducing the VTP area to cruise flight requirements, saving drag and weight. The design case mentioned leads to non-linear aerodynamic characteristics caused by partial flow separation. These differ from a typical passenger aircraft wing geometry due to the VTP's low-aspect ratio, highly-swept planform.

Therefore, understanding the complex three-dimensional baseline flow over the VTP is the basis of this work. Building on this, the tangential blowing slot is developed in three steps. First, a 2D section is used to analyze the effects of geometry changes in the vicinity of the slot. In a next step this geometry is extended to 2.5D where a constant chord geometry with extension in spanwise direction is used. This allows accounting for the large sweep angle of the VTP and opens the possibility to examine apart from a continuous full span slot also discrete slots. Introducing the discrete slots leads to the creation of a vortex system over the rudder which helps to attach the flow not only in the path of the jet but also in between the jets in spanwise direction. The slot width and the gap between the slots are varied to optimize this vortex system. The findings were in a last step transferred to the 3D vertical tailplane. Due to the reduction of the slot extension over the span a considerable mass flow reduction of around 50% could be achieved for the same increase in side force coefficient. Thus it could be shown that the side force coefficient can be significantly increased using tangential blowing which is more efficient when using discrete slots.

TU Braunschweig – Niedersächsisches
Forschungszentrum für Luftfahrt

Berichte aus der Luft- und Raumfahrttechnik

Forschungsbericht 2022-08

**Aerodynamic Design of Active Flow Control
on the Vertical Tail**

Anna Gebhardt

Deutsches Zentrum für Luft- und Raumfahrt
Institut für Aerodynamik und Strömungstechnik
Braunschweig

Diese Veröffentlichung wird gleichzeitig in der Berichtsreihe „NFL - Forschungsberichte“ geführt.

Diese Arbeit erscheint gleichzeitig als von der Fakultät für Maschinenbau der Technischen Universität Carolo-Wilhelmina zu Braunschweig zur Erlangung des akademischen Grades einer Doktor-Ingenieurin genehmigte Dissertation.

Aerodynamic Design of Active Flow Control on the Vertical Tail

Von der Fakultät für Maschinenbau
der Technischen Universität Carolo-Wilhelmina zu Braunschweig

zur Erlangung der Würde
einer Doktor-Ingenieurin (Dr.-Ing.)
genehmigte Dissertation

von:	Anna Gebhardt
geboren in:	Halle (Saale)
eingereicht am:	18.03.2021
mündliche Prüfung am:	01.12.2021
Vorsitz:	Prof. Dr.-Ing. Ali Elham
Gutachter:	Prof. Dr.-Ing. Ralf Rudnik Prof. Dr.-Ing. Rolf Radespiel

Aerodynamic Design of Active Flow Control on the Vertical Tail

Deutsches Zentrum
für Luft und Raumfahrt e.V.

Institut für Aerodynamik und Strömungstechnik
Abteilung Transportflugzeuge
Lilienthalplatz 7, 38108 Braunschweig

Weyhe, im April 2022

Institutsdirektor:
Prof. Dr.-Ing. habil. C.-C. Rossow

Verfasser:
A. Gebhardt

Abteilungsleiter:
Prof. Dr.-Ing. R. Rudnik

Aerodynamic Design of Active Flow Control on the Vertical Tail

Abstract

In this work the application of active flow control with tangential blowing is investigated to delay flow separation on the vertical tailplane (VTP) of a modern passenger transport aircraft. While tangential blowing is known to be effective on wing geometries, the aim of this work is to design the aerodynamic part of a blowing system in order to show two things: That tangential blowing can be effective on a VTP as well and that its efficiency can be increased when deviating from a full span slot. The design is done using numerical methods based on the Reynolds-averaged Navier-Stokes equations. The sizing case for the area of the VTP is a one-sided engine failure at low speed accompanied by small-to-medium sideslip angles. To compensate the asymmetric thrust, a large rudder deflection is needed to achieve the high side force required. The objective here is to increase the side force by delaying the flow separation to allow reducing the VTP area to cruise flight requirements, saving drag and weight. The design case mentioned leads to non-linear aerodynamic characteristics caused by partial flow separation. These differ from a typical passenger aircraft wing geometry due to the VTP's low-aspect ratio, highly-swept planform.

Therefore, understanding the complex three-dimensional baseline flow over the VTP is the basis of this work. Building on this, the tangential blowing slot is developed in three steps. First, a 2D section is used to analyze the effects of geometry changes in the vicinity of the slot. In a next step this geometry is extended to 2.5D where a constant chord geometry with extension in spanwise direction is used. This allows accounting for the large sweep angle of the VTP and opens the possibility to examine apart from a continuous full span slot also discrete slots. Introducing the discrete slots leads to the creation of a vortex system over the rudder which helps to attach the flow not only in the path of the jet but also in between the jets in spanwise direction. The slot width and the gap between the slots are varied to optimize this vortex system. The findings were in a last step transferred to the 3D vertical tailplane. Due to the reduction of the slot extension over the span a considerable mass flow reduction of around 50% could be achieved for the same increase in side force coefficient. Thus it could be shown that the side force coefficient can be significantly increased using tangential blowing which is more efficient when using discrete slots.

Aerodynamischer Entwurf von aktiver Strömungskontrolle an einem Seitenleitwerk

Zusammenfassung

In dieser Arbeit wird aktive Strömungskontrolle mit tangenalem Ausblasen untersucht, um die Strömungsablösung am Seitenleitwerk (SLW) eines modernen Passagierflugzeugs zu verzögern. Während die Effektivität von tangenalem Ausblasen an Flügelgeometrien bekannt ist, ist das Ziel dieser Arbeit der Entwurf des aerodynamischen Anteils eines Ausblassystems um zwei Dinge zu zeigen: Tangentiales Ausblasen kann auch an einem SLW effektiv sein und die Effizienz kann erhöht werden, wenn sich der Schlitz nicht über die gesamte Spannweite erstreckt. Der numerisch durchgeführte Entwurf basiert auf den Reynolds-gemittelten Navier-Stokes Gleichungen. Der Entwurfsfall für die Fläche des SLWs ist ein einseitiger Triebwerksausfall im Langsamflug bei kleinen bis mittleren Schiebewinkeln. Zum Ausgleich des asymmetrischen Schubs wird ein großer Ruderausschlag benötigt, um die notwendige hohe Seitenkraft zu erzeugen. Das Ziel ist hier die Erhöhung der Seitenkraft durch Verzögerung der Strömungsablösung, um die Seitenleitwerksfläche auf die Anforderungen für den Reiseflug reduzieren zu können und damit Widerstand sowie Gewicht einzusparen. Der erwähnte Entwurfsfall führt zu einem nichtlinearen aerodynamischen Verhalten aufgrund teilweiser Strömungsablösung. Dieses unterscheidet sich von dem einer typischen Verkehrsflugzeug-Flügelgeometrie aufgrund der kleinen Streckung und hohen Pfeilung des SLWs.

Daher ist das Verständnis der zugrundeliegenden komplexen dreidimensionalen Strömung um das SLW die Basis dieser Arbeit. Darauf aufbauend wird der tangenale Schlitz in drei Schritten entwickelt. Zuerst werden an einem 2D-Profil die Effekte von geometrischen Änderungen im Schlitzbereich untersucht. Im nächsten Schritt wird dies zu einer 2,5D-Geometrie erweitert, die eine konstante Profiltiefe und eine Ausdehnung in Spannweitenrichtung hat. Damit können zusätzlich zu einem durchgehenden Schlitz diskrete Schlitze und der große Pfeilwinkel des SLW berücksichtigt werden. Diese führen zur Erzeugung eines Wirbelsystems über dem Ruder, welches hilft die Strömung nicht nur im Pfad des Strahls sondern auch dazwischen in Spannweitenrichtung anliegend zu halten. Zur Optimierung des Wirbelsystems werden die Schlitzbreite und der Abstand zwischen den Schlitzen variiert. In einem letzten Schritt werden die gewonnenen Erkenntnisse auf das 3D-Seitenleitwerk übertragen. Durch die Verringerung der spannwitigen Schlitzausdehnung konnte eine erhebliche Einsparung im Massenstrom von etwa 50% für die gleiche Erhöhung des Seitenkraftbeiwerts erreicht werden. Es konnte also gezeigt werden, dass der Seitenkraftbeiwert durch tangentiales Ausblasen signifikant erhöht werden kann, wobei dies mit diskreten Schlitzen effizienter möglich ist.

Acknowledgements

The majority of this dissertation and all numerical investigations were created during my time in Braunschweig at the DLR Institute of Aerodynamics and Flow Technology. After I left, it became harder to find the time parallel to my new job but perseverance and support from friends and family helped me to finish it. I learned a lot in these years and many people supported me in realizing it.

I would like to sincerely thank my doctoral supervisor Prof. Dr.-Ing. Ralf Rudnik who guided me from the initial start of finding an appropriate topic until the end, contributing his time and experience to shape this work into its final form. As my manager and as head of the Transport Aircraft department at the DLR he gave me the opportunity to also work on topics related to my thesis and allowed me to use the resources available at DLR for further research in my free time, enabling me to turn this project into reality.

I am also very grateful to Prof. Dr.-Ing. Rolf Radespiel who encouraged me to gather the work he saw at several conferences like the STAB symposium and to derive a dissertation from it, giving valuable advice on the way as well. As head of the Institute of Fluid Mechanics of the Technische Universität Braunschweig (TU-BS) he also agreed that I use the experimental findings generated at his institute for the validation of this work. Vickram Singh was responsible for creating these experimental results on the 3D vertical tail. He did not only share the results of the LuFo research project AsSaM with me and was open for discussions about the results but also invested time to make them not only suitable for his dissertation but also to be of use for mine.

Dr.-Ing. Peter Scholz from the TU-BS as head of the working group “Measurement and Manipulation of Flows” encouraged Vickram and me to work on a common goal. He was also the person leading the AsSaM research project, as part of which the tangential blowing design from this numerically-based work could be tested experimentally, contributing one cornerstone for the final success of this work. Based on my suggestions he and Prof. Radespiel agreed to realize two tangential blowing configurations for the wind tunnel tests to have not only the conventional continuous slot configuration but also a direct comparison with discrete slots. To Vickram I am very thankful as well that he agreed to do the additional work required for the second configuration, obtaining interesting results for the whole active flow control community.

Some colleagues at DLR who supported this work are Dr.-Ing. Jochen Wild and Dr.-Ing. Vlad Ciobaca who were essential in initiating the project AsSaM where not only the required experimental validation results for this dissertation could be realized but also part of the numerical 3D vertical tail investigations. In addition to their support in this later stage of my work they were also very supportive and encouraging at the very beginning when I was trying to find a topic. Throughout the genesis of this thesis they were available for various discussions and advice on active flow control and other

topics when needed.

An important contribution to the success of this work was made by Jochen Kirz who did the majority of the 2.5D investigations in his master thesis which I supervised and later became a colleague in the same department at DLR. He did not only make a lot of numerical investigations to study the idea of discrete tangential blowing slots but also contributed with his good work, own ideas about the realization, his open mindset for my ideas and time for a great many discussions. After I left the DLR he brought the project AsSaM to a successful conclusion and on top also supported me personally in finishing my dissertation.

In addition, several other colleagues at the DLR Institute of Aerodynamics and Flow Technology were helping in different ways and I could not name them all. But some of them I want to mention here nevertheless. Sven Geisbauer was always open for discussions about dissertations in general, about what he had learned and the various steps a thesis includes but also for every other topic which seemed to be important — be it scientific or personal. Dr.-Ing. Axel Raichle was a big help by providing his L^AT_EX layout as a starting point and furthermore helped with many related questions.

After I had left DLR, several colleagues at my next job at Airbus were very helpful in realizing this work as well. My team manager Dr.-Ing. Michael Meyer was supportive as much as possible to foster the completion of my thesis. Other colleagues helping to finalize this work were Dr.-Ing. Bruno Stefes and Dr.-Ing. Gerd Heller who both supported me with their advice and time.

Many more people helped or guided me in one or another way to make this dissertation come true and I am very thankful to them all.

Last but not least I am very grateful to my husband Lutz who supported me in every way possible on this journey from the very start until the end.

Weyhe
April 2022

Anna Gebhardt

Contents

List of Figures	xiii
List of Tables	xix
Nomenclature	xxi
1 Introduction and State of the Art	1
1.1 Introduction	1
1.2 Objective and Outline	3
1.3 State of the Art	5
1.3.1 Parameters for the Active Flow Control Investigation	5
1.3.2 Additional Parameters for Unsteady Flow Simulations	6
1.3.3 General Findings Regarding Flow Control	7
1.3.4 VTP Related Findings Regarding Flow Control	11
2 Simulation Setup	17
2.1 Flow Solver and Parameters	17
2.1.1 Turbulence Modeling	18
2.2 Geometry	18
2.3 Mesh Generation	20
3 Verification and Validation of the Numerical Setup	23
3.1 Influence of the Spatial Discretization	23
3.2 Influence of the Time Discretization	26
3.3 Influence of the Turbulence Model	28
3.4 Experimental Setup	29
3.5 Comparison of Numerical and Experimental Results	30
3.5.1 Baseline Configuration Without Blowing	31
3.5.2 Blowing Slot Configurations	35
3.6 Summary	37
4 Studies of Mechanisms and Effects of Tangential Blowing on a Vertical Tail	41

4.1	Investigations Based on a Vertical Tail Section	41
4.1.1	Variation of the Blowing Momentum Coefficient	42
4.1.2	Variation of the Sideslip Angle	43
4.1.3	Variation of the Slot Height	44
4.1.4	Effect of the Step Behind the Slot	45
4.1.5	Effect of the Rudder Thickness Behind the Slot	46
4.1.6	Effect of Slot Angle Variation	48
4.1.7	Effect of Pulsed Blowing	52
4.1.8	Summary	61
4.2	Investigations on an Infinite Swept Vertical Tail Segment	61
4.2.1	Continuous Slot	62
4.2.2	Discrete Slots	63
4.2.3	Effect of the Sweep Angle	70
4.2.4	Effect of Pulsed Blowing	73
4.2.5	Summary	75
4.3	Investigations on a Full 3D Vertical Tail	78
4.3.1	Baseline Flow	78
4.3.2	Continuous Slot	81
4.3.3	Discrete Slots	83
4.3.4	Summary	88
5	Conclusion	91
	Bibliography	99

List of Figures

1.1	Top view of an aircraft with definition of the coordinate system	2
1.2	Different airfoil geometries with tangential blowing slots	8
1.3	Areas of boundary layer and circulation control	9
1.4	Two types of actuators avoiding moving parts	10
2.1	3D VTP side view	20
2.2	2D airfoil	20
2.3	2.5D VTP section	20
2.4	Top view of the 2.5D VTP section	20
2.5	2D airfoil with a detailed view of the blowing slot geometry	20
2.6	2D mesh showing the hexahedron blocks used for field refinement.	21
2.7	Details of the 2D mesh	22
3.1	Dependence of the grid resolution on the global coefficients for three different blowing ratios.	24
3.2	Influence of the grid resolution on global side force and drag coefficients as a function of the momentum coefficient.	25
3.3	Dependence of the temporal and iterative convergence on the global coefficients of a time-resolved simulation.	27
3.4	Comparison of the pressure coefficient distribution for three different turbulence models	28
3.5	Pressure measurement sections of the wind tunnel model.	29
3.6	Side force coefficient versus sideslip angle, 3D VTP, baseline configuration, various calculation proceeds, wind tunnel test results by TU-BS	31
3.7	Sections of pressure coefficient distribution, 3D VTP, baseline configuration compared to wind tunnel results provided by TU-BS, $\beta = 0^\circ$ and $\beta = 7^\circ$	33
3.8	Sections of pressure coefficient distribution, 3D VTP, baseline configuration compared to wind tunnel results provided by TU-BS, $\beta = 0^\circ$ and $\beta = 10^\circ$	33
3.9	Sections of pressure coefficient distribution for SARC and RSM turbulence model results, 3D VTP, baseline configuration compared to wind tunnel results provided by TU-BS, $\beta = 0^\circ$ and $\beta = 7^\circ$	34

3.10	Sections of pressure coefficient distribution for SARC and RSM turbulence model results, 3D VTP, baseline configuration compared to wind tunnel results provided by TU-BS, $\beta = 0^\circ$ and $\beta = 10^\circ$	34
3.11	Side view of the vertical tail with comparison between wind tunnel test and CFD, baseline configuration, $\beta = 0^\circ$	36
3.12	Side force coefficient versus sideslip angle, 3D VTP, comparison between wind tunnel test results and CFD.	37
3.13	Sections of pressure coefficient distribution, 3D VTP, comparison with wind tunnel results provided by TU-BS, $\beta = 0^\circ$, for two different mass flow coefficients $C_{\dot{m}}$, continuous slot	38
3.14	Sections of pressure coefficient distribution, 3D VTP, comparison with wind tunnel results provided by TU-BS, $\beta = 0^\circ$, for one mass flow coefficient $C_{\dot{m}}$, discrete slots	38
3.15	Side view of the vertical tail with comparison between wind tunnel test and CFD, continuous slot configuration, $\beta = 0^\circ$, $C_{\dot{m}} = 3.15 \cdot 10^{-3}$	39
3.16	Side view of the vertical tail with comparison between wind tunnel test and CFD, discrete slots configuration, $\beta = 0^\circ$, $C_{\dot{m}} = 0.81 \cdot 10^{-3}$	39
4.1	Flow field showing the field pressure coefficient distribution including streamlines.	42
4.2	Side force and drag coefficient increment over a variation of the momentum coefficient.	43
4.3	Change in side force coefficient vs. sideslip angle with and without blowing.	44
4.4	Side force and drag coefficient increment vs. momentum coefficient for three different slot heights	45
4.5	Side force coefficient increment vs. mass flow coefficient for three different slot heights	45
4.6	Geometry in the vicinity of the slot with and without step	46
4.7	Variation of the Mach number in the vicinity of the slot for the geometry with and without step at $c_\mu = 0.01$	46
4.8	Geometry in the vicinity of the slot with thinner and original rudder	47
4.9	Variation of the Mach number in the vicinity of the slot for the geometry with thinner and original rudder at $c_\mu = 0.01$	47
4.10	Definition of the slot angle	48
4.11	Geometry in the vicinity of the slot with different slot angles and geometries	48
4.12	Variation of the Mach number in the vicinity of the slot for different slot angles and geometries.	49
4.13	Geometry in the vicinity of the slot showing the location of the velocity profiles	50
4.14	Comparison of velocity profiles at $c_\mu = 0.01$ in x -direction for a variation of the slot angle.	50

4.15	Comparison of side force and drag coefficient increments versus momentum coefficient for different slot geometries and slot angles.	51
4.16	Comparison of the pressure coefficient distribution at $c_\mu = 0.01$ for the geometry with slot angle 0° and thinner rudder, slot angle 15.6° and slot angle 0° without step.	53
4.17	Flow field showing the field pressure coefficient distribution and streamlines for various snapshots over one actuation period, pulsed blowing, $F^+ = 0.3$, $c_\mu = 0.004$	54
4.18	Side force and drag coefficient increment shown versus a variation of the momentum coefficient comparing results for constant blowing obtained with steady and unsteady simulations.	55
4.19	Comparison of unsteady results for constant blowing with pulsed blowing for two dimensionless frequencies	56
4.20	Flow field showing the field pressure coefficient distribution and streamlines where constant and pulsed blowing results are compared for $c_\mu = 0.004$	58
4.21	Flow field showing the velocity magnitude distribution and streamlines in the vicinity of the rudder for different pulsed and constant blowing results at instantaneous snapshots.	59
4.22	Pressure coefficient distribution of instantaneous snapshots at the end of an actuation period for a variation of the dimensionless frequency and c_μ	60
4.23	Side force and drag coefficient increment versus a variation of the dimensionless frequency for two momentum coefficients.	61
4.24	Mean pressure coefficient distribution for $c_\mu = 0.01$ and a variation of the dimensionless frequency.	61
4.25	Surface pressure coefficient and skin friction lines for the continuous slot, $C_\mu = 0.08$	63
4.26	Side force and drag coefficient increment versus momentum coefficient for the continuous slot.	63
4.27	2.5D VTP section with a detail view of three different slot configurations	64
4.28	Streamlines and field slices showing the vortices over the rudder	65
4.29	Side force coefficient increment versus the momentum coefficient at $U_j = 207$ m/s	66
4.30	$N = 1$, $w = 38.2$ mm, $U_j = 207$ m/s, $C_\mu = 0.38\%$	67
4.31	$N = 4$, $w = 9.6$ mm, $U_j = 207$ m/s, $C_\mu = 0.38\%$	67
4.32	$N = 8$, $w = 4.8$ mm, $U_j = 207$ m/s, $C_\mu = 0.38\%$	67
4.33	Side force coefficient increment versus the momentum coefficient at a constant slot width $w = 9.6$ mm and varying gap size g	69
4.34	Side force coefficient increment versus the mass flow coefficient at a constant slot width $w = 9.6$ mm and varying gap size g	69
4.35	$N = 4$, $w = 9.6$ mm, $U_j = 239$ m/s, $C_\mu = 0.5\%$	69

4.36	$N = 8, w = 9.6 \text{ mm}, U_j = 207 \text{ m/s}, C_\mu = 0.75\%$	70
4.37	Top view of the VTP section (stretched span) for two different sweep angles	71
4.38	Side force coefficient increment versus jet velocity for a sweep angle variation	71
4.39	Top view onto the VTP section: skin friction lines and areas marked with $C_{fx} < 0$ for different leading edge sweep angles, $U_j = 207 \text{ m/s}$. .	72
4.40	Aft view of the VTP section: field streamlines (p_t) and vortices (ω_x) for different leading edge sweep angles, $U_j = 207 \text{ m/s}$	72
4.41	Comparison of side force coefficients for constant (const.) and pulsed (PJ) blowing results for the 2.5D geometry for a variation in the numbers of slots	74
4.42	Top view of the VTP section: skin friction lines and areas marked with $C_{fx} < 0$, comparison of constant and pulsed blowing, $N=4, C_\mu = 0.19\%$	76
4.43	Top view of the VTP section: skin friction lines and areas marked with $C_{fx} < 0$, comparison of constant and pulsed blowing, $N=4, C_\mu = 0.38\%$	76
4.44	Aft view of the VTP section: field streamlines (p_t) and vortices (ω_x), comparison of constant and pulsed blowing, $N=4, C_\mu = 0.19\%$	77
4.45	Aft view of the VTP section: field streamlines (p_t) and vortices (ω_x), comparison of constant and pulsed blowing, $N=4, C_\mu = 0.38\%$	77
4.46	Geometry in the vicinity of the blowing slot shown in a slice perpendicular to the rudder hinge line through the 3D VTP with the rudder deflected 30°	78
4.47	Areas with negative skin friction coefficient (blue) and skin friction lines, baseline configuration, suction side	79
4.48	Surface pressure coefficient and skin friction lines, baseline configuration, suction side	80
4.49	Field slices along the VTP span colored with Mach number, baseline configuration, $\beta = 0^\circ$	80
4.50	Field streamlines, baseline configuration, $\beta = 0^\circ$	80
4.51	Side force coefficient vs. normalized span coordinate η , baseline configuration, $\beta = 0^\circ$	81
4.52	Side force coefficient vs. sideslip angle, 3D VTP, baseline and full span slot with jet velocity variation	81
4.53	Areas with negative skin friction coefficient (blue) and skin friction lines, full span slot configuration, $U_j = 200 \text{ m/s}$, suction side	82
4.54	Surface pressure coefficient and skin friction lines, full span slot configuration, $U_j = 200 \text{ m/s}$, suction side	82
4.55	Field slices showing the vortices over the rudder, discrete slots at the 3D VTP, $U_j = 200 \text{ m/s}$	84
4.56	Areas with negative skin friction coefficient (blue) and skin friction lines, discrete slot configuration, $U_j = 200 \text{ m/s}$, suction side	84

4.57	Surface pressure coefficient and skin friction lines, discrete slot configuration, $U_j = 200$ m/s, suction side	84
4.58	Side force coefficient versus sideslip angle, 3D VTP, baseline, full span slot and discrete slots with jet velocity variation	85
4.59	Pressure coefficient distribution in six sections along the span, 3D VTP, baseline, full span slot and discrete slots with $w = 10$ mm, $\beta = 0^\circ$	86
4.60	Side force coefficient versus momentum coefficient for the full span slot and the discrete slots configurations for the 3D VTP	87
4.61	Side force coefficient versus mass flow coefficient for the full span slot and the discrete slots configurations for the 3D VTP	88

List of Tables

3.1	Error estimates for the side force coefficient in [%] compared to an extrapolated solution with the grid spacing tending towards zero	24
4.1	List of slot variations for the 2.5D geometry	64

Nomenclature

Arabic Symbols

Symbol	Designation	Dimension
A_{ref}	Reference area	m^2
A_j	Area of the slot orifice	m^2
b	Span	m
c	Airfoil chord length	m
c_D	Local drag coefficient (2D)	–
C_D	Drag coefficient (3D)	–
C_f	Skin friction coefficient	–
C_{fx}	Skin friction coefficient in x -direction	–
c_L	Local lift coefficient (2D)	–
C_L	Lift coefficient (3D)	–
C_p	Pressure coefficient	–
c_S	Local side force coefficient (2D)	–
C_S	Side force coefficient (3D)	–
C_m	Mass flow coefficient (Eq. (1.4))	–
c_μ / C_μ	Momentum coefficient (2D / 3D) (Eq. (1.1))	–
DC	Actuation duty cycle (Eq. (1.5))	–
f	Frequency (Eq. (1.6))	Hz
F^+	Dimensionless frequency (Eq. (1.6))	–
g	Gap size between slots	m
h_{slot}	Slot height	m
h_{slot}/c	Dimensionless slot height referenced to the chord length	–
l_{slot}	Slot length	m
M	Mach number	–
L	Rolling moment, x -component of resulting moment	N m
M	Pitching moment, y -component of resulting moment	N m
\dot{m}	Mass flow rate	kg/s
N	Yawing moment, z -component of resulting moment	N m
N	Number of slots	–
Re	Reynolds number	–
t	Time	s

Symbol	Designation	Dimension
T	Actuation period	s
U	Magnitude of the velocity vector	m/s
\overline{U}	Time-averaged velocity over one actuation cycle	m/s
w	Slot width	m
x, y, z	Coordinates in the fixed aircraft system	m
x/c	Dimensionless chord length	–
y^+	Dimensionless wall distance	–

Greek Symbols

Symbol	Designation	Dimension
α	Angle of attack	°
β	Angle of sideslip	°
δ_r	Rudder deflection angle	°
Δ	Increment	–
η	Normalized span coordinate	–
μ	Dynamic viscosity	kg/(m s)
ρ	Density	kg/m ³
ω_x	x -component of the vorticity	rad/s
ϕ	Sweep angle	°

Subscripts

Symbol	Designation
j	Jet conditions
LE	Leading edge
peak	Peak (velocity) during one actuation cycle
TE	Trailing edge
∞	Freestream conditions

Acronyms and Abbreviations

Symbol	Designation
2D	Two Dimensional
3D	Three Dimensional
ALM	Added Layer Manufacturing
ACARE	Advisory Council for Aeronautics Research in Europe
AFC	Active Flow Control

Symbol	Designation
C ² A ² S ² E	Center for Computer Applications in AeroSpaceScience and Engineering
CFD	Computational Fluid Dynamics
DDES	Delayed Detached-Eddy Simulation
DLR	Deutsches Zentrum für Luft- und Raumfahrt (German Aerospace Center)
GGDH	Generalized Gradient Diffusion Hypothesis
LBM	Lattice Boltzmann Method
LRR	Launder-Reece-Rodi
LUSGS	Lower-Upper Symmetric Gaus-Seidel
MFR	Mass Flow Rate
MUB	Model Unterschallwindkanal Braunschweig (model subsonic wind tunnel Braunschweig)
NASA	National Aeronautics and Space Administration
OEI	One engine inoperative
ONR	Office of Naval Research
RANS	Reynolds-Averaged Navier- Stokes [equations]
RSM	Reynolds stress model
SAO	Spalart and Allmaras turbulence model, original version
SARC	Spalart and Allmaras turbulence model with vortical and rotational flow correction
SGG	Speziale-Sarkar-Gatski
TU-BS	Technische Universität Braunschweig (University of Technology Braunschweig)
URANS	Unsteady Reynolds-Averaged Navier-Stokes [equations]
ZNMF	Zero Net Mass Flux
VGJ	Vortex Generating Jet
VTP	Vertical Tail (Plane)
WTT	Wind Tunnel Test

1 Introduction and State of the Art

This chapter presents the introduction, the objective and outline of this work and an overview of related research and literature.

1.1 Introduction

Since 1970, air traffic has been doubling every 10 to 15 years, largely unaffected by worldwide crises like the oil crisis in the mid-1970s, the 9/11 terrorist attacks closely followed by the first SARS outbreak 2000-2003 and the world financial system crisis 2008 [1]. Thus, air traffic was forecast to continue growing in the coming years [2, 3]. In line with this, the number of flying aircraft is predicted to increase as well, leading to a rise in air pollution. This being recognized, large efforts are made to lower the global emissions created by aircraft like carbon dioxide and nitrogen oxide despite the fact that the total number of air vehicles is growing. Ambitious targets are set by the Advisory Council for Aeronautics Research in Europe (ACARE) to reduce atmospheric pollution [4, 5]. Strategies followed are on one hand a change of the fuel to a one which is made from sustainable biomass and thus more environmentally friendly, or the use of electrical engines. On the other hand for example efforts are made to improve the technology of the aircraft itself targeting its fuel consumption. Here, drag and weight reduction are sought after. This would result in less fuel burned for the same transport task, leading to a reduction of the emissions.

With regard to the drag and weight reduction, different technologies are investigated. For weight reduction composite materials are for example used today or added layer manufacturing (ALM). The latter allows to build optimized structures which are not primarily driven by the manufacturing methods available but by the load paths of the structure. For drag reduction, a main driver is the aerodynamic shape of the aircraft. Here one attempt strives for example to reduce the skin friction drag by increasing the extent of laminar flow of the airfoil or the wing [6]. Another way would be an optimized shape design and a decrease of the wetted surface to reduce friction drag and also pressure drag. Smaller components not only tend to be lighter themselves, but their reduced weight can also lead to a decrease of the weight of the underlying and supporting structure resulting from snow ball effects.

In general, transport aircraft are optimized for cruise flight which is the segment they spent most of the time in during one flight. Nevertheless, one component which is today often sized by low speed conditions seen at take-off and landing is the vertical tail(plane) (VTP). The main function of the VTP is to provide stability and control for the aircraft about the yaw axis which is the z-axis in Fig. 1.1. For most conventional transport aircraft used today, modern fly-by-wire systems help to artificially augment the cruise

yaw stability, allowing a smaller VTP size during this part of the flight. During take-off and landing, the speed of the aircraft is lower than in cruise flight. This means that also the aerodynamic forces produced in these flight phases are smaller. The rudder of the VTP, which is the aft part, can be deflected while the forward part, the fin, is fixed. The rudder works as a plain flap, allowing to change the magnitude of the side force created by the vertical tail for controlling the aircraft about the yaw axis. Similar to the effect of a plain flap or an aileron on the lift of a wing, an increase of the rudder deflection angle δ_r leads to an increase of the side force. Beyond a certain rudder deflection angle any further increase does not lead to an increase in the side force any more since the airflow cannot further follow the contour and separates. Therefore, the size of the VTP needs to be increased if more side force is required. One case where this is needed is the one-engine-inoperative (OEI) condition. Here, the critical engine on one side of the aircraft fails, with take-off being a critical flight segment for this to happen. In this segment the aircraft velocity is low while the thrust of the engines is high. Thus, in case of a one-sided engine failure the aircraft experiences a large yawing moment N created about the center of gravity due to the still running engine. If the right or in Fig. 1.1 the upper engine fails, the left or lower engine has a large thrust component pointing forward, leading to a clockwise moment which is in this case opposite to the rotation direction of N shown in the figure. This moment then needs to be counteracted by the VTP and is usually a sizing criterion.

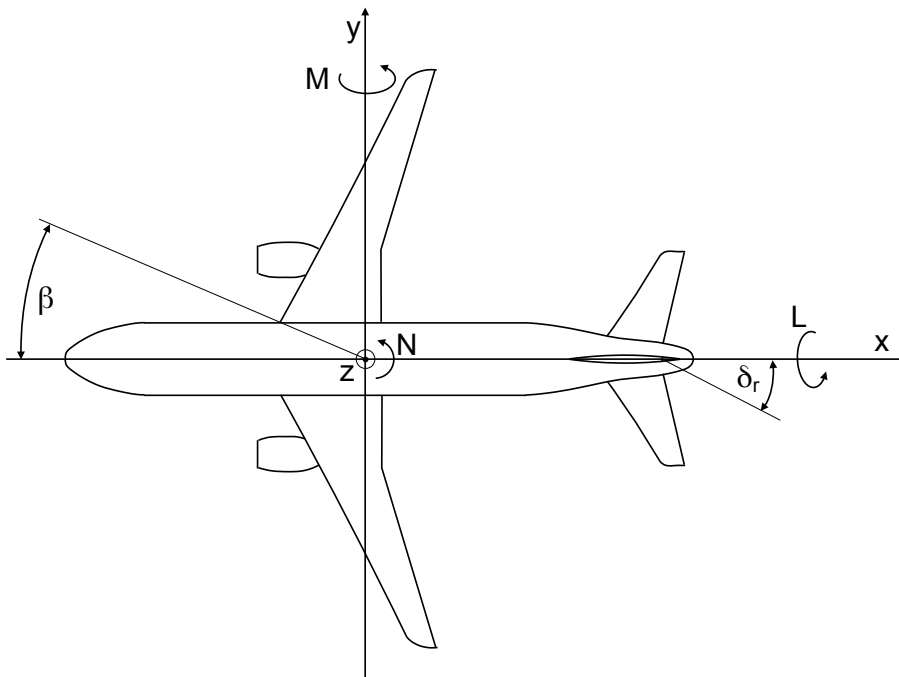


Fig. 1.1 Top view of an aircraft with definition of the coordinate system

In the OEI case the rudder is highly deflected to achieve the maximum side force possible. This is often combined with small to medium sideslip angles β . Such flow conditions at the VTP lead to non-linear aerodynamic characteristics, caused by partial flow separation on this usually low aspect ratio, highly swept lifting surface. If the VTP size should be kept small and just sufficient to satisfy cruise flight requirements, other means have to be found to generate the large side force needed during the OEI maneuver. Because the same behavior in response to asymmetric flow from left and

right is desired about the vertical axis of the aircraft, the VTP has a symmetric airfoil. Hence, whatever is integrated must be usable in a symmetric way for left and right rudder deflection. In addition, the means needs to be effective in a very short time frame as necessary for an OEI case. One possibility for side force augmentation is the use of flow control. This can be done in a passive or an active way. Passive would for example be the implementation of vortex generators which are usually small metal plates which are added approximately perpendicular to the surface and could have a rectangular or triangular shape. These vortex generators create vortices which help — when placed properly — to enhance the mixing with the surrounding flow, thus increasing the momentum in the boundary layer and delaying or preventing flow separation. They have the advantage that they are relatively simple to integrate and easy to maintain. However, they are fixed on the aircraft and can usually not be retracted in cruise flight when they are not needed, leading to a measurable increase in drag.

With active flow control (AFC), energy is locally introduced into the flow by an actuator with the intention to influence the flow field on the whole VTP. The advantage of active flow control means is that they can be turned off when they are not in operation, for example during cruise flight, and thus do not lead to an aerodynamic drag penalty when they are not needed. In addition, it might be possible to adapt them to changing conditions during the flight. On the other hand their implementation is more complicated. Furthermore, the weight of the additional systems can be interpreted as a drag increment which needs to be compensated by the reduction in VTP size (leading to both reduced drag and weight) before the AFC system can provide a net benefit. Additionally, a source for the provision of energy has to be found and provided with very high reliability. This energy input can be used to power different types of actuators like fluidic, thermal or plasma actuators.

Further research on the actuators themselves is still necessary to improve their functionality or to make them applicable to real flight conditions which is something that has not changed fundamentally over the last years [7]. Thermal or combustion [8] actuators suffer up to now from a limitation to relatively low frequencies whereas plasma actuators can only generate limited output velocities and need very high voltage to work. Fluidic actuators usually use the surrounding air which is blown through exit holes or slots in the aircraft surface with a certain alignment, direction, shape and size. One kind of these actuators, synthetic jets, have for example a vibrating membrane for ingesting air and then releasing it again. They are also called zero-net mass-flux actuators. This kind of actuator needs in principle apart from the actuator itself just an electric power supply. Other actuator types need pressurized air, which requires an energy source for generation, and the corresponding ducts to guide the air, ejecting a jet into the flow field. This type is the only kind of actuator of sufficient maturity which would allow installation on transport aircraft today. Such actuators can be used to delay or avoid flow separation and increase the force that can be produced by force-generating components like a VTP.

1.2 Objective and Outline

The objective of this work is to understand the complex three-dimensional flow at a vertical tailplane with large rudder deflection and small to medium sideslip angles and

then to find active flow control means to delay the flow separation. This can among others allow the design of a smaller VTP, reducing weight and drag and would thus contribute to reducing an aircraft's fuel consumption. From the variety of flow control methods available, blowing by fluidic actuators is selected, which is already used in a wide range of active flow control applications. Specifically tangential blowing will be considered. The ambition of the investigations done for this work is not only to find some effective way of tangential blowing — this was already shown for similar 2D geometries and other 3D but more wing-type geometries in literature — but also to improve its efficiency.

Starting from the available literature and the current state of the art in the remainder of this chapter, the application of tangential blowing will be extended for use on the vertical tailplane. For typical turbofan-powered passenger transport aircraft, the VTP differs from the wing by its larger sweep angle and the very low aspect ratio. This changes its basic flow characteristics and leads in summary to a much more three-dimensional flow when approaching its maximum side force capacity. In contrast to other kinds of fluidic actuators like sweeping jets and synthetic jets, not much data or results concerning the VTP exist for tangential blowing. This makes this type of blowing interesting for further research to examine its potential especially with the focus on increased efficiency.

In this thesis, first a design for the tangential blowing will be developed using numerical methods. In contrast to other existing VTP studies, a different flow solver will be used, namely the TAU code, solving the Reynolds-averaged Navier-Stokes equations. The simulation setup will be described in **Ch. 2** including important aspects about the geometry, the mesh generator and the flow solver.

Since the application of the TAU code to this specific kind of problem was not examined before, some work is invested in the verification and validation of the numerical setup in **Ch. 3**. To make the validation of the numerical results possible, experimental results obtained on the same geometry were provided by the Technische Universität Braunschweig (TU-BS). To allow a direct comparison between experimental and numerical results, the numerical investigation is performed at the same scale and Reynolds number as used in the wind tunnel test.

A multi-disciplinary study for finding a suitable location for the blowing slots on the VTP was carried out before in collaboration with an industrial partner. Identified requirements are the possibility to integrate the system in the existing structural concept without too many modifications and to avoid rotating parts like the rudder, which would complicate the integration significantly. With these constraints in mind, a location aft of the fin box but in front of the rudder was determined to be a suitable location. Therefore this study concentrates on tangential blowing over the rudder with the jet exit located at the end of the fin.

The design and analysis of the active flow control system will be done in **Ch. 4** using a combination of 2D, 2.5D and 3D simulations. Starting with a 2D airfoil geometry, some investigations are performed for which 3D effects are negligible or only play a minor role. This includes for example a variation of the slot height, modeling of small geometric changes or the effect of tangential pulsed blowing on the mass flow rate but also a variation of the blowing momentum coefficient and the sideslip angle. Since in 2D spanwise effects cannot be investigated, a 2.5D approach is the next step. Here the high sweep angle of the VTP is captured. With the span being infinite the tapering of the VTP cannot be considered. The 2.5D approach makes it possible to investigate the

effect of replacing the full-span slot by several discrete slots along the span. This aims to reduce the momentum coefficient needed due to the reduced slot area and by this increasing the efficiency. The effect on the increase in the side force coefficient will be examined and compared to the full-span slot. In a next step the results are transferred to the 3D VTP. First, the baseline flow without blowing is analyzed to enable a deeper understanding of the flow and the application of the blowing. Then, the best slot design from the 2D and 2.5D study is transferred to the 3D geometry. Here again, results for a continuous slot are compared to discrete slots. The mass flow rate and momentum coefficient are investigated and the potential of these important parameters for the 3D geometry, which is the relevant geometry for an actual application on a transport aircraft, is discussed.

In **Ch. 5** the results and findings of this work are summarized and compared to other studies carried out by the research community.

1.3 State of the Art

In this section, first some parameters of interest for the active flow control investigation and in addition for unsteady pulsed blowing simulations are described in Sec. 1.3.1 and Sec. 1.3.2 before presenting the findings of a literature study. Flow control for aircraft applications has been a research topic for a couple of decades. A lot of investigations were done for 2D and wing-type geometries. Some important or representative findings will be presented in Sec. 1.3.3. The investigations behind often assume a long, higher aspect ratio wing which is often not or only slightly tapered and has no or only moderate sweep. However, as already stated before, a transonic transport aircraft VTP has a planform with a much lower aspect ratio, higher taper and higher sweep angle. This leads to a more three-dimensional flow field, especially when approaching its maximum side force capacity where AFC would be beneficial, as was for example observed in [9]. Under such conditions, flow control concepts optimized for a wing might not be suitable. Therefore the flow control studies done for VTP-like geometries are summarized separately in Sec. 1.3.4.

1.3.1 Parameters for the Active Flow Control Investigation

For industrial applications two main parameters for the design of an AFC system with relation to the aerodynamic efficiency are usually of interest. The first is the momentum coefficient and the second one the mass flow rate or mass flow coefficient.

The momentum coefficient was suggested by Poisson-Quinton [10] as an important non-dimensional parameter for boundary layer control. The exact definition varies a bit in the literature. In the frame of this work it is defined as follows:

$$C_\mu = \frac{U_j \cdot \dot{m}_j}{\frac{1}{2} \cdot \rho_\infty \cdot U_\infty^2 \cdot A_{\text{ref}}} = \frac{U_j^2 \cdot \rho_j \cdot A_j}{\frac{1}{2} \cdot \rho_\infty \cdot U_\infty^2 \cdot A_{\text{ref}}} \quad (1.1)$$

where \dot{m}_j is the mass flow rate of the jet through the actuator slot with the jet velocity U_j and the jet density ρ_j . The variables ρ_∞ and U_∞ are the density and velocity of the onset flow in the farfield, A_{ref} is the reference area of the model used which is the chord

length times one for the 2D cases, the chord length times span for the 2.5D cases and the planform area for the 3D cases. A_j is the area of the slot orifice. For the pulsed blowing simulations the time-averaged velocities need to be considered for which U_j is replaced in the formula by the time-averaged jet velocity over one period. The formula above was extended to consider unsteady actuation [11] and can be written for a square signal as:

$$C_\mu = \frac{1}{DC} \frac{\overline{U}_j^2 \cdot \rho_j \cdot A_j}{\frac{1}{2} \cdot \rho_\infty \cdot U_\infty^2 \cdot A_{\text{ref}}} \quad (1.2)$$

with

$$\overline{U}_j = DC \cdot U_{j, \text{peak}} \quad (1.3)$$

where DC is the duty cycle (compare Eq. (1.5) below) and $U_{j, \text{peak}}$ is the peak jet velocity during the actuation period.

A more accurate definition of the momentum coefficient is given in [12], where the term $(p_j - p_a) \cdot A_j$ is added to the numerator in Eq. (1.1). This additional term takes the difference of the pressure between the blowing slot p_j and the external flow p_a into account. For an under-expanded jet this pressure difference can be neglected and will not be used in the remainder of this work.

The mass flow coefficient is a measure for how much mass flow is used by the blowing device. It is defined as:

$$C_{\dot{m}} = \frac{\rho_j \cdot U_j \cdot A_j}{\rho_\infty \cdot U_\infty \cdot A_{\text{ref}}} = \frac{\dot{m}_j}{\rho_\infty \cdot U_\infty \cdot A_{\text{ref}}} \quad (1.4)$$

The mass flow rate is quite important since the air blown out of the slots has to be provided by some source. The amount needed has an impact on the size of the tubes that need to be used and with this on the integrability into the structure and the weight added. The other one, the momentum coefficient, has usually a similar tendency as the mass flow rate, but here the jet velocity has a higher impact. So if a high jet velocity is needed and with this an increased pressure in the tubes, this parameter might be even more important, having also an impact on the sizing of the required compressors and with this also on additional equipment and weight. These two parameters will be used in the following chapters to judge the different designs. Since the 2D and 2.5D results are only an intermediate design step, more emphasis is put on the momentum coefficient while for a realistic 3D geometry meaningful values for the mass flow coefficient can be obtained as well which will be analyzed more in depth in the corresponding sections.

1.3.2 Additional Parameters for Unsteady Flow Simulations

For unsteady flows the parameter space is broadened by time dependent variations. One important parameter is the duty cycle DC:

$$DC = \frac{t_{\text{blowing}}}{t_{(\text{blowing} + \text{off})}} \quad (1.5)$$

It describes the time the jet is blowing divided by the overall time of the period, i.e. the sum of the time with and without blowing until the next blowing cycle starts. The duty cycle can be varied between zero and one. One would be the value for a constant

blowing jet. The duty cycle can also vary between adjacent slots as can the starting time of the blowing which could for instance lead to alternate blowing of neighboring jets. Often a duty cycle of 0.5 is used where the jet is blowing half the time [13]. This was also found to be a good compromise between the required mass flow rate and the lift coefficient achieved [14]. $DC = 0.5$ is also the effective value for synthetic jet/ZNMF actuators with combined suction and blowing. Since the optimization of the pulsed blowing parameters is not at the center of interest in the present work but a comparison between constant and pulsed blowing in general, a value of 0.5 is used throughout.

Another important parameter is the actuation frequency which can be obtained by:

$$f = \frac{U_{\infty} \cdot F^{+}}{c_{\text{Rudder}}} \quad (1.6)$$

Here U_{∞} is the reference freestream velocity, F^{+} is the dimensionless frequency and c_{Rudder} the rudder chord length as characteristic length which the flow has to travel from the slot to the end of the vertical tail. With the geometry and thus the denominator fixed in Eq. (1.6) as well as the freestream velocity given by the aircraft velocity, only the frequency or dimensionless frequency can be varied. Here again substantial variations are possible. In the literature screened F^{+} in the region of 1 is suggested for maximum lift augmentation [15, 16] which is also used here as starting point for the investigation.

1.3.3 General Findings Regarding Flow Control

Influencing the lift and drag of an airfoil or wing by active means has been studied for decades. Fluidic actuators were invented quite early and several types have been developed over the years. With the introduction of the boundary layer theory by Prandtl at the beginning of twentieth century [17] he also showed the possibility to delay separation by suction through slots at a cylinder. In the 1920's also blowing through slots was examined. In 1921 Baumann developed the idea to blow highly pressurized air through slots [18]. The idea behind using suction through slots was to remove weakened flow from the boundary layer and thus help the flow to stay longer attached. This is also the objective of the blowing slots which increase the near-surface flow velocity by adding energy to the boundary layer, helping it to overcome the adverse pressure gradient. Experiments for example performed by Reid and Bamber [19] or Knight and Bamber [20] confirmed that blowing slots can enhance the lift of a 2D airfoil. One part of the research focused first on airfoils or wings with elliptically shaped airfoils or rounded trailing edges as shown in Fig. 1.2(a). Air blown tangentially to the surface was used to achieve circulation control. The intention was not only to avoid separation but also to move the aft stagnation point to the lower side as explained by Nielsen and Biggers [21] what is accompanied by an increase in the circulation. Moving the rear stagnation point to the lower side of the airfoil relies on the Coanda effect and required the substitution of the sharp trailing edge with a round one. The Coanda effect works by creating a low pressure region between the high velocity jet and the solid surface due to the entrainment of surrounding fluid. This leads to a flow which stays longer attached to the curved surface. The flow separates only if the energy introduced by the jet is used up by friction effects or if the centrifugal forces due to the curvature of the surface prevail. For this approach the blowing slot was usually positioned close to the round trailing edge.

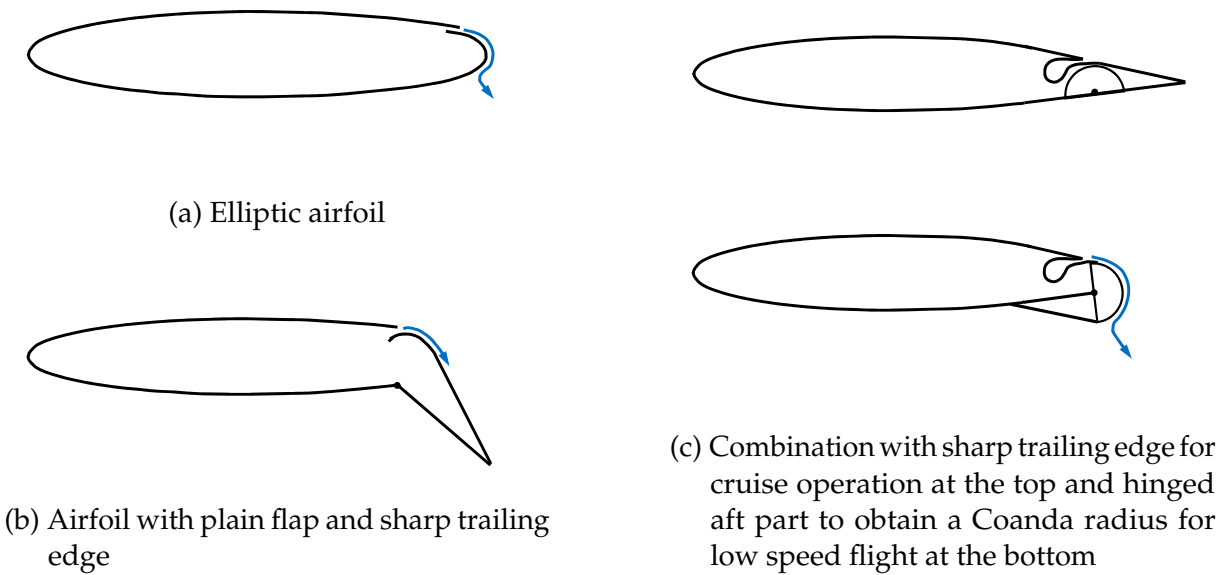


Fig. 1.2 Different airfoil geometries with tangential blowing slots

Since conceptionally sharp trailing edges are used on transport aircraft because they are advantageous regarding drag in cruise flight, tangential blowing was also investigated on this kind of geometries [22, 23]. Here the jet was blown over the upper surface of a plain flap following the round flap shoulder as depicted in Fig. 1.2(b). Further designs were tested where the flap with a sharp trailing edge could expose a cylindrical surface which then became the Coanda trailing edge [24] as shown in a schematic sketch in Fig. 1.2(c). The aim was to obtain a shape which is optimized predominantly for cruise flight but which can still provide benefits when used with tangential blowing.

By increasing the blowing over the deflected flap with a sharp trailing edge a separation can be avoided up to the trailing edge. This part of mass flow investment is called boundary layer control. Increasing the mass flow rate even further than needed for complete flow attachment is called super-circulation or circulation control. This leads to a deflection of the streamlines as if the effective trailing edge is extended. In this range more mass flow needs to be invested for the same increase in lift as it is the case in the boundary layer control regime. This is sketched in Fig. 1.3. Summaries of the research related to circulation control and its application were for example compiled by Korbacher [25] and Englar [26].

It was found that a relatively large mass flow investment is required to obtain a fully attached flow for a highly deflected flap. This amount of mass flow is currently considered too high for commercial applications [11]. One approach which has shown an improvement in that area is the use of oscillatory or pulsed blowing. With this, the jet is only blowing part-time. Due to the higher frequencies used, the mean flow field stays attached while the blowing leads to spanwise vortices running downstream over the wing. For wing-type geometries it was shown that the pulsed jets require significantly less mass flow than steady tangential blowing for separation control (e.g. by Seifert et al. [27], Nishri and Wygnanski [15], or Jones and Englar [28]). Additional optimization parameters for this unsteady problem are now the actuation frequency, the duty cycle and the blowing amplitude. The angle of the jet relative to the surface is

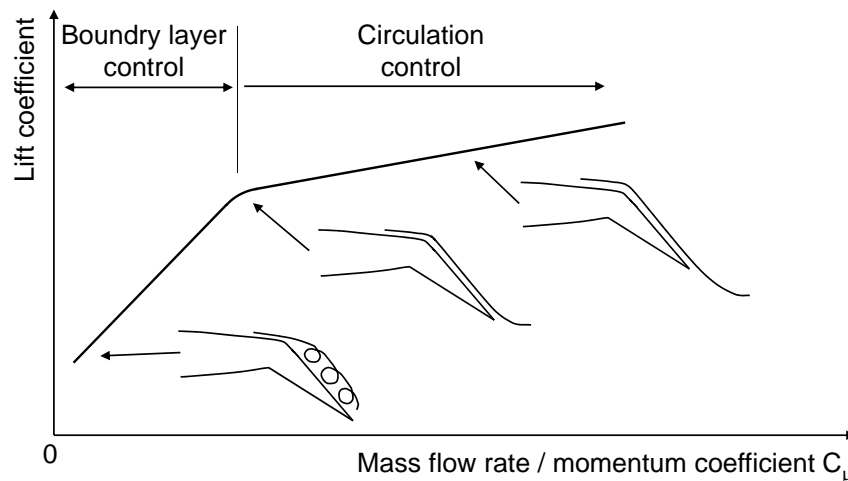


Fig. 1.3 Areas of boundary layer and circulation control

another parameter which can be varied as well as can the distance between adjacent slots for 3D wings. The aim of the increased slot spacing is to reduce the required mass flow even further. This could also include a combination of suction at one location and ejecting the air again at another. Related wind tunnel experiments employed some kind of fast-switching valves like rotating, flapping or solenoid ones. But installing these valves on an airplane would be quite complex, especially while assuring high reliability and robustness as required for critical systems. This led to the development of other actuator types which avoid moving parts. One kind are two-stage fluidic pulsed blowing actuators where the air is split into two loops as shown in Fig. 1.4(a). One loop or stage is the main supply providing the air which is ejected through one of two nozzles of each actuator. The other one is the control stage which enters the actuator from the side pushing the first, main air stream alternately towards one or the other nozzle. This is described by Bauer et al. [29]. Usually the actuator blowing direction has some angle other than tangential or perpendicular to the wing surface. Another kind of actuators are sweeping jets which have just one airstream towards each actuator, but inside the actuator a feedback loop is included which drives the jet alternately in one or the other direction of the outlet (see Fig. 1.4(b)). This leads to a sweep of the airstream on the wing surface. One of the first applications of the sweeping jets to aircraft wing geometries was described by Seele et al. [30] and with a bit more detail about the working principle later by Graff et al. [31]. The sweeping jets are often aligned tangentially to the surface. Thereby, their jet is not only covering a larger part of the wing surface due to the sweeping reducing the mass flow required, but it also takes benefit of the effects of tangential blowing by adding momentum to the flow close to the surface.

Scaling of the actuators and systems used in wind tunnel tests without reducing their effect was a topic for many years since the high efficiency gains observed in small-scale low Reynolds number experiments were found to be not directly transferable to large-scale applications [32]. Current research results show that this has improved in recent years. A flight test on a Boeing 757 with sweeping jets on the vertical tail has shown that the actuators are delivering significant performance improvements also at full-scale [33]. For two-stage fluidic actuators a wind-tunnel investigation could show recently that

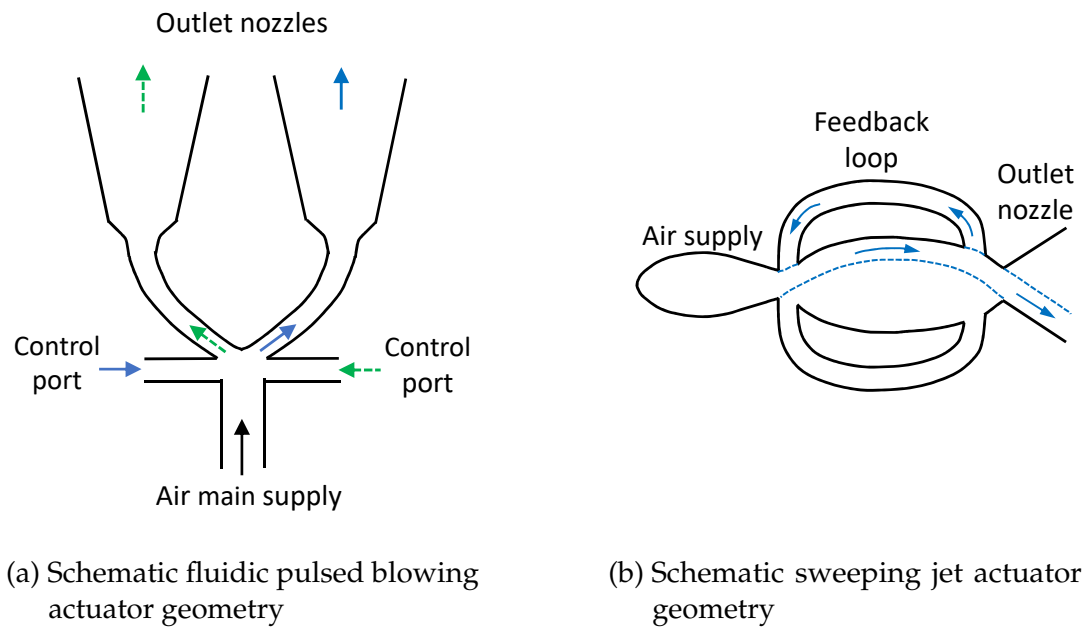


Fig. 1.4 Two types of actuators avoiding moving parts

this kind of actuator can be effective at full-scale for an industrial application, delaying separation on the wing by blowing close to the leading edge in the pylon region [34].

Other kinds of actuators are zero-net mass-flux (ZNMF) actuators, also known as synthetic jets, which combine suction and blowing in one device. Using for example an oscillating diaphragm or a piston they first ingest fluid into a small chamber or cavity and then expel it again. One of the first applying it to lifting surfaces were Honohan et al. in 2000 [35]. This kind of actuator is quite attractive since it needs no mass flow source to work. The main drawback are the limited peak velocities which can be achieved by this device. Current research is targeting to improve the exit velocities well above 100 m/s to make them interesting for industrial applications [36, 37].

A further type of actuators are vortex generating jets (VGJs). Their effect is similar to conventional vane vortex generators by generating rotating vortices inside the boundary layer enhancing the mixing of the flow. While conventional vortex generators for example consist of a small rectangular or triangular metal plate attached perpendicular to the surface creating additional drag during the whole flight time, the active VGJs can be turned off leaving just a small hole in the surface. The blowing direction is skewed and pitched with respect to the freestream direction. To be effective, the skew and pitch angles have to be well adapted to the local flow which needs to be taken care of during the design process. Since the intention is not the addition of momentum but the augmentation of the momentum exchange, the required mass flow rates are relatively low. However, this also limits the potential increase of the lift coefficient which is smaller than for example for the pulsed or tangential blowing devices mentioned above.

Finding an effective but still efficient way to apply these different kind of actuators is still a part of the ongoing research in an effort to make them interesting for commercial airplanes. Examples of applied active flow control are the Lockheed F-104 featuring internally blown flaps, where air was blown over the flaps to enhance the lift in the low speed region and a version of the MiG-21. A more recently developed aircraft using

boundary layer control is the ShinMaywa US-2, an amphibious sea rescue aircraft which had its first flight in 2003. The application of active flow control is up to now more limited to military aircraft. The application to mass-produced civil transport aircraft is still to come, requiring besides efficiency also reliability and less complex systems to make active flow control a net benefit for the airlines.

In the beginning all investigations were based on experiments. With improvements in computational power, more and more numerical investigations are performed using different flow simulation software for problems with growing complexity and even for unsteady pulsed blowing simulations. One part of a large workshop in 2004 was used to assess the CFD capabilities for calculating a two-dimensional test case with Coanda blowing over an elliptical trailing edge. During this NASA/ONR Circulation Control Workshop the need for more and properly designed experimental validation cases was observed [38] since the output is also dependent on properly specified boundary conditions. Another example of a large workshop dealing with the prediction of experimental results by CFD was called "CFD Validation of Synthetic Jets and Turbulent Separation Control", held in 2004 [39]. Experiments were designed specially for this workshop and the results and test cases of this "CFDVAL2004" workshop have been used since then in the community to enhance the CFD methods, with the modeling of the boundary condition being one topic. In general, the agreement depends on the configuration investigated, the flow conditions as well as the turbulence model. Ciobaca [40] carried out a validation exercise showing that the TAU code can be used for active flow control calculations and provided some guidelines on how to model a part of the slot to apply the boundary condition with special focus on unsteady Reynolds-averaged Navier-Stokes (URANS) computations and pulsed blowing. His approach is followed in this work.

1.3.4 VTP Related Findings Regarding Flow Control

After the wing was for many years the main subject of active flow control applications for transport aircraft, the range of applications has broadened in recent years. Currently the vertical tail is the subject of several investigations targeting the increase of the side force by active flow control. In contrast to wing related investigations it has to be kept in mind that now due to the vertical arrangement on the aircraft the side force is the parameter of interest which is corresponding to the lift of a wing. Similarly, the sideslip angle at the vertical tail is equivalent to the angle of attack at the wing.

Experimental Investigations

Low scale wind tunnel tests were conducted 2012 by Seele et al. [41, 42] and Rathay et al. [43, 44, 45, 46]. Seele et al. used sweeping jets on a generic vertical stabilizer model which was mounted on the wind tunnel floor. At a Reynolds number of up to 1.5 million several rudder deflection angles and a variation in the sideslip angle were investigated. The 92 actuators were placed close to the hinge line of the 1.067 m span model, near but upstream of the location of natural separation. Depending on the freestream velocity and momentum input a side force increase of approximately 50% was achieved for reasonable mass flow or momentum coefficients with $C_\mu \leq 1\%$. Rathay et al. on the other hand concentrated on synthetic jets as active flow control

device. They used a generic vertical tail based on public information available for the planform of the Boeing 767. The span of the first wind tunnel model was 0.39 m which is about $1/25^{\text{th}}$ of a full scale geometry, resulting in a Reynolds number of 275000. Eight synthetic jet actuators were integrated into the model just upstream of the hinge line. They reported a 18% increase in the side force coefficient at moderate rudder deflection angles for cases without sideslip. No absolute values were given for this investigation as well, like for the above mentioned ones from Seele et al. During the investigation of spanwise spacing and the effect of different actuation locations it was observed that the mid-span actuators are the most effective ones for moderate rudder deflection angles. In addition, wind tunnel tests were conducted by Rathay et al. with a larger model at a scale of about $1/19^{\text{th}}$ [47]. The model now featured a span of 0.53 m and a Reynolds number of 350000. The number of synthetic jet actuators was increased to twelve. Here also the sideslip angle was varied and an increase of the side force coefficient by 34% was reported. Part of this work was a more detailed analysis of the interaction of the jets with the surrounding flow. Furthermore, the effect of the orientation, location, and geometry of the synthetic jet orifices on the effectiveness of the actuation was studied [46].

Building on these results the integration of the two active flow control systems in the vertical tail of an aircraft was investigated by Mooney et al. [48] in a study carried out by the research agency NASA and the aircraft manufacturer Boeing. The aim was to assess the net benefits at aircraft level while taking systems integration and operational requirements into consideration. This included for example the additional time for manufacturing, maintenance cost, space for the additional components and power requirements. It was assumed that the vertical tail was sized for the longest version of an aircraft family. Shorter aircraft would then include active flow control on the vertical tail so that it can achieve the higher maximum side force required to generate a similar yaw moment with the shorter moment arm than the longer aircraft. Through this design principle, a vertical tail size reduction of 17% was assumed. Sideslip angles from 0° to 8° were specified as being representative for the critical range. Since the OEI case is reported to be the critical maneuver during take-off, climb, approach, and landing, the airspeed associated with the operation of the AFC devices is in the lower range. One outcome of the study is that for both actuator types the benefit due to drag reduction associated with the reduced size outweighs the negative impacts caused by the implementation of the system. Since several assumptions were made for this study where no or only little data was available, rather conservative values were used where the data was less certain. The sweeping jet actuators were found to have a larger benefit than the synthetic jet actuators. For the sweeping jets the auxiliary power unit (APU) was assumed to deliver the required compressed air. Since a tendency can be seen that aircraft systems become more and more electrically powered, the bleed air capability of the APU could reduce for new aircraft. This could become a drawback for AFC actuators requiring compressed air since additional systems might need to be installed just for supplying this compressed air, adding weight to the aircraft. For synthetic jets — depending on the exact requirements — the availability of sufficient electrical power might also lead to additional weight. This has to be kept in mind for future aircraft developments. However, since the sweeping jets could deliver a larger side force augmentation it made them a favorite for further studies. Another advantage of this actuator type is that the maturity required of flight scale actuators has already been achieved while more development work is needed for the synthetic jet actuators.

The small-scale wind tunnel tests mentioned above were followed in 2013 by a large scale wind tunnel test on a full-scale Boeing 757 vertical tail with a span of about 7.60 m. For this, 37 individually controlled and evenly spaced sweeping jet actuators were used. Results of this test were reported by Andino et al. [49] and Whalen et al. [50]. At a freestream velocity of 51.4 m/s a Reynolds number of 15 million was achieved. The range of rudder deflection angles investigated was between 0° and 30° at sideslip angles between -20° and 20° , with the most interesting range deemed to be between 0° and 7.5° . The variation of the parameters involved the actuator spacing, the momentum coefficient and the configuration of the active actuators. One finding was that the tip actuators could be turned off without significant effect on the gain in the side force coefficient. A significant effect was also found depending on whether the rudder leading edge cut-outs for the actuators were present or covered. These cut-outs lead to a pressure exchange between pressure and suction side and degraded the performance of the reference configuration without flow control. A targeted side force coefficient increase of 20% was achieved with less input from the actuators than for the configuration with leading edge cut out covers installed. With cut-outs a momentum coefficient of approximately 0.5% was needed at a sideslip angle of 7.5° . With cut-out covers installed an additional 0.25% momentum coefficient was required. Since no cut-outs were present in both sub-scale tests and CFD calculations, this was an important observation for cross-comparison. A side force coefficient gain of more than 20% could be reached with a 31 actuator configuration at maximum rudder deflection angle and also at a higher sideslip angle of 7.5° . In general, the required momentum coefficient needed to be increased with increasing sideslip angle. Compared to the small-scale experiments conducted by Seele et al. the amount of momentum coefficient to obtain a 20% increase in the side force coefficient was very similar for the case without leading edge cut-outs. The full-scale wind tunnel test was used for preparing a flight test with a Boeing 757, called ecoDemonstrator, with a modified vertical tail. The results were summarized by Whalen et al. [51, 52] and Lin et al. [33, 53]. A more detailed description of the system design and integration was prepared by Alexander et al. [54]. The flight test was conducted in April 2015 with a 31 sweeping jet actuator configuration placed between the root and 70% of the span. The jet exit area was with 6.35 mm times 12.7 mm about the same size as in the full-scale wind tunnel test. The pressurized air was provided by the APU. Based on the flight test data in conjunction with the full-scale wind tunnel test results and the Boeing aerodynamic database for the Boeing 757 an increase of the side force coefficient by about 14% was estimated at 30° rudder deflection angle and at relevant sideslip angles up to 7.5° . Due to flight test limitations some data had to be calculated or extrapolated for the range of critical sideslip angles. The side force coefficient augmentation obtained would allow a 12% reduction in vertical tail area. A systems analysis study indicated that an aircraft drag reduction of 0.9% might be possible. The side force coefficient increase in the flight test was lower than observed in the full-scale wind tunnel test at equal or slightly less actuator output which was limited during flight test by the capability of the APU. Through CFD analysis it could be concluded that this was due to the wind tunnel floor, which changes the load distribution along the span, and due to the different Mach number which was 0.151 in the wind tunnel test and 0.176 for the flight test, changing the Reynolds number and the ratio of jet velocity to aircraft velocity.

Other experimental studies using active flow control at a VTP-type geometry were for example done by Cafarelli et al. in 2014 [55]. They used a scaled Boeing 737-like VTP

with a span of 0.4 m and 12 vortex generating jets (VGJ) along the span. They varied the rudder deflection angle as well as the sideslip angle. While the first variation without sideslip just led to a drag reduction, the second one with a change of the sideslip angle resulted in a small side force increase. They concluded that being able to realize higher jet to freestream velocity ratios than 2.5 would be a prerequisite for the VGJs to be effective. Other investigations utilizing VGJs were performed by Singh and Scholz in 2017 [56] on the same scaled generic VTP as used in this work. The VGJs were found to be capable to replace vane vortex generators and to significantly delay the flow separation on the deflected rudder. Using the same VTP geometry Löffler et al. applied pulsed blowing fluidic actuators [57, 58], demonstrating that they have an even higher ability to increase the side force coefficient as shown in a comparison of the methods in [59]. For the pulsed blowing actuators leading edge blowing was investigated in addition to the actuator position close to the hinge line used in the other investigations, leading to additional improvements at larger sideslip angles.

Numerical Investigations

Experimental results for AFC-enhanced vertical tails were presented in the studies mentioned above. In addition to experimental investigations also numerical studies were performed. Their main idea was to show that the experimental findings can be predicted in principle by simulations as well and to enhance the understanding of the interaction between the active flow control devices and the surrounding flow.

One publication using a CFD code for the prediction of active flow control on a 3D vertical tail was published by Vatsa et al. in 2014 [60]. They used the code PowerFLOW which is based on the Lattice Boltzmann Method (LBM). Besides the outside flow domain also the inside of the sweeping jet actuators was simulated and compared with the experimental findings from the small-scale wind tunnel test of Seele et al. [42]. While a better agreement with the wind tunnel test results could be found for the baseline case without actuation, the discrepancies were larger for the actuated case at a rudder deflection angle of 30° and a sideslip angle of 0° . Both sideslip angle and rudder deflection angle were varied. Even though the magnitude of side force and drag coefficient could not be predicted correctly for all cases, the trends found are in agreement with the experimental results.

Childs et al. published their work about the simulation of sweeping jets with the CFD code OVERFLOW in 2016 [61]. OVERFLOW was originally developed at NASA [62] and uses multiple overset structured grids. It solves the Reynolds-averaged Navier-Stokes (RANS) equations to simulate three-dimensional, viscous and compressible flows. The results were compared with the outcome of a wind tunnel test from a single actuator and with selected full-scale wind tunnel test results [49, 50]. A Mach number of 0.15 was used. Their aim was the development of a computational method to simulate sweeping jet actuation. First, computations of a single sweeping jet were performed. The results were used as input for the full VTP calculation as boundary condition for the actuation. This approach allowed a significant reduction in the computational time required. The results obtained with the implemented time-dependent sweeping jet inflow boundary condition are in good agreement with the experimental outcome, especially for the mean-flow characteristics. Larger discrepancies were observed for unactuated areas with separated flow.

This work was followed by Shmilovich et al. [63] also using OVERFLOW, now including the sweeping jet actuators and their simulation directly in the geometry. After validation with single actuators to properly model the choked conditions due to supersonic flow as well, this was applied to a comparison with the small-scale wind tunnel results by Seele et al. [42]. The investigation was then extended to full-scale flight conditions and the results were compared to the corresponding wind tunnel [49, 50] and flight test results [52]. Again the trends were captured well, but some discrepancies in terms of absolute values for the side force coefficient remained. As two main contributors to the remaining discrepancies the uncertainties in the experimental setup and the turbulence model accuracy for such complex time-varying and interactive flows were identified.

Another work of Shmilovich and Whalen [64] investigated the effect of higher air supply temperatures using OVERFLOW. This resulted in reduced mass flow for the same increase in the side force coefficient. One application case was sweeping jet actuators on a VTP, another steady blowing applied at a plain-hinge flap with a convergent-divergent actuator nozzle.

For the synthetic jets computational models were developed as well and then applied to a vertical tail geometry. For a study by Shmilovich et al. [65] the code OVERFLOW was adapted accordingly. The results were compared to the experimental findings of Rathay et al. [43, 44]. Steady blowing calculations were used in addition to the ones with a mainly sinusoidal signal at a frequency of 1600 Hz. In general, a good agreement with the measured data was observed but also some discrepancies. Especially for the calculations with only a small number of actuators and larger areas of separation the results derived using the actuation model show that the gains in the side force coefficient are underpredicted.

In contrast to the study by Shmilovich et al. [65] mentioned above, the main driver for a study by Jansen et al. [66] was the accurate prediction of the forces and not the computational cost. To gain a deeper understanding of the working principle of synthetic jets a coordinated experimental and computational approach was applied. The conditions of the low-Reynolds number wind tunnel test results [43] were used in the CFD calculations as well. Findings for the baseline flow without sideslip angle and one single active jet at the half-span position were presented. Using a delayed detached-eddy simulation (DDES) not only the change in the side force coefficient when activating the jet was predicted correctly but this time also the magnitude of the side force coefficient.

To summarize, partly substantial experimental and computational resources were invested to demonstrate the ability to apply and simulate active flow control devices at a 3D vertical tail. The main emphasis of the investigations was on sweeping jets and synthetic jets, but vortex generating jets and fluidic pulsed blowing actuators were considered as well. The tangential blowing approach, which is followed in this work, was not investigated for the application on the vertical tail so far. Different flow solvers were used to compute the effects of active flow control. However, the application of tangential blowing to the vertical tail was so far not studied using the TAU solver which is applied in this work. Here, the focus is on applying an existing and validated boundary condition, not its implementation. It is used to develop a tangential blowing design for use on a highly swept, low aspect ratio vertical tail for side force augmentation.

2 Simulation Setup

In this work the flow field around the vertical tail is simulated using numerical methods. Using a defined geometry of the vertical tail a mesh is generated which is the basis for the flow calculations. An overview of the flow solver is given in this chapter, followed by a description of the geometry and the mesh generation.

2.1 Flow Solver and Parameters

For the numerical flow simulations the TAU code is used. It is being developed by the German Aerospace Center DLR (Deutsches Zentrum für Luft- und Raumfahrt) in collaboration with German universities and the aircraft industry [67, 68]. The TAU code solves the steady or unsteady Reynolds-averaged Navier-Stokes (RANS) equations in two or three dimensions on hybrid grids. A viscous, compressible and fully turbulent flow is considered in this work. The TAU version 2015.1.0 [69] was used for all 2D and 2.5D investigations presented here and the version 2016.1.0 for the 3D investigations. Since the same settings are used, no changes in the resulting coefficients are expected but since the 2.5D results cannot be transferred directly to the 3D results a slight change in the coefficients would not change the outcome of this study.

The more general form of the RANS equations, the Navier-Stokes equations, is based on the conservation laws for mass, momentum and energy. Solving these equations directly for unsteady turbulent flow would require too much computational effort to allow it to be done in a reasonable time frame, even if only parts of an aircraft like a vertical tail would be considered. Thus some simplifications are introduced to make the simulation of turbulent flow feasible. With these, turbulence is averaged in certain time intervals by introducing a mean value and a fluctuating part of the velocity components, leading to the Reynolds-averaged Navier-Stokes equations. This approach leads to additional stress and heat fluxes in the Navier-Stokes equations, which necessitate the introduction of turbulence models, i.e. the turbulence is no longer resolved but modeled. In this work mainly a one-equation turbulence model developed by Spalart and Allmaras is applied (see Sec. 2.1.1), enhanced by a vortical and rotational flow correction (SARC).

As the RANS equations cannot be solved in closed form, they must be discretized in space and time and can thus only be computed at discrete points in the flow field. This requires the creation of a computational grid described in more detail in Sec. 2.3. Because the RANS equations are non-linear partial differential equations, they can only be solved by an iterative approach until a defined convergence criterion is fulfilled. For the spatial discretization a finite volume method is applied. The temporal discretization is realized by the semi-implicit Backward-Euler scheme with the linear Lower-Upper

Symmetric Gauss-Seidel (LUSGS) algorithm used here. The results are available on the surface and in the flow field.

For the calculations with blowing activated, an actuation boundary condition is specified at the upstream wall of the slot, which is the bottom of the plenum used to inject the jet into the flow domain. For this boundary condition a specification of jet velocity and density is necessary, with the latter assumed to be identical to the value of the flow in the farfield. When performing steady RANS calculations a constant blowing jet is used. This TAU boundary condition is described in [70] and was validated for numerical simulations with separation control by Ciobaca [40] whose approach in setting up the calculations is followed in this work.

When using pulsed blowing the jet is turned on and off in a regularly alternating manner. Thus, the solution is varying in time as well, necessitating the use of unsteady flow simulations. For unsteady computations the equations are integrated with a second-order backward differencing scheme in time employing the dual time-stepping approach by Jameson [71]. Here a physical time interval is specified based on the characteristics of the flow physics expected.

2.1.1 Turbulence Modeling

Most of the flow calculations described in the following chapters are based on the Spalart and Allmaras turbulence model [72]. It is a one-equation model which uses a single transport equation to close the Reynolds-averaged Navier-Stokes equations. From this type of one-equation turbulence models the SARC version is used specifically. This is the Spalart and Allmaras turbulence model enhanced with a vortical and rotational flow correction (SARC) based on the approach of Spalart and Shur [73]. For circulation control airfoils it was shown that this turbulence model leads to good results for flows with high streamline curvature [74].

Two additional turbulence models are studied and the results are compared in Sec. 3.3 and Sec. 3.5.1 with the SARC-based results to assess the influence of the turbulence model. One is the original Spalart and Allmaras (SAO) turbulence model in order to examine the effect of the additional rotation and curvature correction of the SARC turbulence model on the results. The other model employed for comparison is the seven-equation Reynolds stress model (RSM). Due to the increased number of equations, the RSM turbulence model is expected to have a higher accuracy for predicting complex flows such as those including high streamline curvature and separation. The drawback of this model is a considerably higher computational effort required for the flow simulation than for the one-equation Spalart-Allmaras turbulence model. The redistribution model selected for the RSM turbulence model calculations is SSG/LRR- ω including the calibration made for the TAU code in 2010, and the diffusion model is the generalized gradient diffusion hypothesis (GGDH) [75], also in the version from 2010.

2.2 Geometry

This section gives an overview of the geometry used for the investigation. All geometries are based on the same 3D VTP. For the two-dimensional investigations a section is

extracted from the 3D VTP. Furthermore, also a 2.5 geometry is employed which is generated from the 2D geometry through extrusion in spanwise direction.

The vertical tailplane investigated is similar to one of those used on a conventional transport category aircraft and is depicted in Fig. 2.1. This geometry was also the basis of the studies presented in [56, 57, 76]. The geometry of this research VTP for the numerical investigations is the same as the one used for the experimental investigations whose results were provided by the TU-BS for validation. Due to the requirement for symmetric behavior, the VTP uses a symmetric airfoil and also the rudder can be deflected symmetrically to both sides. The forward fixed part of the VTP is called fin and the deflectable aft part is the rudder. This VTP is scaled down to wind tunnel dimensions and used in this size throughout the study to allow a direct comparison between numerical and experimental results.

The span or height of the vertical tailplane is $b = 850$ mm. This size is selected to fit the geometry into the wind tunnel of the TU-BS (described in more detail in Sec. 3.4) and represents a compromise between maximizing the Reynolds number and still having acceptable interference with the surrounding wind tunnel walls. The aspect ratio is small compared to a wing which leads in combination with the large leading edge sweep angle to increased 3D flow effects. The rudder chord is 33% of the overall chord length. The sweep angle is $\phi_{LE} = 44^\circ$ at the leading edge and $\phi_{TE} = 25^\circ$ at the trailing edge. The rudder rotates around the hinge line. The rudder deflection angle investigated is 30° . i.e. a relatively large one. At this angle part of the flow on the rudder is already separated without active flow control.

For the 2D investigations a VTP section at 50% span is extracted from the geometry with 30° rudder deflection angle. This geometry is shown in Fig. 2.2. It is extracted at the position marked in Fig. 2.1 with the chord length c . From an aerodynamic point of view a 2D flow simulation gives results equal to a wing with infinite span and zero sweep. In a next step this 2D geometry is extruded in spanwise direction. This is then called a 2.5D approach and is depicted in Fig. 2.3. Because the 2.5D model also has an extension in spanwise direction, the effect of the large leading edge sweep angle can be captured in these calculations. The chord length is kept constant along the span. This allows the left and right boundaries of the calculated section to be defined as periodic boundaries, leading to the simulation of a swept lifting surface with infinite span. A top view is given in Fig. 2.4. The angle of the incoming flow to the leading edge is marked with ϕ . The chord length c in the freestream direction is kept identical to that of the 2D geometry. For the 3D simulations the VTP is placed on a plane with a symmetry boundary condition assigned to it.

Tangential blowing is realized by integrating a slot at the end of the fin as shown in Fig. 2.5. The slot height is varied as part of the investigation which will be presented in Sec. 4.1.3. The final slot height h_{slot} used is 0.0006 of the local chord length or written as the dimensionless slot height $h_{\text{slot}}/c = 0.0006$. This results in a relatively thin slot of approximately 0.3 mm for the 2D geometry. A part of the slot is modeled for numerical reasons [40]. The slot length l_{slot} is 20 times the slot height. It is chosen to ensure that a developed pipe flow is established at the outlet. The shell thickness above the slot towards the surrounding air is 0.1 mm for the 2D investigations. Looking at a real aircraft geometry the lip closing the gap from the fin to the rudder is also relatively small. For the 3D geometry this shell thickness was increased to 0.5 mm to comply with the manufacturing constraints for the wind tunnel model which was used to carry

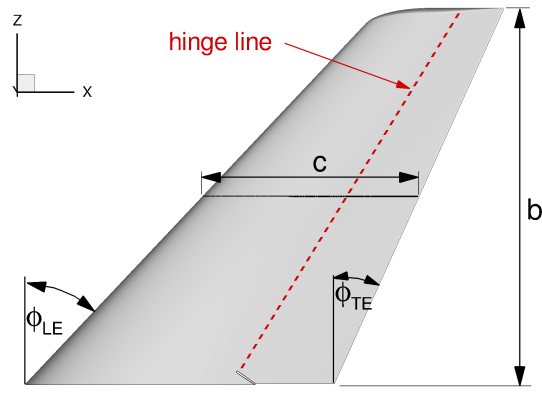


Fig. 2.1 3D VTP side view

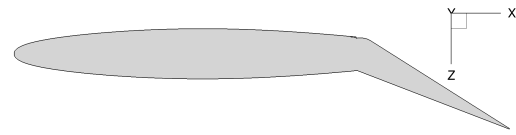


Fig. 2.2 2D airfoil

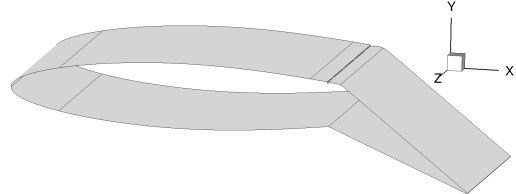


Fig. 2.3 2.5D VTP section

out the validation experiments. For the 2.5D geometry the continuous slot is replaced by discrete slots for some investigations. Examples of discrete slot geometries are visualized in Sec. 4.2.2.

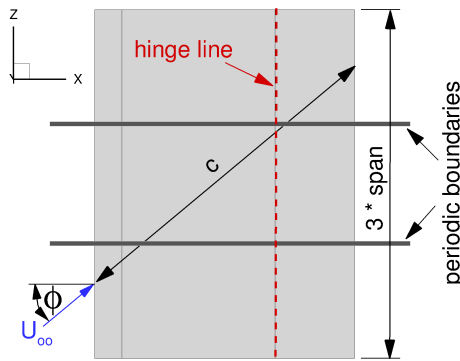


Fig. 2.4 Top view of the 2.5D VTP section. To allow a better illustration of the definition of the chord length c , three times the span of the computational model is shown.

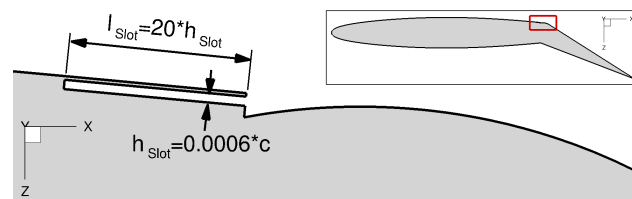


Fig. 2.5 2D airfoil with a detailed view of the blowing slot geometry; h_{Slot} : slot height, c : airfoil chord length, l_{Slot} : slot length

2.3 Mesh Generation

In this section some details about the mesh generation are described. To be able to conduct a flow simulation, the area around the geometry has to be divided in many small control volumes. For each control volume or cell the flow quantities are calculated. The aggregation of all cells is called mesh. The size of the mesh cells has to be adapted to

the local flow behavior and is e.g. refined in areas with rapidly changing flow quantities or around small geometric details. A mesh refinement study is conducted where the mesh is systematically refined. This helps to find cells sizes where the flow solution does not change any more when further reducing the cell size.

The mesh generation was done using the commercial software Centaur from CentaurSoft [77]. It creates hybrid meshes. The surface mesh is made of triangles and quadrilaterals. From this prisms or hexahedrons are growing into the field, building the near-surface mesh which is important for the resolution of the boundary layer. The remainder of the flow field is filled with tetrahedrons. For a 2D mesh the elements reduce to quadrilaterals and triangles. The slots themselves and also the rudder are meshed with quadrilaterals or hexahedrons wherever possible. In addition, the flow field above and behind the rudder is discretized with hexahedrons, essentially leading to a mesh with a structured appearance. Hexahedrons are less dissipative and should lead to a better preservation of the flow quantities. In this area separated flow for the cases without or with insufficient blowing and/or vortices due to the blowing jets is expected. An overview of the mesh in the vicinity of the VTP is given in Fig. 2.6, taking the mesh around the 2D geometry as an example.

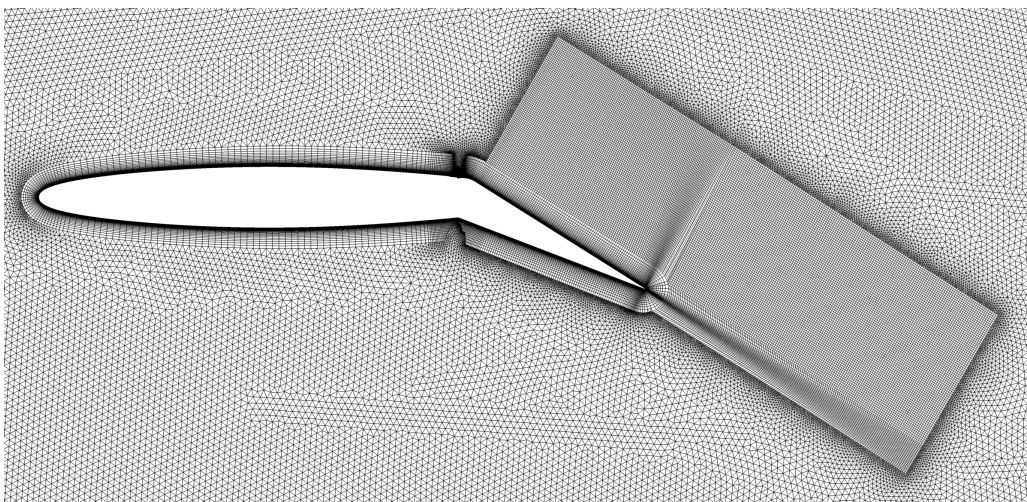


Fig. 2.6 2D mesh showing the hexahedron blocks used for field refinement.

Right aft of the slot the number of prism layers has to be reduced by the mesh generator in the corner of the step for geometric reasons. Here the mesh is created in such a way as to enable a rapid growth of the boundary layer-resolving semi-structured layers. This is shown in Fig. 2.7(a) and in a detail view in Fig. 2.7(b). Where the use of prisms or hexahedrons is not possible in this area, highly refined tetrahedrons are utilized.

The farfield of the mesh extends about 100 times the VTP chord length in each direction to minimize the effect of the farfield boundary on the accuracy of the results (see e.g. [78]). Such a distance is often used in similar investigations as for example in [79]. It ensures that the perturbations emanating from the airfoil geometry into the flow field decay sufficiently before reaching the farfield boundary where freestream conditions are assumed. For the 2.5D investigation the two parallel sides, which include the airfoil, are assigned a periodic boundary condition. Since the tangential blowing influences the boundary layer very close to the surface, this region is resolved well using a target dimensionless wall distance y^+ of 0.5. With 50 layers, the number of prism or hexahedron layers is also quite high compared to 25 to 30 layers used in

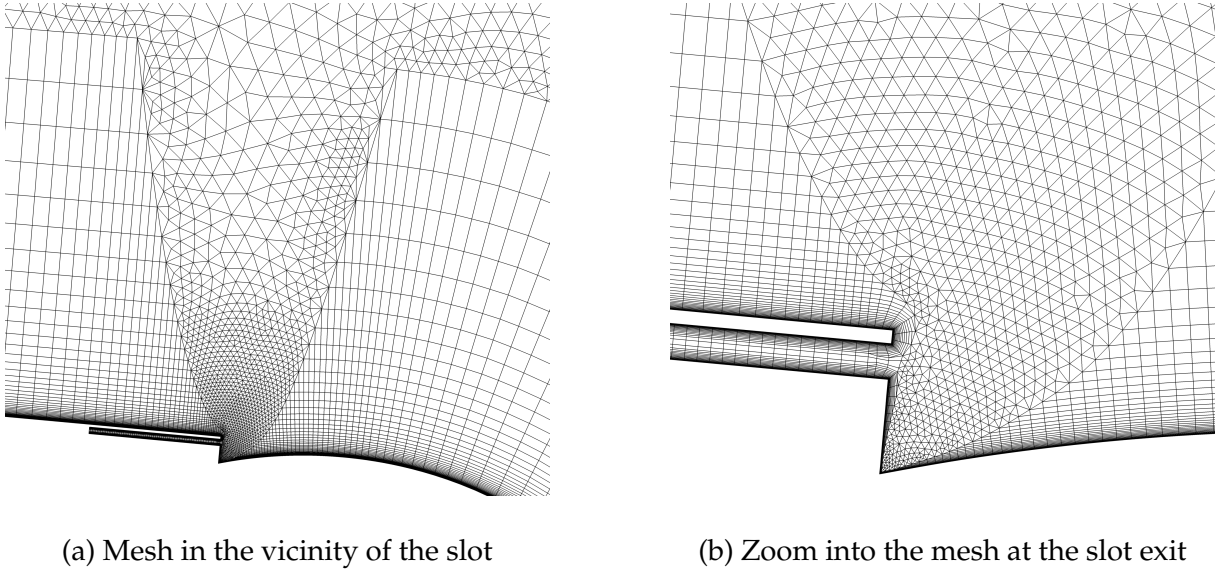


Fig. 2.7 Details of the 2D mesh

other investigations applying the same mesh generator and flow solver, e.g. [79]. The higher number of layers allows an improved resolution of the boundary layer, the thin jet ejected from the slot and of potential separated flow and small vortices. The total number of points for a 2D mesh is about 240000, for a 2.5D mesh about 7 million and for a 3D mesh about 77 million.

A grid convergence study is performed using the 2D mesh to investigate the influence of the spatial discretization on the results. It is based on the Richardson extrapolation [80] generalized by Roache [81] for arbitrary grid refinement factors and spatial orders of accuracy. Using this, a higher-order estimate for a solution based on a mesh approaching zero grid spacing can be obtained. Starting with a very fine mesh, three consecutively coarsened meshes were created. In this study the first cell height is kept constant for the coarsened meshes as well. Since for each turbulence model a recommended range of non-dimensional wall distances y^+ is targeted, which for the SARC model is in the range of 1, the first cell height and the resulting y^+ would become too large if they would be coarsened, too. An estimate for the infinitely fine mesh solution f_∞ is calculated by:

$$f_\infty = f_1 - \frac{f_2 - f_1}{r^p - 1} \quad (2.1)$$

Therein f_i is the solution obtained using the mesh refinement level i , with $i = 1$ representing the solution based on the finest mesh. The term r is the refinement rate and p the formal order of accuracy of the algorithm. The latter can be calculated if the solutions of three refined meshes and their refinement rate is available:

$$p = \frac{\ln\left(\frac{f_3 - f_2}{f_2 - f_1}\right)}{\ln(r)} \quad (2.2)$$

Since not structured but unstructured grids are used in this study, which need to be created independently, errors like a slightly differing refinement rate between the grids are introduced. This should be kept in mind when assessing the influence on the quantification of the numerical uncertainty. The results of the study are presented in Sec. 3.1.

3 Verification and Validation of the Numerical Setup

First a verification of the numerical setup will be discussed in this chapter. This includes the spatial discretization with the results from the mesh refinement study; the time discretization, which is important for the unsteady pulsed blowing results; and the influence of the turbulence model. The verification study is carried out using a representative 2D section. The flow conditions used here are a Mach number of 0.2 and a Reynolds number of $2.24 \cdot 10^6$ based on the extracted airfoil's chord length. The sideslip angle, usually referred to as angle of attack for 2D wing section investigations, is zero. In a subsequent step the numerical setup for the 3D investigation is validated by comparing the results to those obtained from a wind tunnel test using the same VTP model. As explained in the respective section the flow conditions are slightly changed leading to a Reynolds number of $1.885 \cdot 10^6$ at the mean aerodynamic chord of the vertical tail at a Mach number of 0.16. Here the sideslip angle is varied.

3.1 Influence of the Spatial Discretization

The results of the mesh convergence study concerning the behavior of side force and drag coefficient with varying mesh sizes are depicted in Fig. 3.1. The values are given as increments referenced to the value of the steady flow calculation based on the finest mesh without blowing. A mesh of a 2D section is used for this study. For this grid convergence study the results obtained with three different momentum coefficients are examined: $c_\mu = 0$ (no blowing), $c_\mu = 0.01$ with mostly attached flow and $c_\mu = 0.014$ with fully attached flow on the rudder. For the calculation result with fully attached flow on the rudder no significant differences in the side force or drag coefficient can be observed between the different meshes. The distinctions between the results become more obvious the more the separation is increased or the energy introduced by the blowing is decreased. For $c_\mu = 0$ it can be observed that the largest number of cells (left side in the diagram) also leads to the largest side force and drag coefficient created. No asymptotic behavior of the coefficients can be observed, but it should also be kept in mind that this kind of grid convergence study is strictly speaking only valid for fully attached flows. This is clearly not the case without blowing, where the flow over the rudder is fully separated.

Using Eq. (2.1) the error due to the spatial discretization $(c_S - c_{S,f_\infty})/c_{S,f_\infty}$ is estimated. Tab. 3.1 shows that for $c_\mu = 0.014$ and $c_\mu = 0.01$ the error tends towards zero but increases for the case without blowing to 1.6% for the fine mesh and is at about 13% quite high for the medium mesh.

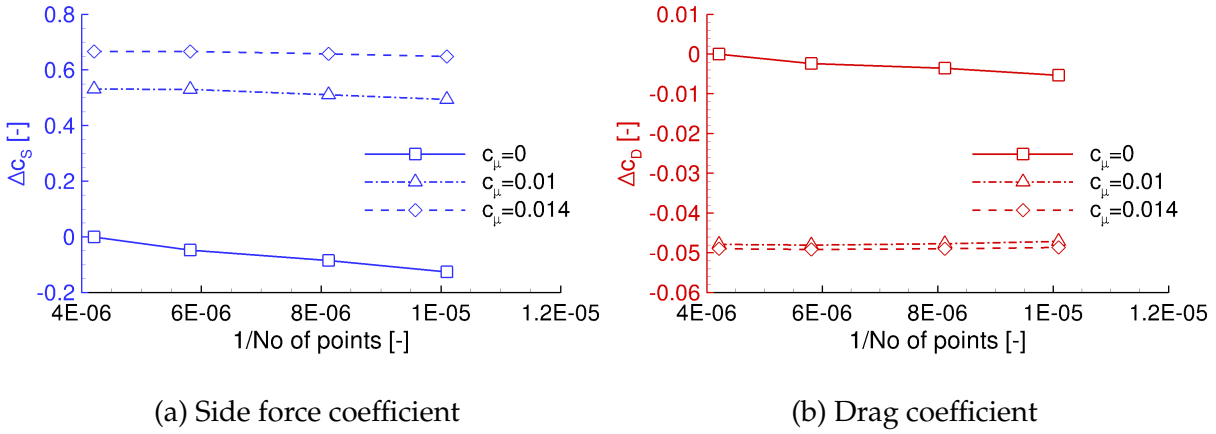


Fig. 3.1 Dependence of the grid resolution on the global coefficients for three different blowing ratios.

Tab. 3.1 Error estimates for the side force coefficient in [%] compared to an extrapolated solution with the grid spacing tending towards zero

c_μ [-]	0.014	0.01	0
fine mesh	$-9.3 \cdot 10^{-05}$	$-3.2 \cdot 10^{-03}$	-1.6
medium mesh	$-6.1 \cdot 10^{-03}$	$-6.0 \cdot 10^{-02}$	-13.2

In Fig. 3.2 the obtained side force and drag coefficients are depicted over the momentum coefficient. Results for three different momentum coefficients are shown connected by lines for convenience. This figure illustrates that the results without blowing vary dependent on the resolution of the grid. The more c_μ increases and the flow on the rudder attaches, the more the results approach each other. Especially for the investigations without blowing it is therefore important, if different geometries are compared, to keep mesh resolution and mesh characteristics as similar as possible to enable a better comparison.

The mesh convergence study yields that the second finest mesh should be sufficient for the larger momentum coefficients. However, it was also observed that the more the flow separation is increasing the more the mesh needs to be refined to reduce the influence of the spatial discretization on the results. Therefore it was decided to use the finest mesh for all calculations.

In addition to just refining the existing mesh topology, a study was conducted to assess the effect of other mesh parameters [76]. For this mesh study the same airfoil was used to generate a constant-chord, unswept low-aspect ratio 3D wing instead of an infinite-span wing. One side of the airfoil was placed on a symmetry plane. This three-dimensional meshing approach was used since it offered more flexibility and features in the mesh generation software. The symmetry plane of the resulting mesh was extracted and then used for a 2D flow simulation. The following was examined:

- Number of cells on the blunt trailing edge surface
- Field discretization using hexahedrons above and behind the rudder instead of tetrahedrons
- Refinement of the surface cells on and above the rudder and its trailing edge

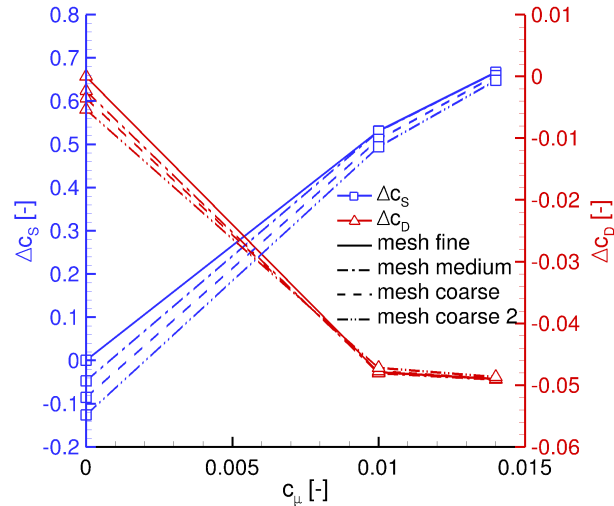


Fig. 3.2 Influence of the grid resolution on global side force and drag coefficients as a function of the momentum coefficient.

In this study it was concluded that for the variation of the number of cells on the trailing edge one cell leads to a significantly different result with no separation on the rudder compared to a mesh with more cells on the trailing edge where the flow is separated over the whole rudder. The results obtained show that six cells seem to be sufficient to get a robust behavior. For the 2D study the number of trailing edge cells was even increased to 24. For the next point, the topology of the field discretization in the area above and behind the rudder was investigated. Tetrahedrons are used in the common hybrid meshing approach above the near surface layer which is here composed of hexahedral elements. In areas where larger vortices are shed from the surface, they have to transition through this element type border, usually noticeable by an increased dissipation of flow quantities. Using directly-connected hexahedrons instead of tetrahedrons as elements for field discretization (cp. Fig. 2.6) avoids a change in cell type. This enables a smoother propagation of the flow quantities in vortex dominated areas. However, the overall effect on the coefficients calculated was rather small. Refining the cells on and above the rudder was found to have a small influence on the overall coefficients as well, resulting in differences below 2.5% for the side force and drag coefficient. It led to a better resolved near wall region and with that to an improved capturing of the vortices and the blowing jet. This observation led to the refined first cell height and increased number of the prism/hexahedron layers used for the meshes in this study.

With the 2.5D mesh a spanwise dimension is introduced. The mesh setup was created by transferring the setup from the final 2D mesh used. The results of the detailed 2D mesh convergence study were checked again in [82] to see if they apply as well after adding the discrete slots. A coarser and a finer mesh with scaling factors of 0.7 and 1/0.7 were created and investigated at different blowing velocities and for a large (16) and a smaller number (4) of slots. The maximum error compared to an infinitely fine mesh was determined to be about 5.8% of the side force coefficient for the medium/reference mesh. This corresponds to a configuration with low jet velocity and large slot spacing, where still large areas with separated flow exist. For all cases where blowing has a significant effect on the reduction of the areas with flow separation, the mesh dependency was found to be below 1%. It was generally observed that a finer mesh results in an increased

side force coefficient. The dimensionless first wall distance was also varied and it was concluded that a coarser first wall distance might be too coarse close to the slot exit. Therefore, the relatively fine value from the 2D study was kept.

The 2.5D mesh setup was then transferred to the 3D mesh and adapted along the span as necessary. The change of the chord length from root to tip is now taken into account. The size of the mesh cells is scaled depending on the chord length, so that about a constant number of cells per chord results. Extra refinement is additionally added around the tip of the vertical tail where the now finite span ends and at the bottom of the rudder where also a pressure exchange between suction and pressure side and the creation of vortices is expected. In 2D, the mesh dependency was found to be the largest without blowing as shown above. To check the mesh influence on the 3D results, the mesh was refined by a very large factor of 2.5. This resulted in no change of the side force coefficient without blowing as will be explained in Sec. 3.5.1.

3.2 Influence of the Time Discretization

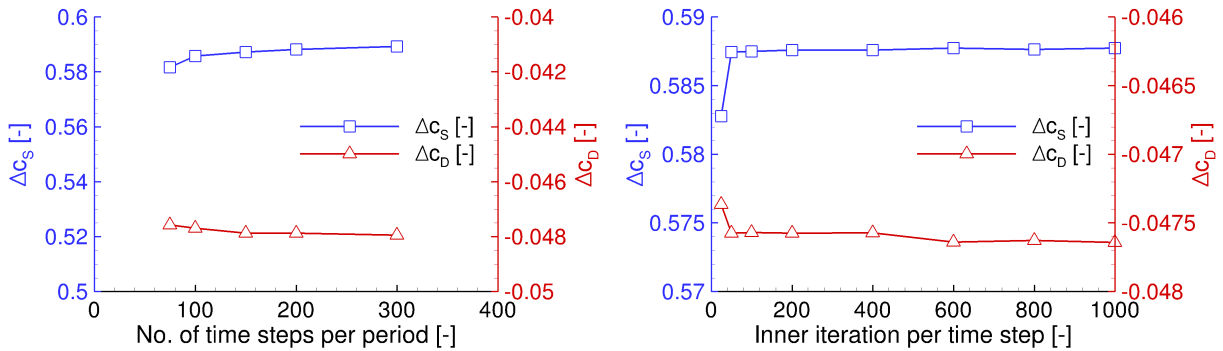
To determine if a solution can be used for further postprocessing, its convergence has to be analyzed. Apart from the normalized density residuum the global side force and drag coefficient are monitored. For the steady calculations with higher blowing momentum coefficients usually a monotonous convergence behavior can be observed. The convergence criteria for the 2D results is a change smaller than $1 \cdot 10^{-6}$ in the side force coefficient and smaller than $1 \cdot 10^{-5}$ in the drag coefficient for a constant range of 3000 iterations. The change in the coefficients is at least one order of magnitude smaller than the differences between variations that shall be compared. This is known to be necessary from experimental investigations as measurement accuracy in order to obtain reliable data [83, Sec. 2.3.3]. This allows to derive a robust ranking even when comparing configurations with very small differences, e.g. see Fig. 4.15 and there slot angles 8° and $8^\circ + 6^\circ$. For the 2.5D and 3D flow calculations this criterion is relaxed by one order of magnitude. Here the increased regions of separated flow along the span make the convergence more difficult. For calculations without or only very little blowing the rudder is to a large extent or even fully separated and thus exhibits a vortex dominated flow. This usually leads to an oscillatory convergence behavior. For such cases it is more difficult to determine if a calculation is converged. Here mainly the mean values of side force and drag coefficients are monitored. For the calculation of the mean value several oscillating periods are used to get a more relevant and representative average value and to reduce the impact of the start and end point of the slice of iterations selected in relation to the period start and end.

For the unsteady calculations the convergence in physical time needs to be considered additionally. Here, the general development of lift and drag coefficients over one actuation period is compared to adjacent ones. Cyclically reoccurring periods are identified which can usually be found if pulsed blowing is applied. For such a period the mean value of the aerodynamic coefficients is calculated and compared with the preceding ones. A 2D calculation is considered converged if the side force coefficient remains constant in the first three significant digits. For the drag coefficient the same applies but on the first four digits.

For the unsteady numerical simulations with pulsed blowing in addition to the grid

convergence study a sensitivity study was conducted where the time resolution and the number of inner iterations were investigated using the 2D section geometry.

To assess the resolution in time, the number of physical time steps for one actuation cycle is varied between 75, 100, 150, 200 and 300 leading to physical time step sizes between $3.173 \cdot 10^{-5}$ s and $7.933 \cdot 10^{-6}$ s. These are chosen such that the physical time for one actuation cycle corresponds to the time the flow at freestream velocity needs to travel over the rudder once. All computations are started from a converged steady-state solution with continuous blowing and use a high number of 1000 inner iterations for each computed physical time step. To study the impact of the temporal resolution the following parameters are fixed: momentum coefficient $c_\mu = 0.01$, dimensionless frequency $F^+ = 1$ and duty cycle $DC = 0.5$. In Fig. 3.3(a) the mean values of side force and drag coefficients are depicted versus the number of time steps used for one actuation period. It can be observed that a small number of 75 time steps leads to some deviations in the side force and drag coefficient compared to the result with the largest number of time steps. Using that value as a reference, the deviation for 75 time steps is about 0.4% in c_S and 1.7% in c_D . The difference decreases the more time steps are used. At 200 time steps per period it is below 0.1% for the side force coefficient and about 0.3% for the drag coefficient.



(a) Variation of number of time steps per actuation period (b) Variation of the number of inner iterations per time step

Fig. 3.3 Dependence of the temporal and iterative convergence on the global coefficients of a time-resolved simulation.

With a selected fixed number of 200 physical time steps per actuation cycle, a variation of the number of inner iterations performed per time step is conducted. In Fig. 3.3(b) it can be seen that fewer than 100 inner iterations lead to a noticeable difference in the results. The convergence of side force and drag coefficients during one physical time step improves up to 600 inner iterations. This is especially true for that part of the blowing period where the switch from blowing to no blowing occurs. This sudden change in the jet velocity also leads to a change in the side force coefficient. In general the changes in the side force coefficient are quite small. Increasing the number of inner iterations from 600 to 1000 leads to a change in c_S below 0.01% and in c_D below 0.1%. Since more iterations tend to stabilize the calculation when the jump in the coefficients occurs after turning the blowing off, 800 inner iterations per physical time step are selected for the calculations presented in the subsequent chapters along with 200 physical time steps per actuation cycle.

3.3 Influence of the Turbulence Model

The SARC turbulence model-based calculation results are compared with flow simulations where the original Spalart and Allmaras (SAO) turbulence model is used in order to examine the effect of the additional rotation and curvature correction of the SARC turbulence model on the results. Apart from these two one-equation turbulence models also the seven-equation RSM turbulence model is used for comparison. For this again the same 2D airfoil geometry is used as in the previous section.

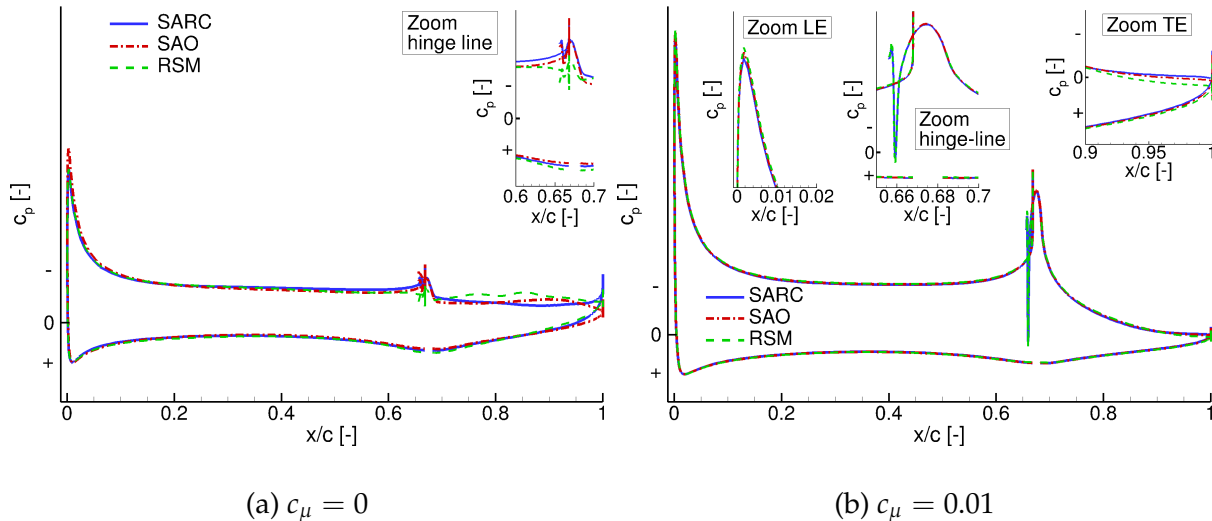


Fig. 3.4 Comparison of the pressure coefficient distribution for three different turbulence models

In Fig. 3.4 the pressure coefficient distributions are depicted over the non-dimensionalized chord length x/c for $c_\mu = 0$ and $c_\mu = 0.01$. A good agreement can be observed for the case with $c_\mu = 0.01$ in Fig. 3.4(b). The flow is attached apart from a small region near the trailing edge where also small differences in the results obtained with the different turbulence models can be found. As expected, the results are somewhat different if the areas of separated flow increase. Such flows are in general more difficult to predict reliably and the turbulence model has a strong influence. In Fig. 3.4(a) the results without blowing, i.e. with the rudder fully separated, are shown. The differences in C_p are mainly concentrated in the rudder area in this case as well.

These investigations show that small uncertainties are introduced into the simulation result depending on which turbulence model is chosen. Since no corresponding wind tunnel data are available for the investigation of the tangential blowing slots in 2D, it cannot be stated which of the models agrees best with experimental results. Based on experience documented in the literature, the SARC turbulence model was selected for the investigations presented later. It has been used several times for similar applications and has shown good agreement with experimental results [84], also as implemented in the TAU code [74]. For the 3D VTP some experimental data is available which is used to assess the influence of the turbulence model in Sec. 3.5.

3.4 Experimental Setup

For the validation of the numerical studies on the 3D vertical tail experimental results are consulted. This allows a comparison also for this highly three-dimensional flow including separations and a better view on the agreement with the turbulence model used for the numerical calculations. The experimental study was conducted in the “Modell-Unterschallwindkanal Braunschweig” (MUB) of the Institute of Fluid Mechanics of the TU Braunschweig. It is a closed-loop (Göttingen type) atmospheric wind tunnel. The maximum freestream velocity is 60 m/s. The closed measurement section has a size of 1.3 m times 1.3 m and a length of 3 m. To compensate for the growing of the boundary layer on the wind tunnel walls, the measurement section floor and ceiling diverge downstream by an angle of 0.2° . The turbulence level is about 0.2% at a flow velocity of 53 m/s. The wind tunnel is driven by a 300 kW direct current voltage motor. The same vertical tail geometry at the same scale as in the numerical study was used for the experimental investigation as well. The model is manufactured from carbon fiber reinforced plastic and aluminium. It is attached to a turntable which is part of the wind tunnel floor. Thus it can be rotated to enable a variation of the sideslip angle.

The measurements were done at a flow velocity of 57 m/s, corresponding to a Mach number of 0.16, with the temperature in the measurement section held constant at about 36°C . This leads to a Reynolds number at the mean aerodynamic chord of the vertical tail of about $1.88 \cdot 10^6$ at a reference length of 0.5285 m. At the fin’s leading edge a zig-zag shaped tape is placed to ensure a fully turbulent boundary layer which is also present in the numerical investigations and which is assumed to be the case for full-scale flight conditions.

The wind tunnel model is equipped with 166 pressure taps in six sections. The location of the sections is shown in Fig. 3.5. The distance between the taps is reduced close to the leading edge of fin and rudder to better resolve the suction peaks at these positions. An under-floor mounted balance is used to measure side force, drag and moment about the longitudinal axis of the vertical tail. For each data point 1000 samples were taken with a sampling frequency of 100 Hz. The accuracy of the pressure transducers is 17 Pa.

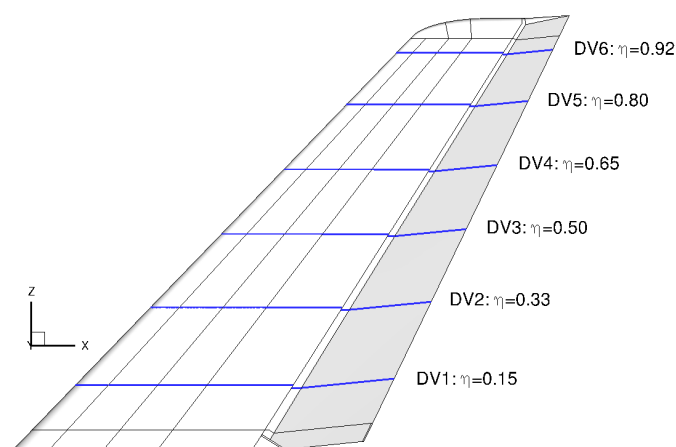


Fig. 3.5 Pressure measurement sections of the wind tunnel model.

For the actuation six separate regions in spanwise direction exist for which the mass flow rate can be controlled individually. The slot height was adjusted to fit the one

from the numerical investigation as close as possible. A conservative estimation of the maximum slot height deviation is ± 0.01 mm with the maximal slot height being 0.45 mm at the root and 0.22 mm close to the tip. Apart from the force and pressure measurements, oil flow visualizations were made for a few selected flow conditions. More details can be found in the description of the experiments by Singh [85].

The surrounding wind tunnel walls lead to a constriction of the flow passing the wind tunnel model. This constriction accelerates the flow around the model, which would not occur in free-flight conditions. This is called solid blockage effect. The blockage is calculated by the projected area of the model onto the wind tunnel exit divided by the cross section area of the wind tunnel. The blockage effect increases when the rudder is deflected and the sideslip angle is increased which is realized in the wind tunnel by rotating the model using the turntable. In the literature it is usually stated that the blockage should be below 10% [86]. For the VTP with 30° deflected rudder the blockage is 4.6% for a sideslip angle of 0° and about 7.5% for a sideslip angle of 9°. These values are still well below the limit of 10%.

Other wind tunnel effects changing the flow compared to a free flying model are wake blockage, straightening of the streamline curvature and buoyancy. The wake blockage arises since the wake of the model with its reduced velocity has a similar effect as a solid body. This leads to an acceleration of the flow outside of the wake due to the presence of the wind tunnel walls. The effect called buoyancy is due to the growth of the boundary layer along the wind tunnel walls which is equivalent to a contraction leading to an acceleration of the flow, causing a drop in the static pressure. This effect is reduced in the MUB due to an increase of the sectional area inside the measurement section through inclining ceiling and floor by 0.2°. In addition, the wind tunnel walls artificially straighten the curvature of the streamlines around the model. This leads to an increase of the angle of attack, increasing the side force coefficient of the model compared to a free flight model. From the wind tunnel test only the raw, uncorrected data is available which is used for comparison with the CFD results.

3.5 Comparison of Numerical and Experimental Results

In this section the comparison of the numerical and experimental results is presented to assess the validity of the numerical approach used. Compared to results shown in Sec. 4.3 a small part of the blowing slot at the tip is deactivated. This area is affected by the tip vortex and has been shown not to contribute much to the gain in side force. It was therefore not used during the wind tunnel test campaign. This made the slot integration with the very limited space in the tip sections easier and also led to an efficiency increase since mass flow rate could be saved for the same gain in side force coefficient.

Since the mass flow rate is directly available from the wind tunnel measurements, this value is used to compare to CFD results at the same mass flow rate. Since the CFD mass flow rate was the target value during the wind tunnel measurements, a good comparison is possible. The CFD results were used to design the tangential blowing slot, which was then later investigated in the wind tunnel. So all numerical results were obtained before the experimental results with blowing were available. For the 3D baseline flow, however, some experimental data were available beforehand and used for understanding and selecting the numerical approach for the 3D calculations.

All wind tunnel test results shown in the following sections were provided by the TU Braunschweig (TU-BS).

3.5.1 Baseline Configuration Without Blowing

At first, emphasis is put on understanding the baseline configuration without blowing. The typical planform parameters of a 3D vertical tail with large rudder deflection with its highly three-dimensional flow on the rudder make this configuration challenging. Results from previous wind tunnel test campaigns with the baseline configuration were available to compare to the CFD results and are shown in Fig. 3.6 as black or dark lines. In this figure the side force coefficient increment ΔC_s is depicted vs. the sideslip angle β . The increment is referenced to the value obtained with the SARC turbulence model at zero sideslip angle. Some variations are visible between the first two wind tunnel campaigns while the second and third, which are the most important ones for the comparison with the activated blowing slots, are in good agreement. This highlights that the absolute values from the experiment can vary and that factors like the consistency in the setup of the geometry and the measurement system might play a role.

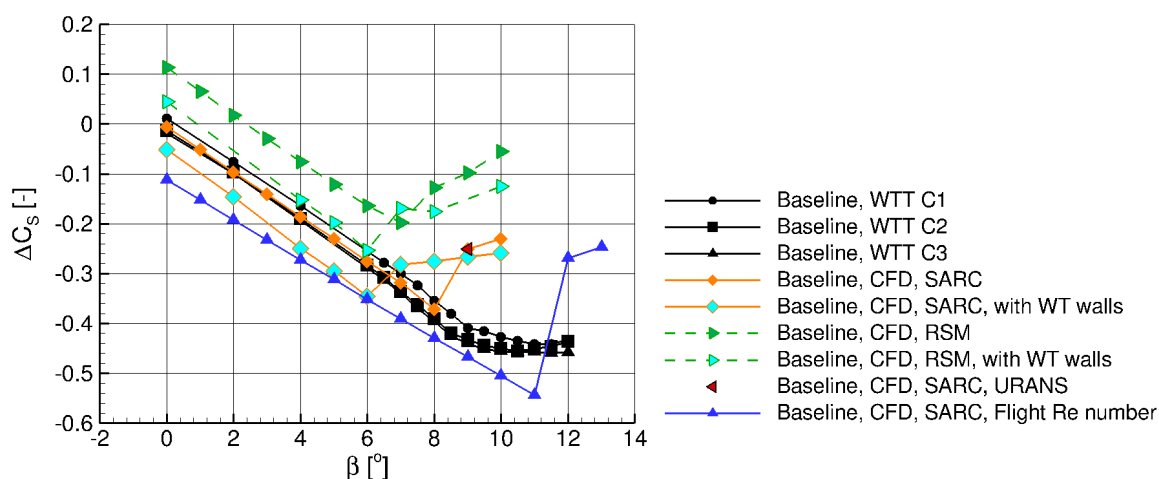


Fig. 3.6 Side force coefficient versus sideslip angle, 3D VTP, baseline configuration, various calculation proceeds, wind tunnel test results by TU-BS [56, 59, 85, 87]

For the numerical approach based on RANS-simulations two different turbulence models are used. These are the one-equation Spalart-Allmaras turbulence model with additional rotation and curvature correction (SARC), which has shown good agreement in other investigations (see Sec. 3.3), and the seven-equation RSM turbulence model. The vertical tail is mounted on an inviscid base plate with a symmetry boundary condition and simulated without modeling the surrounding wind tunnel walls. The RSM results show quite a bit of oscillation in the convergence of the coefficients. These were averaged to obtain the mean values given here. It can be observed that the RSM-based curve has the same gradient as the SARC-based result but a significantly reduced side force coefficient and also an earlier side force breakdown.

The SARC curve lies in principle on the wind tunnel results of the last two campaigns. The results were obtained by computing the subsequent sideslip angle always as a restart from the previous angle. The largest difference is the behavior at large sideslip

angles. Here, the CFD result features an abrupt breakdown of the side force coefficient while the side force gradient reduces gradually in the wind tunnel result before the level of C_S plateaus. Despite this difference, the same stall mechanism was found in CFD and experiment with a leading edge separation at the tip of the fin. This can be observed in a surface plot of the CFD result in Fig. 4.47 and in the following two sets of pressure coefficient distributions comparing CFD and wind tunnel test in Fig. 3.7 and Fig. 3.8. These figures show the six sections where pressure information is available in the experiment for three different sideslip angles. At 0° and 7° a good agreement between wind tunnel test and CFD results can be observed while at 10° some deviations are visible. At this sideslip angle the stall causing the side force breakdown has already happened in the numerical simulations. For the CFD results, the C_p -values at 10° sideslip angle are less negative on the fin in the upper sections on the suction side than at 7° . For the wind tunnel results, the values at 10° show that the suction peak has vanished as well, but that the C_p has become more negative downstream, partially offsetting the loss in the suction peak, leading to the more gradual stall observed in Fig. 3.6. Looking now just on the results for the 10° sideslip angle, in the experiment more negative C_p is generated on the suction side, thus leading to a higher side force as in the CFD results. In addition, the spanwise extent of the fin separation is smaller in the experimental results, contributing further to a more gradual side force reduction.

To investigate the reason for the different behavior of the C_S vs. β curve at high sideslip angles a few variations in the CFD approach were examined, including a change of the multi-grid scheme and a variation in the Courant-Friedrichs-Lewy (CFL) number which limits the time step size for each cell in order to keep the semi-implicit LUSGS scheme stable. Furthermore, also simulations which include the viscous wind tunnel walls were performed using both the SARC and the RSM turbulence model. These lead to an offset of the C_S vs. β curve and also to a small increase in the gradient of the curve. It can be observed that the stall occurs now at an even lower sideslip angle — although it could be argued that the stall is also a bit less abrupt and slightly closer to the behavior seen in the experiments. However, in the region of linear C_S -increase the sectional pressure coefficient distributions from the SARC-based computations without wind tunnel walls still exhibit the best agreement to those from the wind tunnel test.

To visualize this, the pressure coefficient distributions representing the RSM turbulence model results are added to those obtained with the SARC turbulence model and to the wind tunnel test results for the sideslip angles 0° and 7° in Fig. 3.9 and for the sideslip angles 0° and 10° in Fig. 3.10. The RSM turbulence model results are the ones with the simulated wind tunnel walls shown in Fig. 3.6 where the side force coefficient vs. sideslip angle curve is the second-closest to the wind tunnel results. For the lowest section the main differences of the RSM C_p -distribution are on the rudder for both small and large sideslip angles. Moving to higher sections along the vertical tail span also differences on the fin become more apparent, leading in most cases to less negative C_p -values compared to the wind tunnel results and also to the SARC-based results at $\beta = 7^\circ$ and $\beta = 10^\circ$. The earlier stall observed for the RSM turbulence model results is reflected in a reduction of the fin leading edge suction peak. Thus, not only the side force coefficient of the SARC-based results shows a better match to the wind tunnel results but also the pressure coefficient distributions.

Since the turbulence models were designed for attached flow only, the separation might not be predicted correctly. Furthermore, the results shown are from a steady calculation

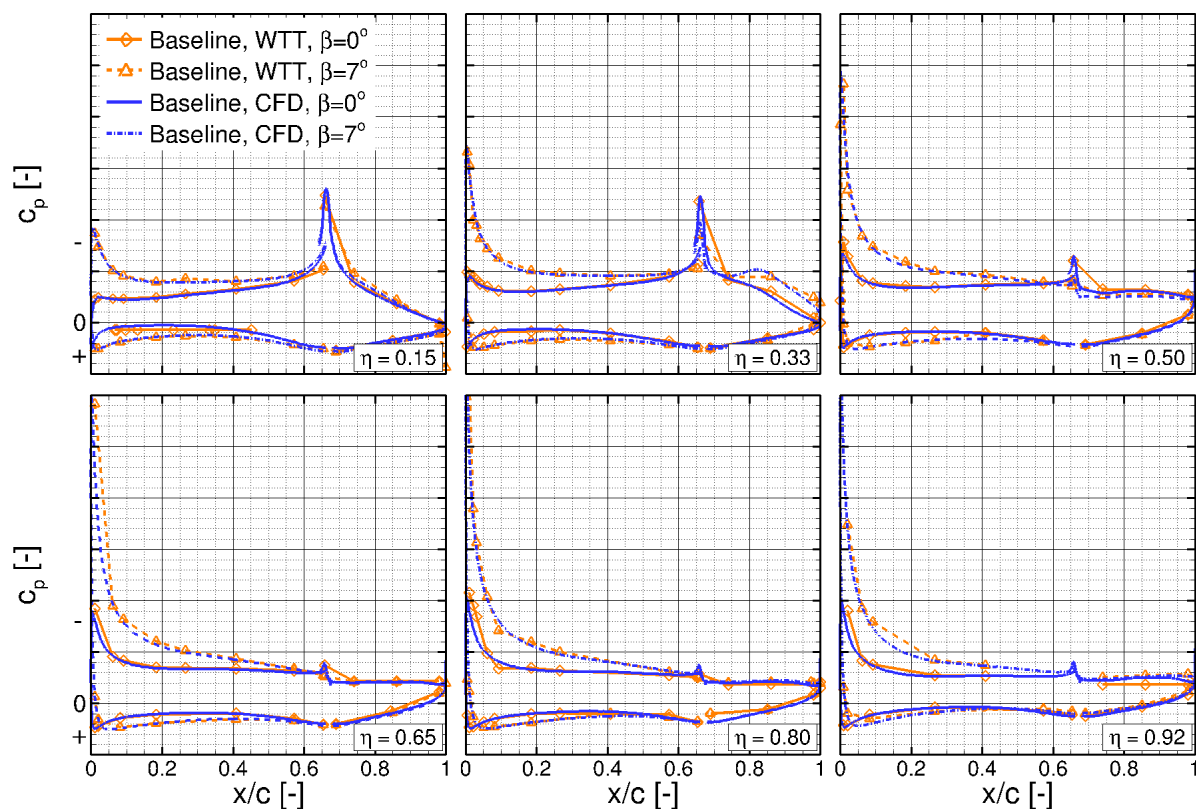


Fig. 3.7 Sections of pressure coefficient distribution, 3D VTP, baseline configuration compared to wind tunnel results provided by TU-BS [85], $\beta = 0^\circ$ and $\beta = 7^\circ$

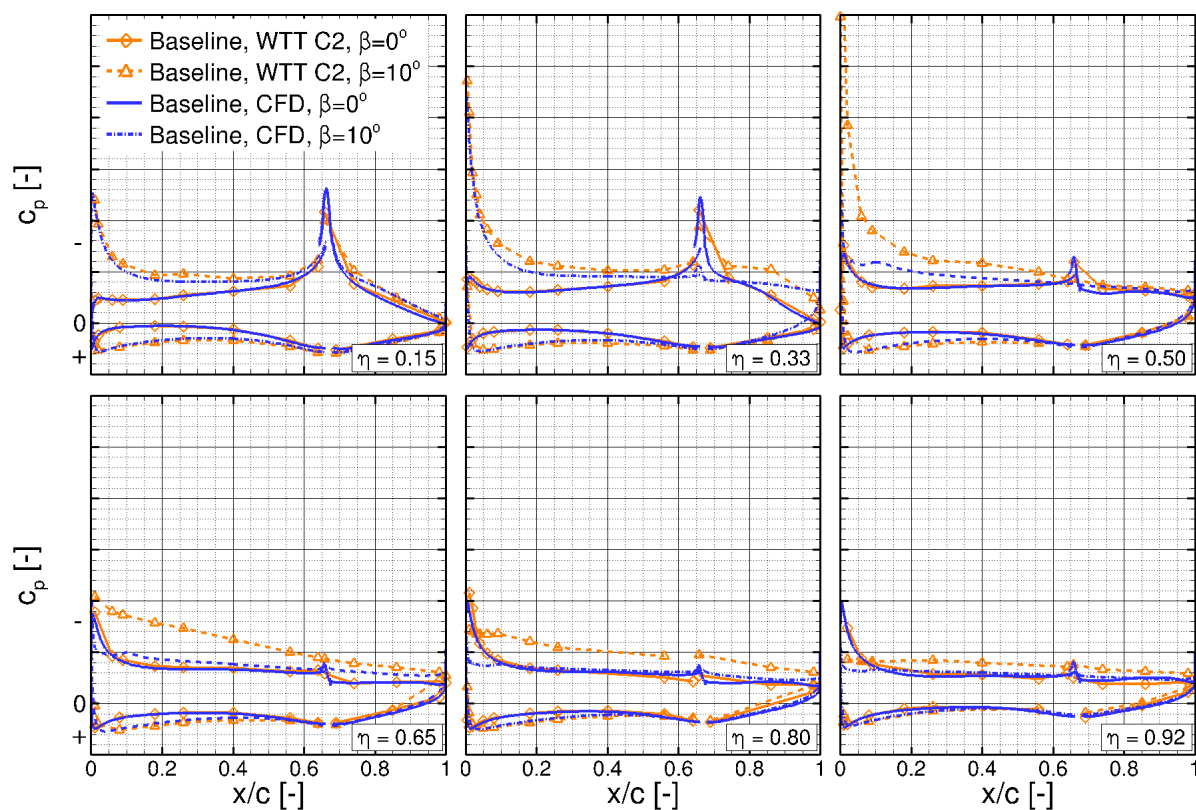


Fig. 3.8 Sections of pressure coefficient distribution, 3D VTP, baseline configuration compared to wind tunnel results provided by TU-BS [85], $\beta = 0^\circ$ and $\beta = 10^\circ$

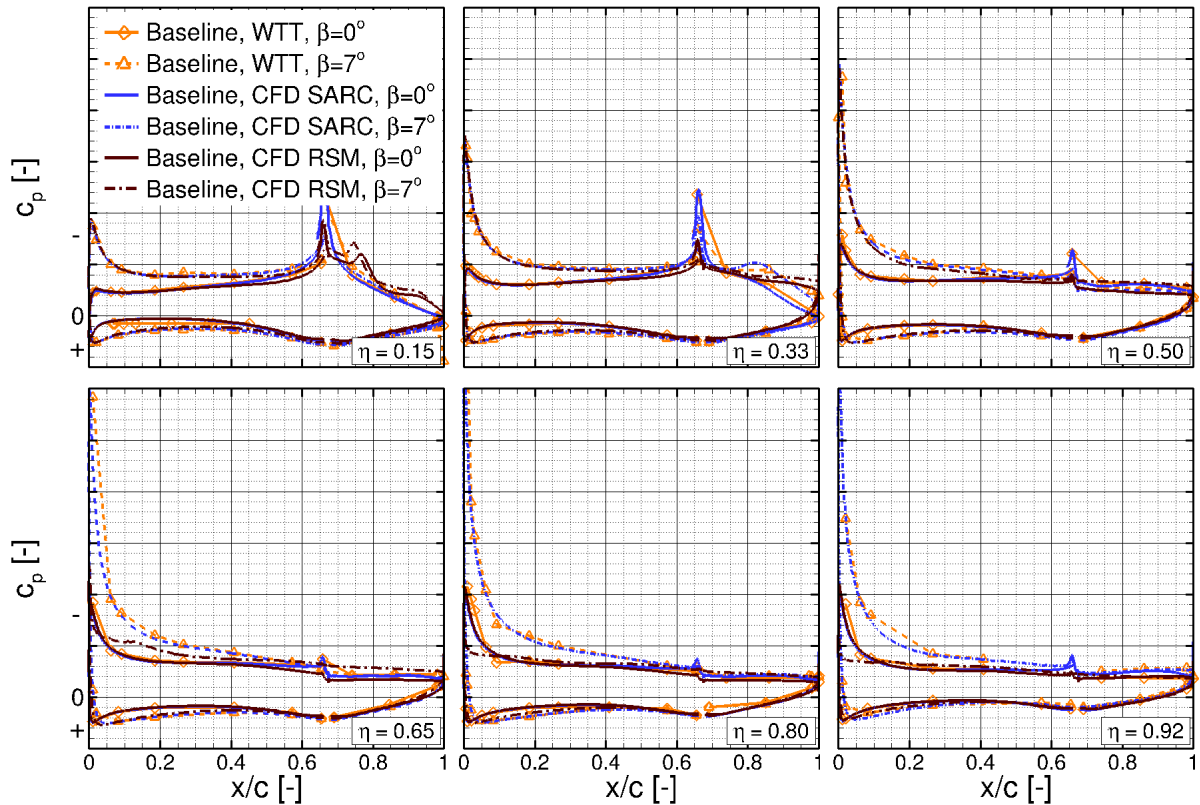


Fig. 3.9 Sections of pressure coefficient distribution for SARC and RSM turbulence model results, 3D VTP, baseline configuration compared to wind tunnel results provided by TU-BS [85], $\beta = 0^\circ$ and $\beta = 7^\circ$

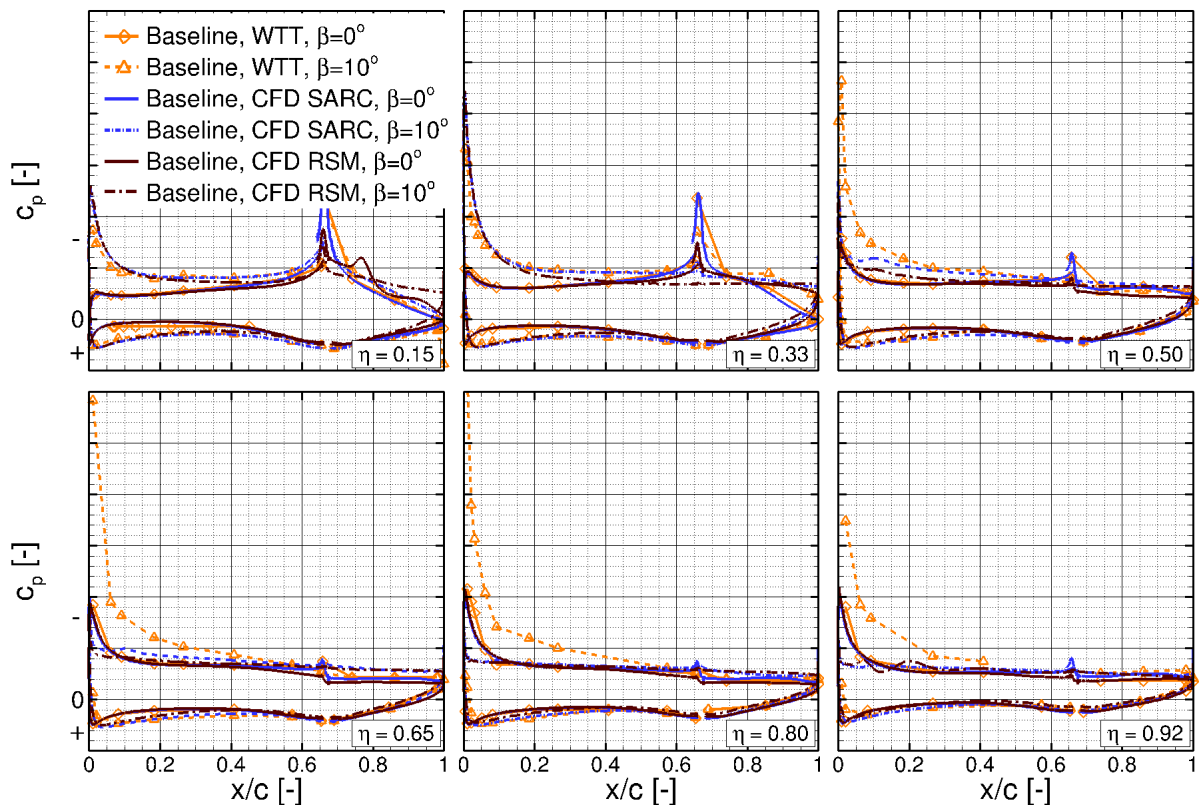


Fig. 3.10 Sections of pressure coefficient distribution for SARC and RSM turbulence model results, 3D VTP, baseline configuration compared to wind tunnel results provided by TU-BS [85], $\beta = 0^\circ$ and $\beta = 10^\circ$

and separation is an inherently unsteady phenomenon. Therefore, an unsteady RANS (URANS) calculation is performed for the sideslip angle where the side force breakdown occurs, started from a converged steady solution of a smaller sideslip angle in the linear range. This resulted in the same stall behavior, though. The decrease in C_S is quite similar and shows this abrupt loss in side force as well.

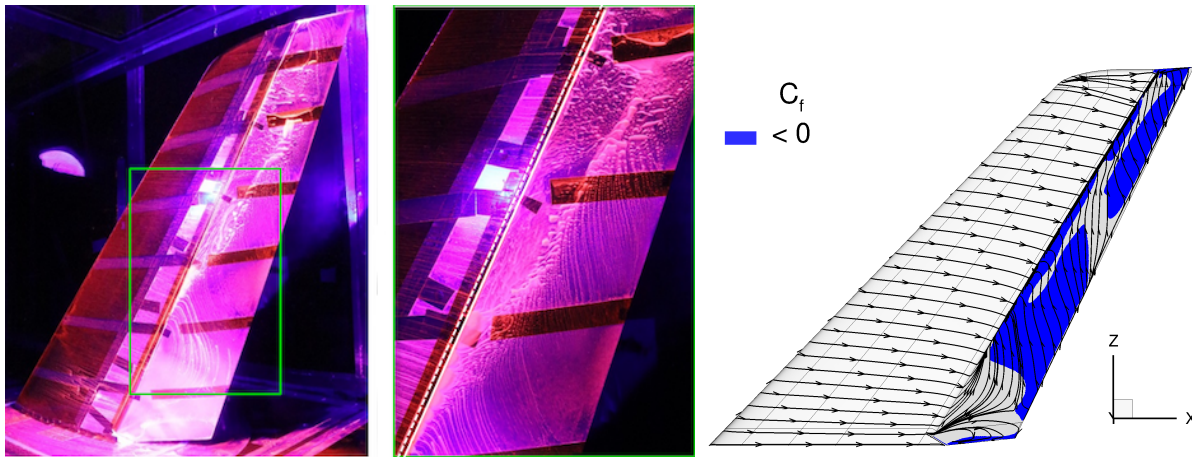
It was also checked whether the already fine mesh resolution might still be too coarse to capture some effects. A significant increase in the number of mesh points by a factor of about 2.5 was realized with an emphasis in refining not only the rudder but also the fin. This again did not lead to any noticeable differences in the results. Neither the side force changes nor does the C_p -distribution or the stall behavior.

It was also investigated if this sudden stall might be an effect triggered by the small Reynolds number compared to full-scale flight conditions. This was also found not to be the case. For the flight Reynolds number the stall behavior is the same but occurs at higher sideslip angles.

All investigations described above could not reveal the cause for the difference in the stall behavior between wind tunnel test and CFD. For the design of the blowing slots the linear part of the side force increase is more important. In this area the largest increase in C_S can be achieved. Here, the SARC turbulence model without wind tunnel walls leads to the best agreement. It has to be kept in mind that the wind tunnel results are not corrected for wind tunnel effects. However, this is in general only done for the force coefficients. The C_p -distributions in particular agree quite well for the approach chosen. They are normally not corrected, although a correction of the sideslip angle and flow conditions might lead to an offset in the sideslip angle where the results are compared. The surface flow topology of the wind tunnel oil flow visualization and the CFD skin friction lines agree well as shown in Fig. 3.11. The flow pattern especially in the lower third of the rudder is very similar with the streamlines at the bottom going first towards the trailing edge and then turning in a curved route towards the hinge line. In the upper part of the rudder there is a separation line in the wind tunnel oil flow visualization at about one third of the rudder chord moving a bit downstream further towards the tip which is not visible in the CFD results. Here the discrepancy might be due to the turbulence model or small differences in geometry or flow conditions. In the CFD solution the flow separates already at a more forward position directly at the step from fin to rudder caused by the slot integration. The aft part of the rudder looks again very similar with skin friction lines going in the same upward direction as in the wind tunnel test visualization. In summary, due to the good overall agreement of the SARC turbulence model-based free-flight simulations as shown above, this setup is used for the design of the blowing slots by numerical methods.

3.5.2 Blowing Slot Configurations

This section shows the comparison of wind tunnel and CFD results when blowing is active. The curves for the side force coefficient versus sideslip angle are depicted in Fig. 3.12(a) for the continuous slot and in Fig. 3.12(b) for the discrete slots. As it will also be explained in Sec. 4.3 dealing with the 3D slot design, the side force coefficient increases with increasing mass flow rate and/or jet velocity. The curves are basically offset to higher magnitudes of C_S . The higher the mass flow rate, the higher the side force gain becomes. The dashed lines represent the wind tunnel results provided by the



(a) WTT, zoom on the rudder on the right, oil flow visualization from [88]

(b) CFD, skin friction lines

Fig. 3.11 Side view of the vertical tail with comparison between wind tunnel test (WTT) and CFD, baseline configuration, $\beta = 0^\circ$

TU-BS. In principle, the numerical results predict the same trend as the wind tunnel results. In general the stall angle varies a bit by 0.5° to 1° . Since the step size in the sideslip angle is just 1° in CFD, part of the deviation could be due to the discretization in sideslip angle. Also deficiencies in the turbulence model to predict the stall precisely as well as small differences in geometry or flow conditions could contribute to the slight differences in the stall angle. Overall, the stall characteristics are now the same for CFD and wind tunnel with a sudden decrease in the side force magnitude to a value closer to that of the respective baseline configuration without blowing.

For the continuous slot the cases with higher mass flow rate agree quite well in absolute values as well as in the side force gradient in the linear side force regime. For the two smaller mass flow rates CFD over-predicts the side force gain compared to the wind tunnel test results. This is investigated in more depth by comparing the pressure coefficient distributions for zero sideslip angle exemplarily for a low and a high mass flow rate in Fig. 3.13. For the low mass flow rate the flow is not fully attached on the rudder. In CFD, this leads to very small oscillations in the convergence which originate from a change in the solution at the tip of the rudder, indicating a certain level of unsteadiness there. This unsteadiness might cause the different C_p -distribution at the tip section, but this cannot be seen in the time-averaged results from the wind tunnel test. Apart from that, the wind tunnel test results and the ones from CFD agree quite well, both for the low and the high mass flow coefficient. Also, the surface skin friction lines of the numerical results and the oil flow visualization from the experiment exhibit good agreement as can be seen in Fig. 3.15. Thus, CFD seems to be capable of predicting the experimental results for the continuous slot quite well.

For the discrete slots configuration the side force coefficient in Fig. 3.12(b) agrees well between CFD and wind tunnel test results for the lower of the two mass flow rates. For the larger mass flow rate, where the jet velocity is already close to the speed of sound, the side force gain in CFD is a bit smaller than measured in the wind tunnel test. However, the comparison of the pressure coefficient distributions for the case at

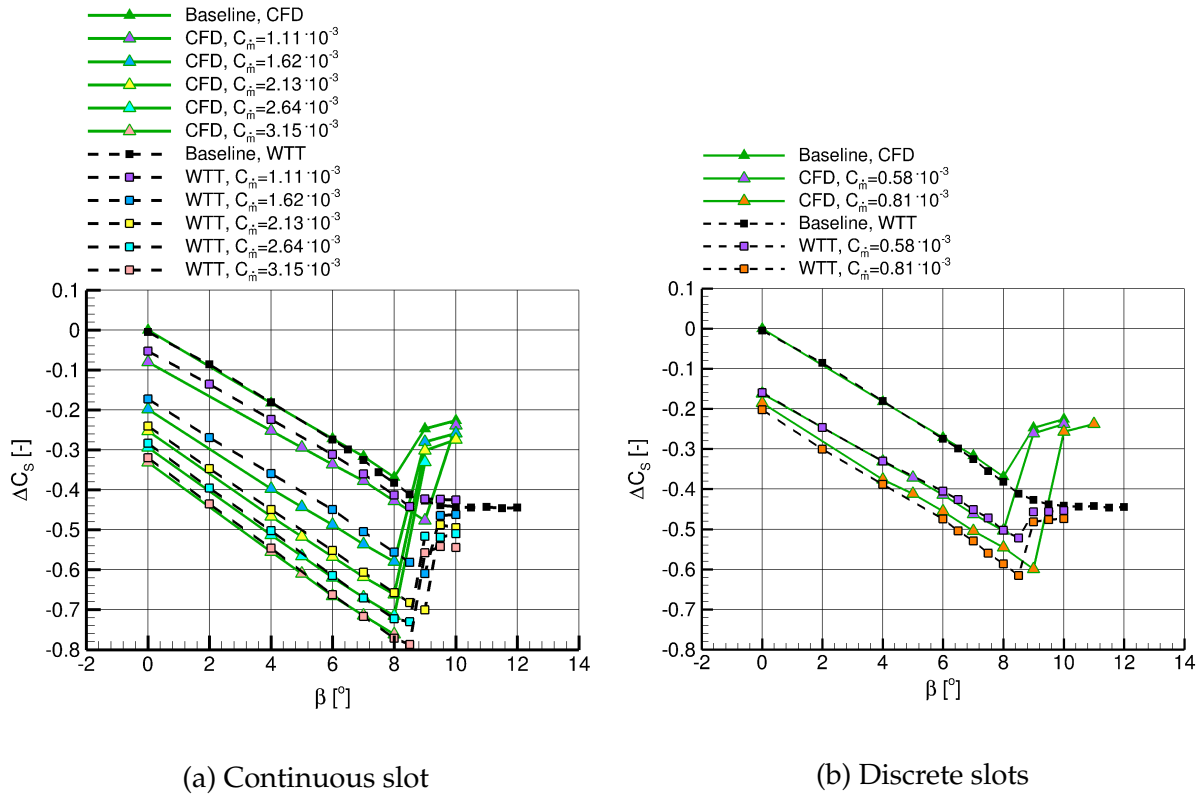


Fig. 3.12 Side force coefficient versus sideslip angle, 3D VTP, comparison between wind tunnel test results provided by TU-BS [85] and CFD.

higher mass flow rate shows again a good agreement of the numerical and experimental results as documented in Fig. 3.14.

Especially the sections on the lower half of the vertical tail fit well while for the upper half a slightly more negative pressure on the suction side of the fin can be seen in the experimental results. This might be the reason for the larger side force coefficient predicted in the experiment. Also, for some sections on the rudder suction side the CFD results depict some bumps in the C_p -distribution due to the vortices caused by the discrete jets. This cannot be seen in the wind tunnel test results. A reason might be that the results in the wind tunnel are time-averaged. If the vortex is moving during the averaging time or/and the discretization of the pressure taps is too sparse to capture such effects it would not be visible in the measurements. Overall, the effect of the discrete slots is captured quite well in CFD what can also be seen in the comparison of the oil flow visualization and the skin friction lines shown in Fig. 3.16. The small separation between the jets of two adjacent slots close to the rudder shoulder, which become more irregular towards the tip, can be found in both.

3.6 Summary

The influence of spatial and time discretization on the CFD simulation results was investigated and an adaptation of the mesh and parameter setting done according to the outcome. With regard to the turbulence model no final conclusions could be drawn

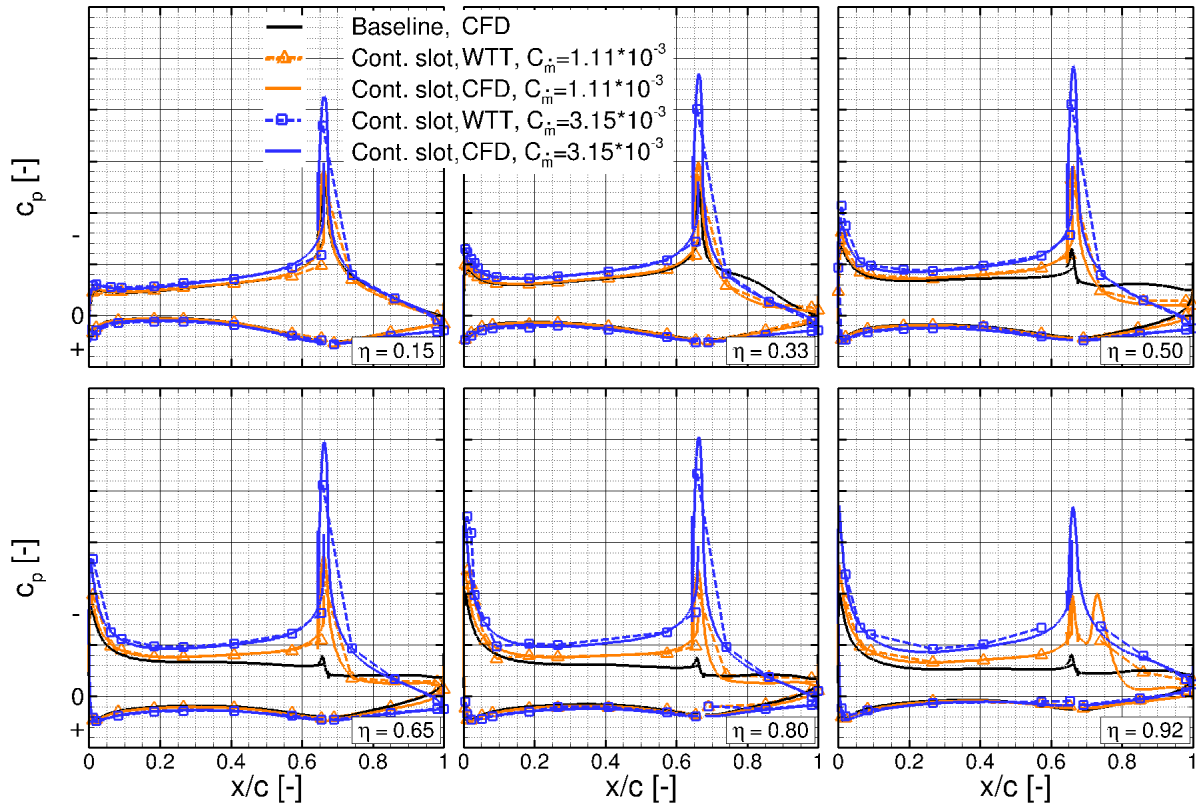


Fig. 3.13 Sections of pressure coefficient distribution, 3D VTP, comparison with wind tunnel results provided by TU-BS [85], $\beta = 0^\circ$, for two different mass flow coefficients C_{m_i} , continuous slot

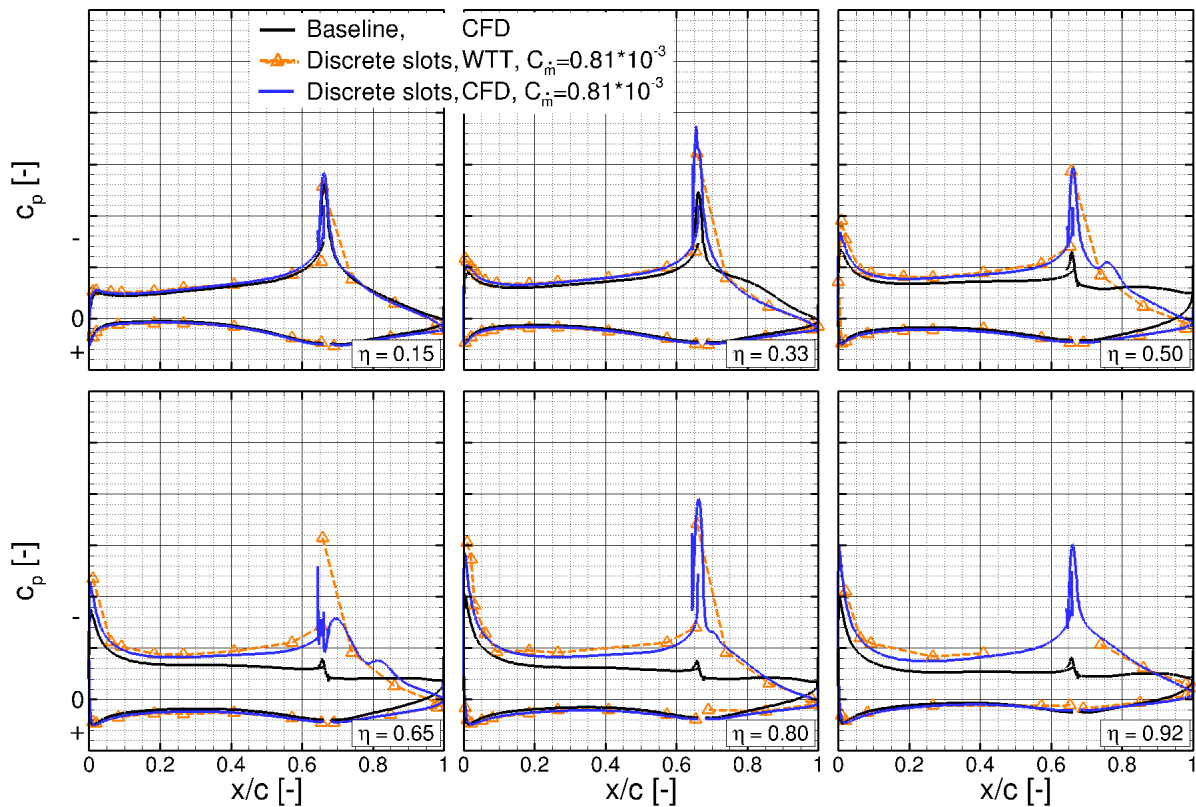
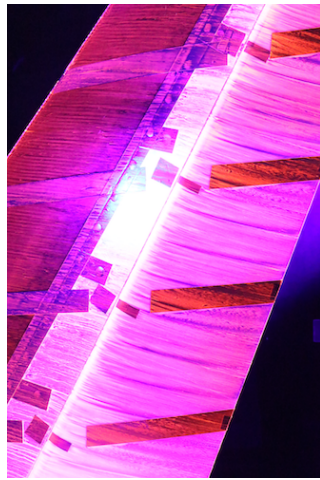
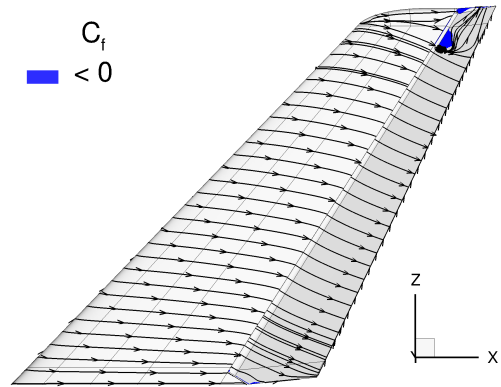


Fig. 3.14 Sections of pressure coefficient distribution, 3D VTP, comparison with wind tunnel results provided by TU-BS [85], $\beta = 0^\circ$, for one mass flow coefficient C_{m_i} , discrete slots

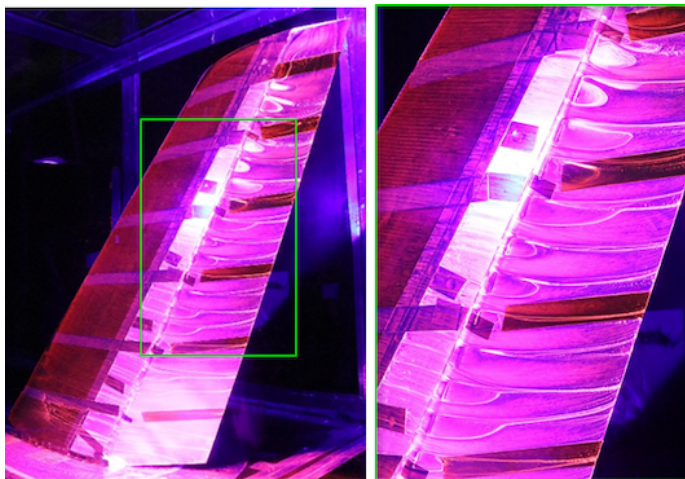


(a) WTT, zoom on the rudder mid-span segment, oil flow visualization from [88]

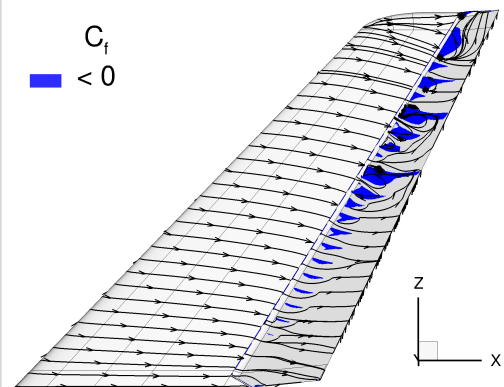


(b) CFD, skin friction lines

Fig. 3.15 Side view of the vertical tail with comparison between wind tunnel test (WTT) and CFD, continuous slot configuration, $\beta = 0^\circ$, $C_m = 3.15 \cdot 10^{-3}$



(a) WTT, zoom on the rudder on the right, oil flow visualization from [88]



(b) CFD, skin friction lines

Fig. 3.16 Side view of the vertical tail with comparison between wind tunnel test (WTT) and CFD, discrete slots configuration, $\beta = 0^\circ$, $C_m = 0.81 \cdot 10^{-3}$

from the initial 2D investigation due to a lack in experimental data to compare with. Here just the resemblance of similar cases with a similar application could be used as an indication. For the 3D vertical tail in the end some experimental data is available which is used for a comparison with the numerical results.

This comparison with the experimental data shows that the numerical setup used is capable to capture the flow characteristics as well as all relevant effects correctly in the linear region, with and without blowing activated. The same trends are obtained, not only for the continuous blowing slot but also for the discrete slots. Even though there is some deviation between wind tunnel test and CFD results in the absolute C_S values for a few combinations of slot configuration and mass flow, the overall agreement is quite good. This shows that the use of CFD with the developed mesh setup, the selected parameter settings including the selected SARC turbulence model and the proposed simulation process is a suitable way to design the tangential blowing slots.

4 Studies of Mechanisms and Effects of Tangential Blowing on a Vertical Tail

In this chapter the mechanisms and effects of tangential blowing on a vertical tail geometry are studied supporting the design of a tangential blowing slot. The location of the slot was selected from a multidisciplinary point of view at the end of the fin as described in Sec. 1.2. Developed around a common baseline geometry, flow calculations with varying complexity were performed. Compared to a wing, 3D effects are stronger on a loaded VTP due to its low aspect ratio and high sweep angle. With the rudder deflected, this three-dimensionality of the flow increases for the same loading. This is further amplified due to partial flow separations at large rudder deflections as investigated in this work. At high loading, the VTP tip and rudder root vortex become stronger and thus also have a wider-ranging impact on the overall flow around the VTP with its low aspect ratio. For the examination of effects like small geometric changes this would complicate the interpretation of the results quite a lot. To allow a separate analysis of the different contributing factors, the 3D effects are disregarded for some investigations allowing a better identification of the design change impact itself. The geometric complexity is then increased from the 2D geometry to a 2.5D geometry. This allows to investigate the influence of the sweep and of effects in spanwise direction like a variation of the slot length. The result of this study is then used as a basis for the 3D investigations with the highest complexity in terms of geometry and flow topology.

4.1 Investigations Based on a Vertical Tail Section

Two-dimensional investigations based on a vertical tail section serve as a starting point for the development of the tangential blowing slot. The airfoil used is a section taken from the 3D VTP with deflected rudder. It is extracted at 50% of the span and depicted in Fig. 2.2. The Reynolds number is $2.24 \cdot 10^6$ based on the extracted airfoil's chord length at a Mach number of 0.2 or a flow velocity of 69 m/s.

In a first step, the momentum coefficient c_{μ} is increased gradually to assess the effect of the blowing. The sideslip angle is also varied. In a next step geometric variations are carried out like changing the slot height and examining the effect of geometric details in the vicinity of the slot. In addition, the effect of pulsed blowing is investigated.

4.1.1 Variation of the Blowing Momentum Coefficient

Without blowing the flow over the rudder is separated already at zero sideslip angle which is used for the blowing momentum variation investigation presented here. This is visualized in Fig. 4.1(a). Activating constant blowing and increasing the momentum coefficient by increasing the jet velocity pushes the onset of the flow separation on the rudder towards the trailing edge. This leads to a higher rudder suction peak, i.e. increased negative pressure coefficients, and to a higher fin leading edge suction peak as depicted in Fig. 4.1(b), Fig. 4.1(c) and Fig. 4.1(d).

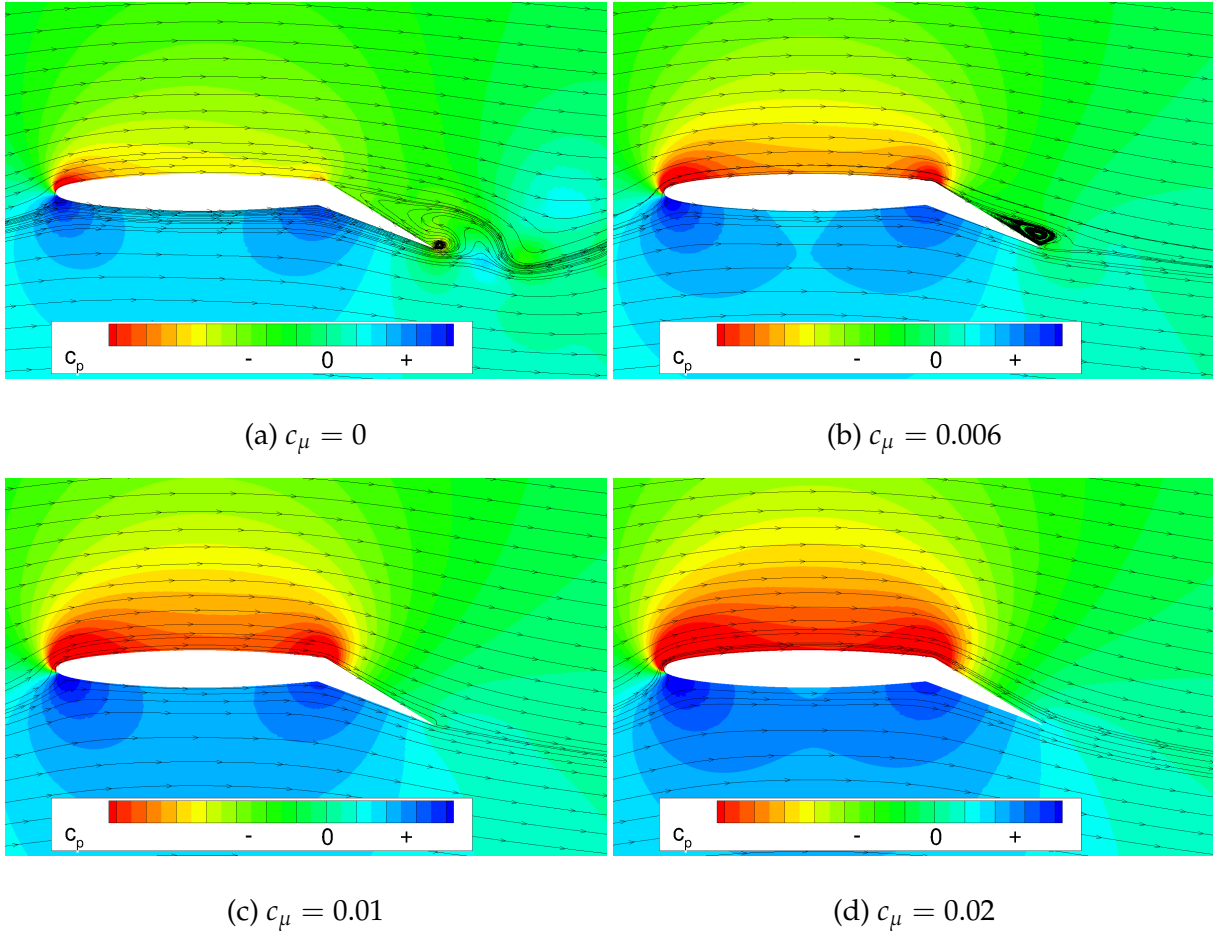


Fig. 4.1 Flow field showing the field pressure coefficient distribution including streamlines.

In Fig. 4.2 the side force and drag coefficients are depicted versus the momentum coefficient. The values of the side force and drag coefficient are given as increments referenced to the value resulting from the flow calculation without blowing. A positive side force increment represents an increase compared to the reference value. A negative Δc_D stands for a reduction of the drag coefficient. The force coefficients are obtained by integration of surface pressure and skin friction excluding the jet boundary plane.

In general, the side force coefficient increases with increasing momentum coefficient. Without blowing activated, the flow is fully separated over the rudder. The larger c_μ and the jet velocity, the longer the flow is able to sustain the adverse pressure gradient on the rudder. This improves the attachment of the flow there, leading to an increase

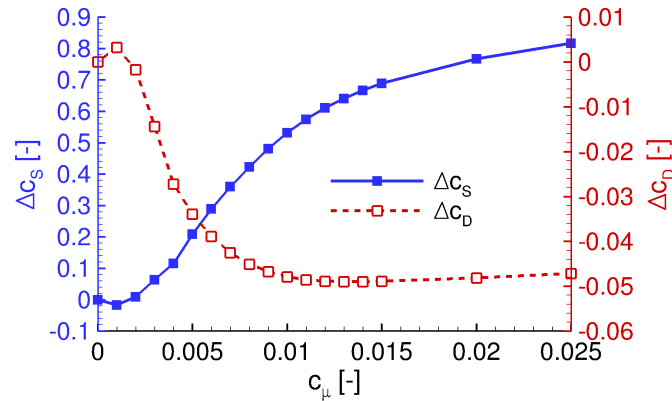


Fig. 4.2 Side force and drag coefficient increment over a variation of the momentum coefficient.

in side force. At $c_\mu = 0.01$ only a very small separation near the rudder trailing edge remains and at $c_\mu = 0.014$ the flow on the rudder is fully attached. At $c_\mu = 0.02$ the jet velocity is higher than needed for complete flow attachment. Between momentum coefficients of 0.01 and 0.015 the efficiency of the active flow control reduces, leading to a reduced increment in c_s for a constant increment in the momentum coefficient. The c_μ -range beyond fully attached flow is called circulation control, the range below is called separation or boundary layer control. This is a typical behavior of circulation control applications [24, 25].

The drag coefficient in general decreases with increasing momentum coefficient since the separation on the rudder is reduced. This leads to a reduction in pressure drag. After the flow on the rudder is fully attached, the drag coefficient increases slightly for very large momentum coefficients. This increase is due to the friction drag which gradually increases with increasing c_μ or jet velocity when the velocity differential and thus friction between the jet and the surface is increased.

For a very small $c_\mu = 0.001$ the effects described above are reversed leading to a decrease in c_s and an increase in c_D compared to the case without blowing. This occurs since the momentum of the jet is smaller than the momentum of the surrounding flow even before the now slightly upstream-moved separation point leading to a detrimental effect on the flow.

4.1.2 Variation of the Sideslip Angle

The sideslip angle is varied for two momentum coefficients: without blowing, i.e. $c_\mu = 0$, and for $c_\mu = 0.01$. With increasing sideslip angle β the side force coefficient c_s increases with and without tangential blowing as illustrated in Fig. 4.3. The curve of the results with blowing activated is shifted towards higher side force values compared to the one without blowing. This is due to the reduction of the separation on the rudder which in turn leads to an increase in c_s . However, the sideslip angle at which the maximum side force coefficient is obtained is lower for the case with blowing. These findings coincide quite well with the results of other experimental and numerical investigations using tangential blowing near a flap leading edge [24, 89]. In the investigation presented here, an airfoil leading edge stall occurs which is responsible for the side force breakdown. If the side force coefficient needs to be increased further, improvements to extend the

usable range of sideslip angles need to be introduced in addition, like for example leading edge blowing. Since the offset between the curves of the two different blowing momentum coefficients is approximately constant in the linear range, the exact sideslip angle used for the following investigation does not play a significant role and a sideslip angle of 0° is selected.

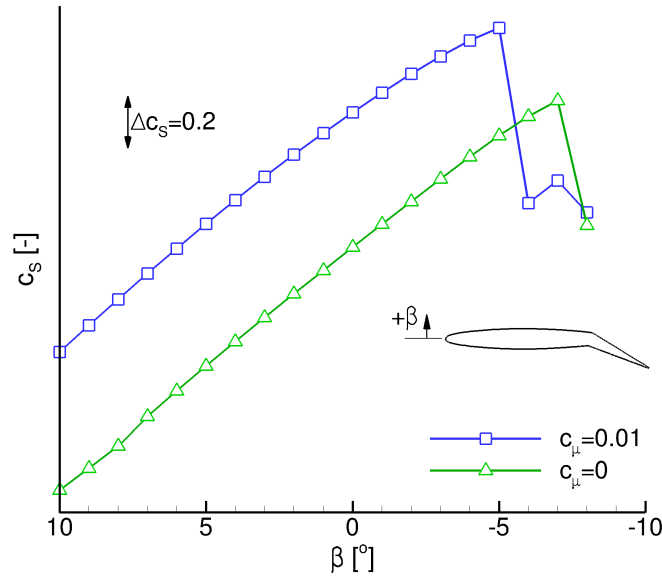


Fig. 4.3 Change in side force coefficient vs. sideslip angle with and without blowing.

4.1.3 Variation of the Slot Height

The slot height has an effect on the side force coefficient which can be reached at a constant momentum coefficient [90]. In a recent circulation control application with a deflected plain flap of a high wing aircraft a dimensionless slot height of $h_{\text{slot}}/c = 0.0006$ was used with good results in terms of efficiency of the flow control system [91]. It was therefore selected as starting point for the work here, complemented by a halved slot height with $h_{\text{slot}}/c = 0.0003$ and a doubled one with $h_{\text{slot}}/c = 0.0012$. Results for this variation are shown in Fig. 4.4. They reveal that for momentum coefficients between 0.01 and 0.014, where the flow is mostly or fully attached, the reference slot height leads to the largest increase in the side force coefficient for the same c_μ . The definition of the momentum coefficient (see Eq. (1.1)) includes apart from the jet velocity also the slot exit area. This means that for a smaller slot height and therefore smaller slot exit area the jet velocity has to be increased to obtain the same c_μ . The opposite is true for the increased slot height where the jet velocity needs to be decreased for the same c_μ .

Even though the reference slot height leads to the largest increase in side force at $c_\mu = 0.01$, halving the slot thickness has a different influence on the magnitude of the side force increment than doubling the slot thickness. For the smaller slot height the results are close to those of the reference slot height, while the reduction of Δc_s is much larger for the case with doubled slot height. One difference between the three cases is the ratio of jet to freestream velocity, which is approximately 3 for the reference slot height. For the smaller slot height, where Δc_s is very close to the one from the reference slot

height, the velocity ratio is even higher. This means that for the cases investigated here and at constant c_μ about the same Δc_s results for velocity ratios above 3. For the larger slot height the jet velocity is reduced for the same c_μ since the jet exit area is increased. This leads to a reduction of the velocity ratio as well which is now only around 2. This reduction in the velocity ratio between jet and outer flow seems to be significant, leading to a noticeable reduction of the side force coefficient increment. For both smaller and larger slot height a small increase in the drag coefficient can be observed. For larger c_μ and larger slot height with the corresponding reduced jet velocity, c_D reduces slightly since the skin friction coefficient is reduced.

The mass flow coefficient for the three different slot heights is depicted in Fig. 4.5. For a prescribed side force coefficient the mass flow coefficient or mass flow rate can be reduced for the smaller slot height. This makes the smaller slot height advantageous. For the larger slot height this is reversed making it less favorable. However, a disadvantage of the smaller slot height could be that it leads to an increase of pressure in the plenum. This might require a stronger structure to avoid a change in the slot geometry when blowing is active. Therefore, for the subsequent studies it was decided to proceed with the reference slot height of $h_{\text{slot}}/c = 0.0006$.

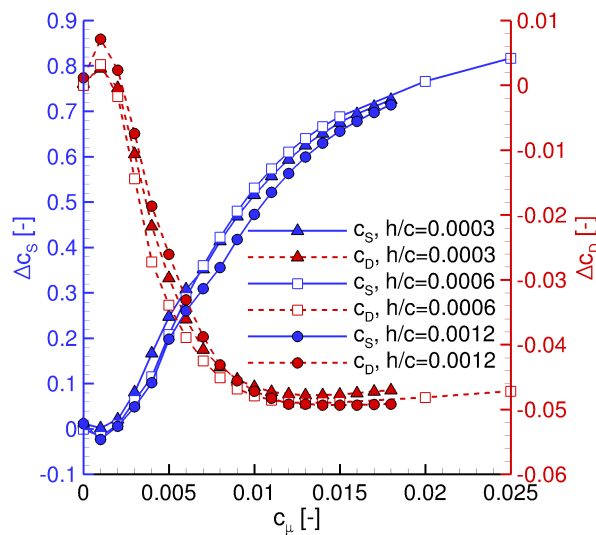


Fig. 4.4 Side force and drag coefficient increment vs. momentum coefficient for three different slot heights

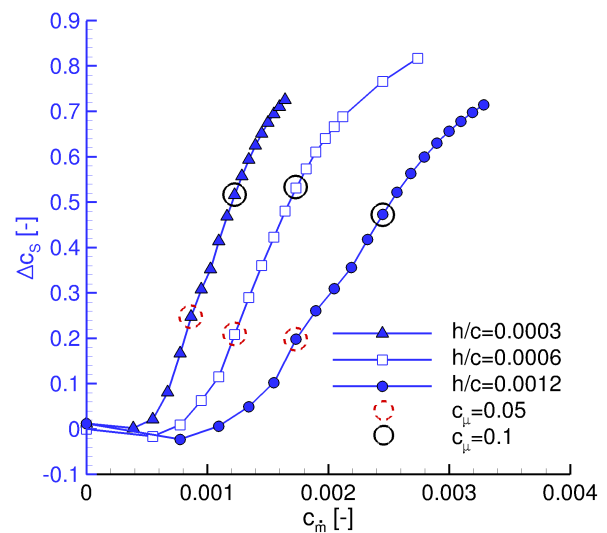


Fig. 4.5 Side force coefficient increment vs. mass flow coefficient for three different slot heights

4.1.4 Effect of the Step Behind the Slot

In this section the two geometries depicted in Fig. 4.6 are investigated. An idea to improve the efficiency of the tangential blowing was to make the rudder slightly thinner so that the jet does not directly blow against the rudder surface. It is assumed that the slot cannot be directly attached to the rudder for integration in a series-production VTP. This would allow manufacturing the rudder unchanged versus a conventional rudder where the rudder shoulder is just a curved piece of sheet metal. It extends only a small distance into the fin, i.e. the rudder leading edge is not closed. Therefore the upper as well as the lower slot wall need to be integrated into the fin. The lower slot wall

would need to have a certain thickness to be stiff enough to keep its shape even at a high pressure in the slot. This inside wall thickness will cause a step from the slot to the rudder shoulder. In many investigations (e.g. [24, 12, 92]) no such step exists in the numerical or experimental setup. The influence of including such a step is investigated here.



Fig. 4.6 Geometry in the vicinity of the slot with and without step

Mach Number Distribution

In Fig. 4.7 the Mach number distribution in the vicinity of the slot is visualized together with velocity profiles. For the configuration with step in Fig. 4.7(a) a recirculation area below the slot exists. It is closed by the corner geometry of the step on one side and by the jet on the upper side. This recirculation area with reversed flow decelerates the jet before it impinges on the rudder shoulder. This is not the case for the geometry where this step does not exist. The Mach number is larger further downstream of the slot exit and therefore improves the attachment of the flow on the rudder to a higher degree.

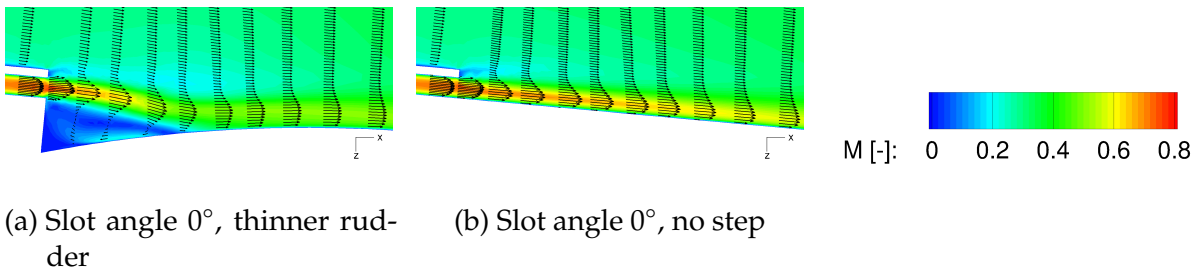


Fig. 4.7 Variation of the Mach number in the vicinity of the slot for the geometry with and without step at $c_{\mu} = 0.01$

Side Force and Drag Increments

The effects observed in the Mach number distribution contribute in summary to a beneficial effect when no step is present. With blowing activated at $c_{\mu} = 0.01$ the side force coefficient is increased by about 4.4% and the drag coefficient is decreased by 11.5% for the configuration without step.

4.1.5 Effect of the Rudder Thickness Behind the Slot

For the previous investigations in Sec. 4.1.4 the geometry of the rudder was made thinner as shown in Fig. 4.8(a). The intention was to allow the jet to pass the rudder shoulder

in a tangential way and not to blow directly onto it. In reality, this would require a modification of the rudder or the fin compared to a non-AFC enhanced vertical tail. The resulting additional step from the fin to the rudder would be present during cruise flight as well and might not be desirable. Therefore, the geometry with the original thickness rudder shown in Fig. 4.8(b) is investigated as well.



Fig. 4.8 Geometry in the vicinity of the slot with thinner and original rudder

Mach Number Distribution

In Fig. 4.9 the Mach number distribution in the vicinity of the slot is visualized together with velocity profiles for the thinner and the original rudder. Obvious is the much larger area of reduced velocity in the corner of the step in Fig. 4.9(a) for the thinner rudder compared to Fig. 4.9(b) with the original-thickness rudder. Since the rudder was made thinner also the step height from the rudder shoulder to the slot is increased as shown in Fig. 4.9(a). This leads to this relatively large area of reversed and low-velocity flow which is not only extended in height but also in length in flow direction. This larger area of low-energy flow also leads to an increased exchange and transfer of energy from the high-energy jet to this recirculation area.

The idea behind making the rudder thinner was that the jet could pass the rudder shoulder tangentially. It should not be decelerated by blowing directly onto the surface. However, as Fig. 4.9(a) reveals, the jet does not travel straight after leaving the slot. It is sucked towards the rudder surface by the recirculation area with its relatively low pressure. Therefore, the initial idea does not work and is not of any benefit here. Due to this, the geometry with the same slot angle of 0° but original rudder thickness (cf. Fig. 4.9(b)) and thus smaller step height leads to an increased jet velocity further downstream on the rudder in comparison.

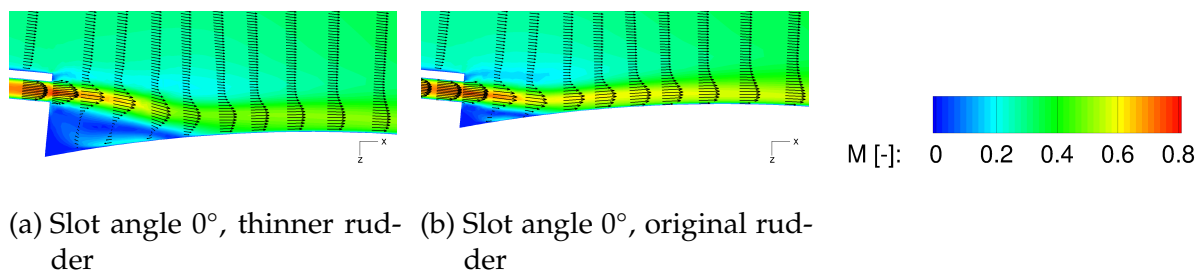


Fig. 4.9 Variation of the Mach number in the vicinity of the slot for the geometry with thinner and original rudder at $c_\mu = 0.01$

Side Force and Drag Increments

Similar as for the configuration without step (cp. Sec. 4.1.4) the original rudder geometry leads to an increased side force and decreased drag coefficient compared to the configuration with the thinner rudder. However, the gain in side force is only about half of the value obtained by removing the step in the geometry. Comparing to the thinner rudder geometry the side force coefficient increases by 2.8% and the drag coefficient decreases by 6.9%.

4.1.6 Effect of Slot Angle Variation

For the geometry with the original rudder the influence of a variation of the slot angle is investigated. The slot angle is defined as shown in Fig. 4.10. The different geometries are given in Fig. 4.11. The slot geometries presented in the previous sections were parallel to the fin surface, corresponding to a slot angle of 0° .

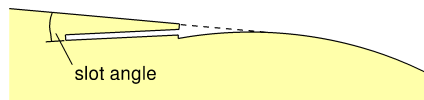


Fig. 4.10 Definition of the slot angle

For the slots with an angle to the fin surface the slot is constructed in such a way that the lower slot surface or its extension meets the rudder shoulder in a tangential way. Due to this, the size of the fin trailing edge thickness above the slot and the step below the slot change. The overall height of step plus fin trailing edge is constant for all geometries. The slot angle is increased from 0° as shown in Fig. 4.8(b) in the previous section to 4° and 8° . When increasing the angle to 15.6° the step below the slot vanishes. For an even larger slot angle of 24° the slot is connected tangentially to the rudder shoulder inside the fin and needs to be extended by adding a curved part to the slot up to the end of the fin. By doing this the slot height can be kept constant. For the geometry with a slot angle of 8° the slot angle is increased by another 6° as shown in Fig. 4.11(c) by rotating the slot around the slot exit lower point to examine the effect of a deviation from the tangential design approach.

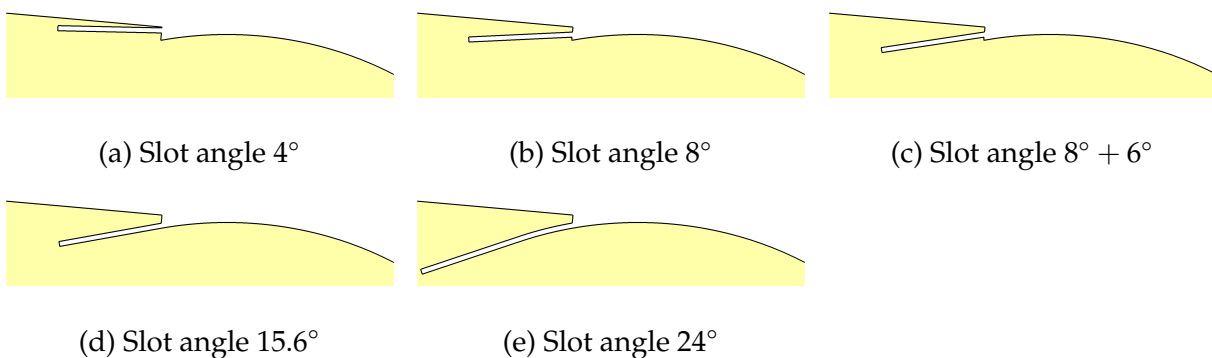


Fig. 4.11 Geometry in the vicinity of the slot with different slot angles and geometries

Mach Number Distribution

For the different geometries with varying slot angle the Mach number distribution in the vicinity of the slot is visualized together with velocity profiles in Fig. 4.12. Due to the varying position of the slot exit in z -direction in principle one main difference can be observed. Fig. 4.12(a) to Fig. 4.12(c) show geometries with a fin trailing edge and a step below the slot. In contrast to this, the geometries with a slot angle of 15.6° and 24° shown in Fig. 4.12(d) and Fig. 4.12(e) have no step below the slot. Since there is no step in these cases, no recirculation area exists below the slot. In addition, the jet is not decelerated before it impinges on the rudder shoulder since it remains attached to the surface after leaving the slot. However, above the slot the fin trailing edge has thickened, leading to an enlarged recirculation area there. This entails losses compared to the geometry without the step, see Fig. 4.7(b), which has only a very small fin trailing edge thickness.

The geometry with a slot angle of 4° in Fig. 4.12(a) has a comparatively thin fin trailing edge which might be too small for manufacturing and structural strength requirements. But from an aerodynamic point of view this thin fin trailing edge leads to a considerable reduction in the size of the recirculation area behind it. On the other hand, the step towards the rudder shoulder is increased compared to the geometry with 8° slot angle as shown in Fig. 4.12(b).

Apart from the size of the recirculation areas, which are dependent on the thickness of the fin trailing edge and the height of the step, a change in the direction of the jet can be observed. This redirection does only take place if there is a low pressure recirculation area below the jet (Fig. 4.12(a) to Fig. 4.12(c)) since the jet cannot remain attached to the rudder surface at the slot exit.

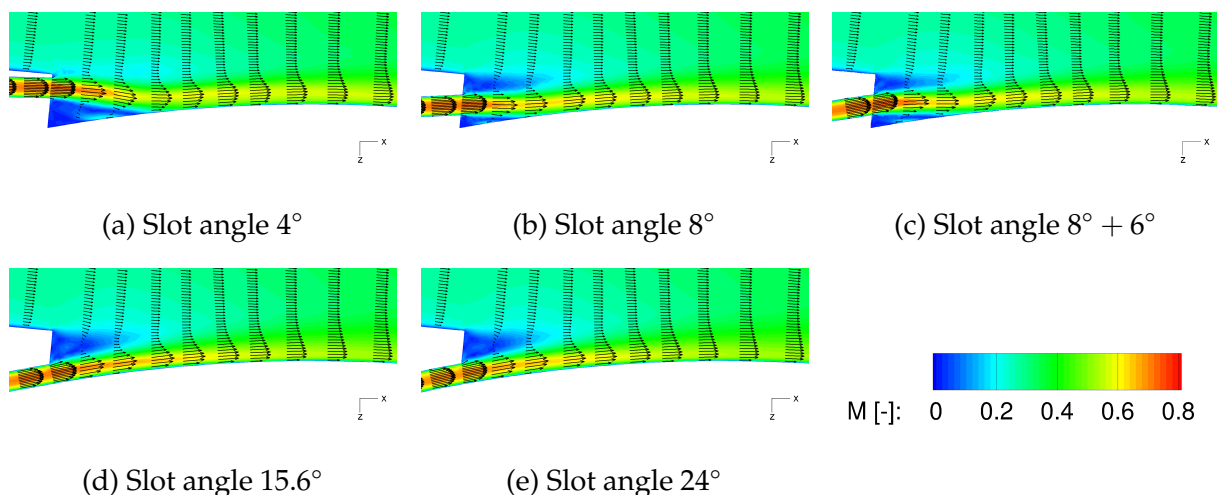


Fig. 4.12 Variation of the Mach number in the vicinity of the slot for different slot angles and geometries.

Velocity Profiles

A direct comparison of the velocity profiles is shown in Fig. 4.14. In Fig. 4.13 the location of the profiles is given exemplarily for the 0° slot. The position of the maximum velocity in each velocity profile varies for the first velocity profiles depending on the position of the slot at the fin trailing edge. For comparison also the result for the 0° slot angle with the original rudder is included.

The largest differences can be found for the velocity profiles close to the slot. Here the maximum as well as the minimum velocity above and below the slot differ at the locations where the recirculation area with reduced velocity can be found. The velocity profiles further away from the slot become more and more similar. They have all in common that the jet increases the velocity near the surface to a value larger than that of the outer flow leading to a bulge in the velocity profile. They have a fuller velocity profile and are therefore more resistant to separation. In contrast to the other calculation results the velocity profiles for the results with 0° and 4° slot angle still have a positive velocity above the slot. For these cases, the fin trailing edge has a smaller height there leading to the reduced size of the recirculation area.

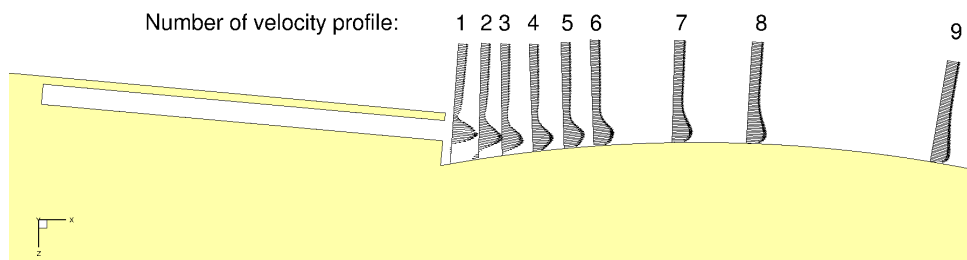


Fig. 4.13 Geometry in the vicinity of the slot showing the location of the velocity profiles

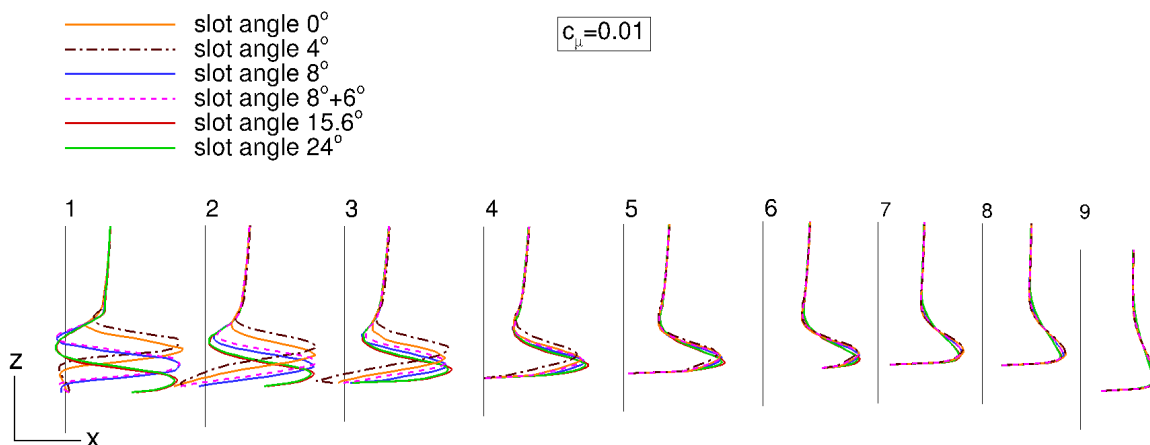


Fig. 4.14 Comparison of velocity profiles at $c_\mu = 0.01$ in x -direction for a variation of the slot angle. The vertical line marks zero velocity for the adjacent profile.

Side Force and Drag Increments

In Fig. 4.15 the side force and drag increments for the different slot angle calculations are presented for c_μ -values of 0, 0.01 and 0.02. The results are compared to those obtained

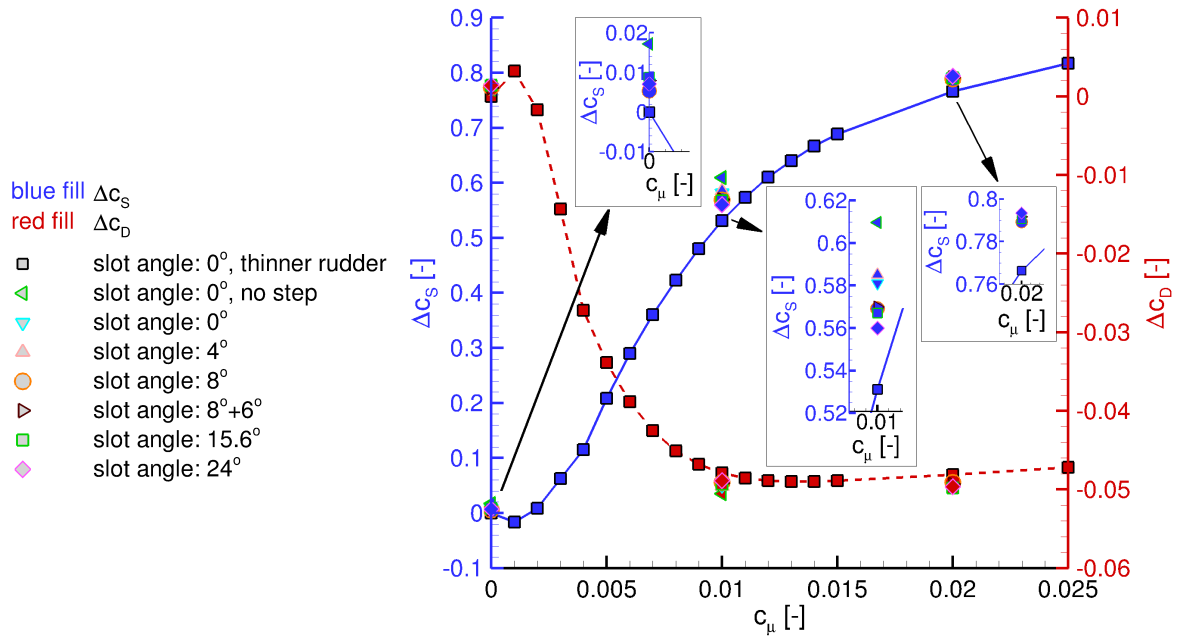


Fig. 4.15 Comparison of side force and drag coefficient increments versus momentum coefficient for different slot geometries and slot angles.

with the thinner rudder as reference which is represented by a curve. Additionally included are the results for the geometry without step and those for the geometry with the original rudder and a slot angle of 0° .

It is obvious that all configurations with the original rudder have an increased side force and decreased drag coefficient compared to the result of the thinner rudder with a slot angle of 0° . The reason for this was explained before with the detrimental effect caused by the increased step height compared to the other configurations. The largest side force increase results from the geometry without step. These data points were discussed in Sec. 4.1.4 and are given here just as a reference. All other results for the slot angle variation with the original rudder thickness are quite close together. The velocity profiles downstream of the rudder shoulder are also quite similar. To allow a better differentiation between the results a zoom view is included for c_s .

The largest deviation in the results can be found for a momentum coefficient of 0.01. Without blowing the separation is very similar for all cases since the overall step height from fin to rudder shoulder is the most influencing parameter. For $c_\mu = 0.02$ the jet velocity is larger than needed for complete flow attachment and due to the large addition of momentum to the flow small changes in the slot angle have only a minor effect.

The increase in Δc_s which can be achieved for a momentum coefficient of 0.01 by slot angle modifications is between 1.6% and 3% compared to the reference configuration with thinner rudder. The largest increase in c_s is obtained for the 4° slot angle closely followed by the 0° slot angle geometry. This agrees with the findings derived from the discussion of the velocity profiles above where these two configurations have the largest jet peak velocity downstream of the rudder shoulder, even if the advantage is only marginally visible there. The lowest increase in the side force coefficient for $c_\mu = 0.01$ results from the case with the largest slot angle of 24° . At $c_\mu = 0.01$, the drag coefficient is reduced by 4.3% to 7.5% for the different geometries compared to the reference geometry.

The slot angle of 15.6° is very similar to the angle of $8^\circ + 6^\circ = 14^\circ$ which is a special case since it has a non-tangential slot direction (cf. discussion on page 48). Not only the angle but also the results for these two geometries are quite similar as well. Also for the 8° slot angle the results are quite close, but here the slot angle is nearly halved. The fact that only minor differences result although the slot angle was varied quite a bit shows that the exact angle of the slot is not that critical. The slot does not need to be exactly tangential to the rudder shoulder and also small variations in the slot angle due to manufacturing accuracy should have no significant impact on the performance of the VTP with AFC activated. More important seems to be the size of the recirculation areas and their effect on the jet.

Pressure Coefficient Distribution

In Fig. 4.16 exemplarily three C_p -distributions are shown for $c_\mu = 0.01$. The result for the slot angle of 15.6° is compared with those of the geometry with a slot angle of 0° and thinner rudder, which gave the smallest increase in c_S , and with the geometry with a slot angle of 0° without step, which gave the largest increase in c_S .

The curves for the 15.6° slot angle geometry and for the 0° slot angle geometry with thinner rudder are in principle quite similar. The zoom shows that with a slot angle of 15.6° the rudder hinge line pressure peak is slightly higher. This leads to a somewhat better pressure recovery at the trailing edge. Since in subsonic flow pressure information does not only travel downstream but also upstream this has also an effect on the fin. The increased circulation shifts the stagnation point at the leading edge further to the pressure side, thus also increasing the suction peak at the fin leading edge. This explains the slight overall increase in the side force coefficient for the 15.6° slot angle geometry. Making the comparison to the results of the geometry without step and 0° slot angle shows a similar rudder shoulder pressure peak as for the 15.6° angled slot but an even better pressure recovery at the trailing edge and a larger upstream effect leading to an increased leading edge suction peak agreeing with the slight increase in the side force coefficient.

4.1.7 Effect of Pulsed Blowing

In addition to the constant blowing jet used so far, a pulsed blowing jet is examined as well. For this, unsteady flow calculations are required which need significantly more computational resources. A top-hat or so-called square-shape function is used for the pulsed blowing actuation signal. With pulsed blowing the jet is switched off half the time of one actuation period in the scope of this work in order to reduce the required mass flow. Different investigations, e.g. for a symmetric NACA 0015 airfoil with deflected flap [93] at comparable Reynolds numbers, have shown that this can increase the blowing efficiency since about the same side force coefficient increment can be obtained with less mass flow. It is investigated here if the same is also true with the geometry used in this work and with tangential blowing instead of blowing at an angle to the surface.

During one actuation period spanwise vortices are created due to the pulsed blowing. This is shown in Fig. 4.17 for a dimensionless frequency $F^+ = 0.3$ and a momentum coefficient $c_\mu = 0.04$. The first snapshot "A" shows the field pressure coefficient

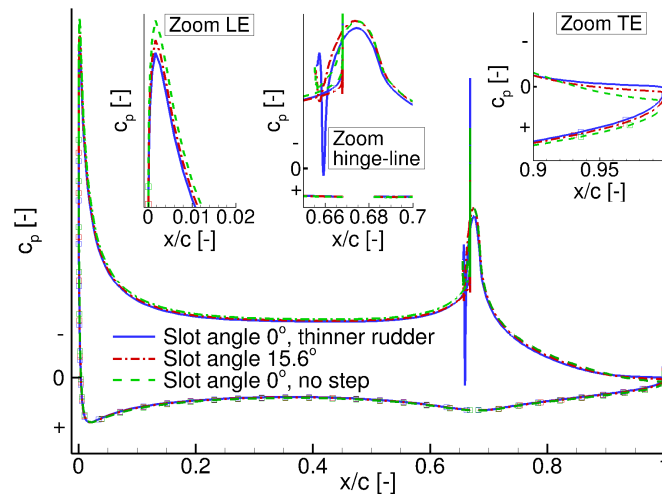


Fig. 4.16 Comparison of the pressure coefficient distribution at $c_{\mu} = 0.01$ for the geometry with slot angle 0° and thinner rudder, slot angle 15.6° and slot angle 0° without step. The pressure distribution of the deflected rudder is rotated back to where it would be for the undeflected case.

distribution and streamlines a short time after blowing was activated. Without blowing large parts of the flow over the rudder are separated. The jet pushes against this recirculation area and squeezes it in flow direction while moving it downstream so that it gets a bit larger perpendicular to the rudder surface. This is depicted in the following snapshots “B” and “C”. In snapshot “D” the vortex is already close to the trailing edge. Now the blowing is switched off. The vortex then leaves the airfoil behind and moves further downstream. Upstream on the rudder a new separation region has started to grow close to the rudder shoulder which gets larger during the non-blowing period and becomes clearly visible in snapshot “F”. At the end of the non-blowing period the separation is again quite large on the rudder but close to the trailing edge a region with attached flow still exists.

Two variations using pulsed blowing are presented here: A variation of the momentum coefficient at a fixed actuation frequency, which is divided into several subsections, and eventually a variation of the dimensionless frequency F^+ for a fixed c_{μ} . Some of the results were already presented in [94].

Variation of the Momentum Coefficient at Two Fixed Dimensionless Frequencies

Constant Blowing: Steady and Unsteady RANS Results

For the constant blowing results presented before, steady RANS computations were carried out. Fig. 4.18 shows that the results using steady versus unsteady RANS simulations differ at low momentum coefficients. The force coefficient depicted for the URANS result is the value averaged over one actuation cycle. Since the separation on the rudder is quite large at very low c_{μ} , using steady RANS simulations does not seem to lead to the correct result due to the unsteadiness of the problem. For c_{μ} larger than 0.004 with gradually reducing separation areas on the rudder the results coincide very well with the URANS results. This means that the RANS results for very low momentum coefficients have to be treated with care regarding the absolute values for side force and

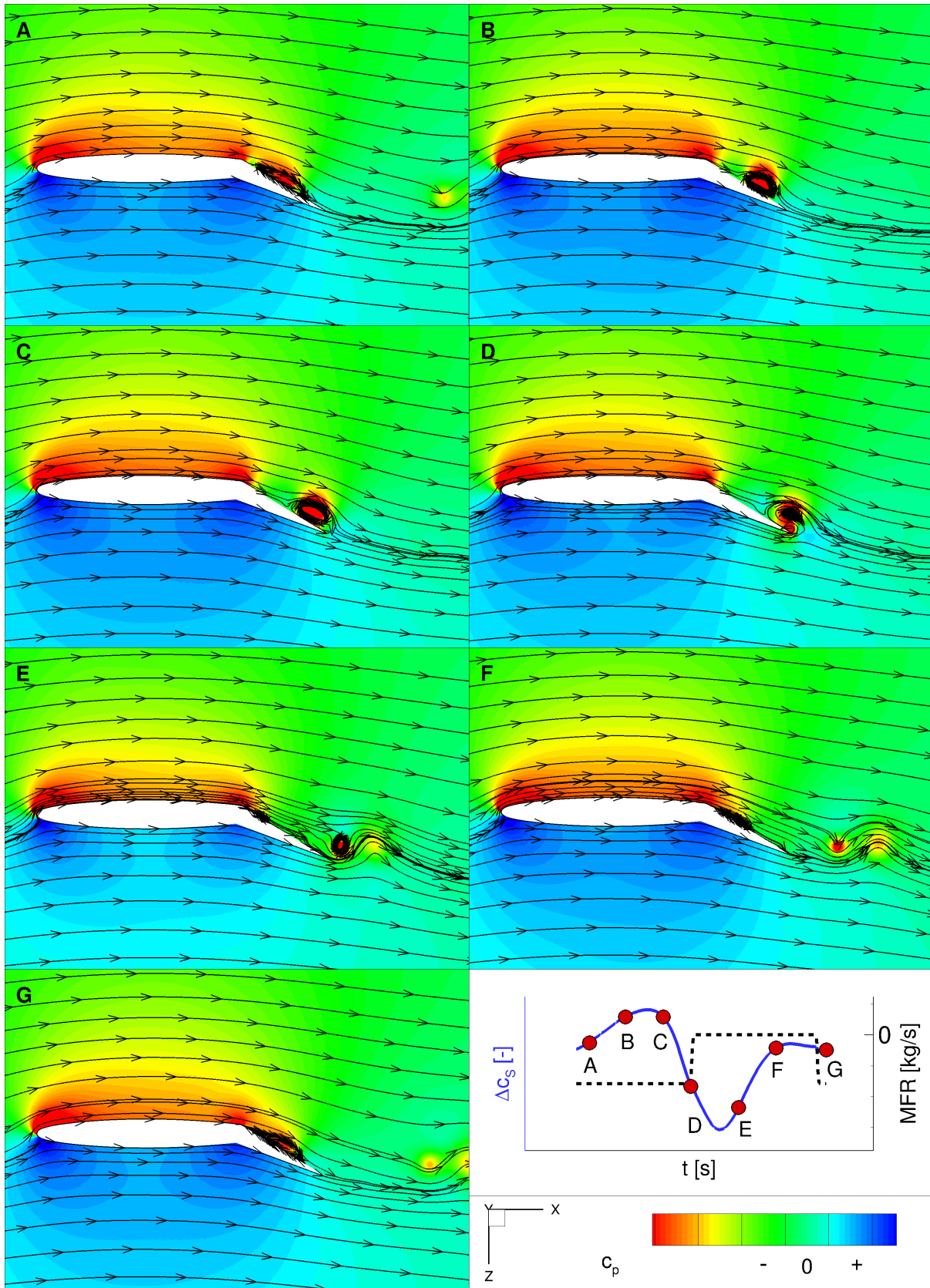


Fig. 4.17 Flow field showing the field pressure coefficient distribution and streamlines for various snapshots over one actuation period, pulsed blowing, $F^+ = 0.3$, $c_\mu = 0.004$

drag increments. However, the curve progression stays in general the same. In order to make an appropriate and consistent comparison to the pulsed blowing jet results, which can only be calculated using the unsteady approach, the constant blowing cases also need to be calculated using the URANS equations — at the expense of a highly increased calculation time.

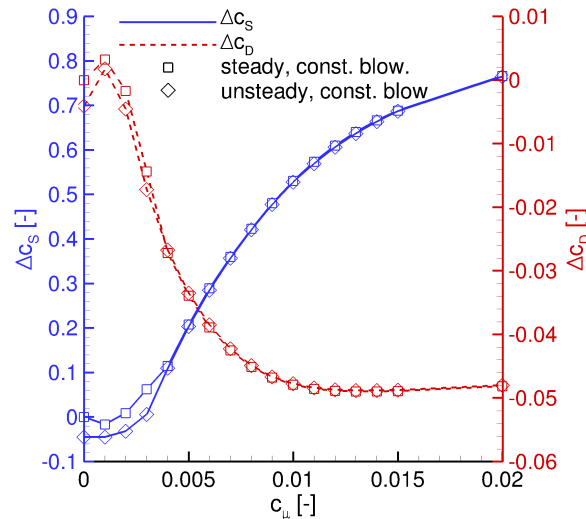
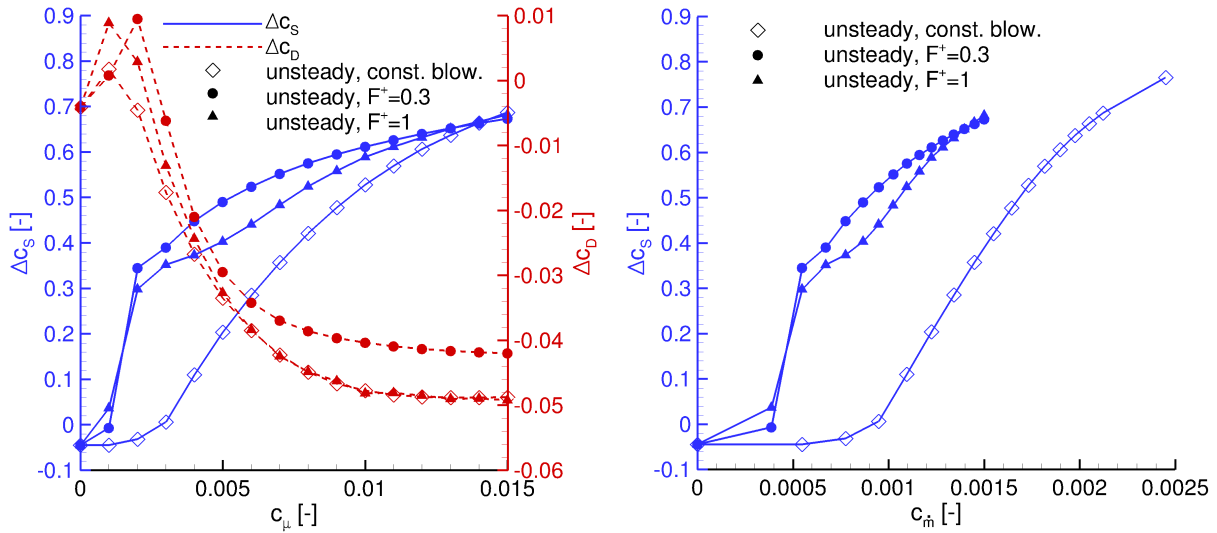


Fig. 4.18 Side force and drag coefficient increment shown versus a variation of the momentum coefficient comparing results for constant blowing obtained with steady and unsteady simulations.

Comparison of Constant and Pulsed Blowing Results

In a next step a variation of the frequency for the pulsed blowing is performed. Two different dimensionless frequencies are compared to the results with a constant blowing jet. For these calculations the momentum coefficient is kept constant between both blowing types. Since for the pulsed jet a duty cycle of 0.5 is used, the jet is only active half the time. In the formula of the momentum coefficient for pulsed actuation (Eq. (1.2)) the factor DC is added to account for this. After inserting Eq. (1.3) into Eq. (1.2) and cancelling, the factor DC remains in the numerator in comparison to the equation for constant blowing. From this it follows that for the pulsing jet the mass flow rate will be multiplied by a factor of \sqrt{DC} leading with a duty cycle of 50% to a reduction of the mass flow rate by approximately 30%. This reduction of the mass flow rate for the pulsed blowing results can be found as well when looking at Fig. 4.19(b).

Fig. 4.19(a) reveals another interesting outcome of the study. For low momentum coefficients the pulsed blowing calculations show a significant increase in c_s compared to the constant blowing jet results. At $c_\mu = 0.003$ a side force increment can be achieved with pulsed blowing which is only possible with constant blowing using a momentum coefficient which is more than twice as high. However, this large gain in side force in comparison to constant actuation decreases with increasing momentum coefficient. At higher values of c_μ the side force coefficients achieved with pulsed blowing approach those resulting with constant blowing. The curves intersect at that value of the momentum coefficient where for constant blowing the flow is fully attached. After this point the constant blowing leads to higher side force increments. Due to the jet being periodically inactive with pulsed blowing there is always a part of the rudder where the flow is not attached, which is avoided when the jet is blowing all the time. This constant blowing



(a) Side force coefficient increment versus momentum coefficient (b) Side force coefficient increment versus the mass flow coefficient

Fig. 4.19 Comparison of unsteady results for constant blowing with pulsed blowing (averaged over one actuation period) for two dimensionless frequencies

is only beneficial if the jet is strong enough to lead to a fully attached flow on the rudder. Similar observations that small mass flows lead to a larger lift increase with pulsed blowing were reported by Jones in an experimental approach for a circulation control airfoil with rounded trailing edge [28]. This behavior is true for both dimensionless frequencies investigated here. The two curves showing pulsed blowing results have a similar curve progression at a low $F^+ = 0.3$ ($f = 126$ Hz) and one being more than three times larger at $F^+ = 1$ ($f = 420$ Hz). Here the results obtained with $F^+ = 0.3$ lead to the largest side force increments for most values of c_μ . The reason for this will be explained below in a dedicated paragraph about the variation of the dimensionless frequency. The same applies to the drag coefficient, which is for the calculations at $F^+ = 1$ similar to the one for the constant blowing calculations over a large range of c_μ , but larger at $F^+ = 0.3$.

Field Pressure Coefficient Distribution

For a selected $c_\mu = 0.004$ the field pressure coefficient distribution is compared for pulsed and constant blowing results in Fig. 4.20. For pulsed blowing a selected instantaneous snapshot after half of the period ($t = T/2$) is shown for both $F^+ = 1$ and $F^+ = 0.3$ as well as the mean value over one actuation period. For $F^+ = 1$ the frequency is higher meaning that one pulse travels faster over the rudder than for $F^+ = 0.3$, but this also leads to a higher number of jet pulses in total in the same time frame. Therefore, there are more vortices over the rudder for the $F^+ = 1$ case in Fig. 4.20(a) compared to Fig. 4.20(c) with $F^+ = 0.3$. When comparing the mean values over one period with the constant blowing result in Fig. 4.20(e) it is obvious that the constant blowing calculation leads to the largest and pulsed blowing with $F^+ = 0.3$ to the smallest separation area on the rudder. The extent of the separation area and the side force coefficient are closely linked — the smaller the separation area, the larger the side force coefficient. Thus, this agrees with the results shown in Fig. 4.19(a), where the calculation results at $F^+ = 0.3$ lead to the largest

side force increment at $c_\mu = 0.004$ which was selected for the illustrations presented here.

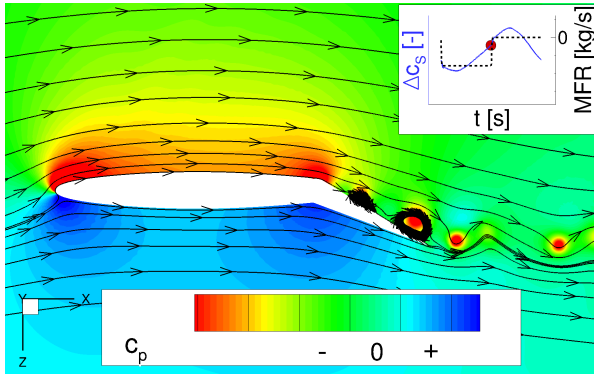
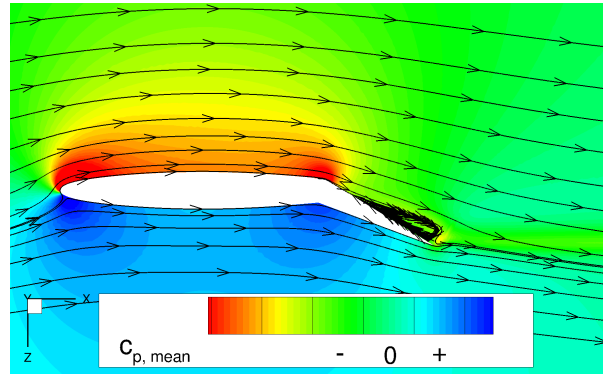
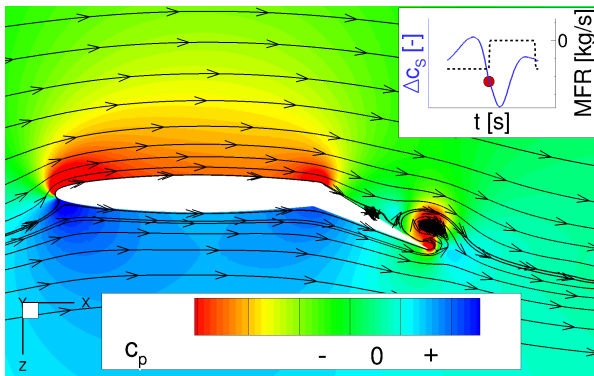
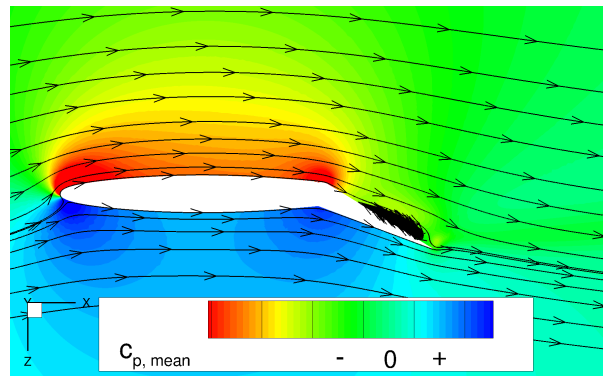
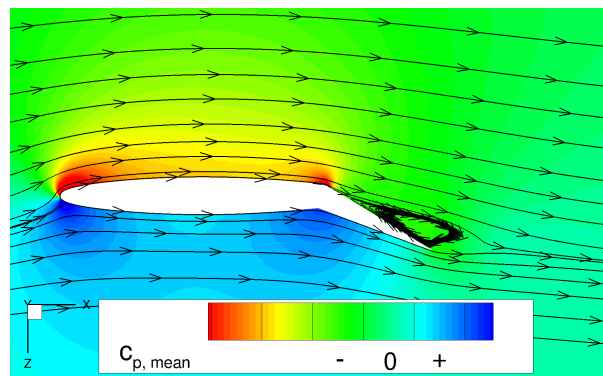
Field Velocity Distribution

An explanation for the comparably high gain in c_s at low momentum coefficients with pulsed blowing can be found in Fig. 4.21. Here for both dimensionless frequencies $F^+ = 1$ and $F^+ = 0.3$ field velocity distributions for an instantaneous snapshot are depicted for two momentum coefficients. At a small value of $c_\mu = 0.002$ a high side force gain compared to constant blowing occurs. For $c_\mu = 0.01$ the side force increment is getting closer to the constant blowing result.

In general, without blowing the flow on the rudder separates just behind the rudder shoulder. If blowing is active the jet introduces energy into the flow close to the rudder surface allowing the boundary layer to better sustain the adverse pressure gradient further downstream on the rudder. The jet also pushes the separated low-energy flow downstream. While this happens, the region of separated flow is first compressed in flow direction, increasing its extent in the direction normal to the rudder surface at the same time. Since the jet with its higher velocity is much faster than the separated flow, it goes over and around the vortex that had developed over the rudder surface. The high velocity at the top of the vortices in Fig. 4.21(a) and Fig. 4.21(c) for the cases with low c_μ can be clearly seen. The rotating motion of the vortex is accelerated, receiving not only energy from the jet itself but also from the outer flow which it reaches due to its large extent perpendicular to the surface. The velocity at the border of the vortex becomes relatively high. At the rudder surface the velocity is directed against the onset flow direction, but the velocity magnitude is the one which is important here. This relatively high velocity creates a lower pressure near the surface leading to increased suction and thus side force for this limited area on the rudder. In the 2D pressure distribution in Fig. 4.22 this can be identified by a bubble or local peak in the distribution.

When looking at the figures for the higher momentum coefficient cases in Fig. 4.21(b) and Fig. 4.21(d) such a high velocity near the rudder surface inside the vortex can not be found. The momentum coefficient is much higher and thus reduces the flow separation to a larger extent but is still not large enough to eliminate the separation completely. It can be noticed that the extent of the vortex perpendicular to the surface is highly reduced. For the higher frequency this is true for the extent in chordwise direction as well. This leads to an increase in the side force coefficient compared to the case at low c_μ . However, since the second effect which draws energy from the outer flow into the boundary layer is not present here as an additional contributor of energy, the gain in side force compared to steady blowing is lower.

The results for constant blowing are shown additionally in Fig. 4.21(e) and Fig. 4.21(f). Here the scale for the side force coefficient in the right upper insert was changed for the smaller c_μ since c_s and its variation are much smaller. The side force is approximately constant due to the constant blowing. The same is true for the size of the separation area. For $c_\mu = 0.002$ in Fig. 4.21(e) it is obvious that no increased velocity near the rudder surface exists. The jet velocity is also smaller compared to the pulsed blowing. Only the mean jet velocity is the same and since the pulsed blowing is only active part of the time it has a higher velocity when blowing is active. For $c_\mu = 0.01$ in Fig. 4.21(f) the area of low velocity seems to be smaller with constant blowing than for the pulsed blowing calculation at $F^+ = 0.3$. This is indeed true for the specific time step shown which is at the end of the actuation period for the pulsed blowing, i.e. with blowing already

(a) Pulsed blowing, $F^+ = 1$, snapshot at $T/2$ (b) Pulsed blowing, $F^+ = 1$, mean values(c) Pulsed blowing, $F^+ = 0.3$, snapshot at $T/2$ (d) Pulsed blowing, $F^+ = 0.3$, mean values

(e) Constant blowing, mean values

Fig. 4.20 Flow field showing the field pressure coefficient distribution and streamlines where constant and pulsed blowing results are compared for $c_{\mu} = 0.004$.

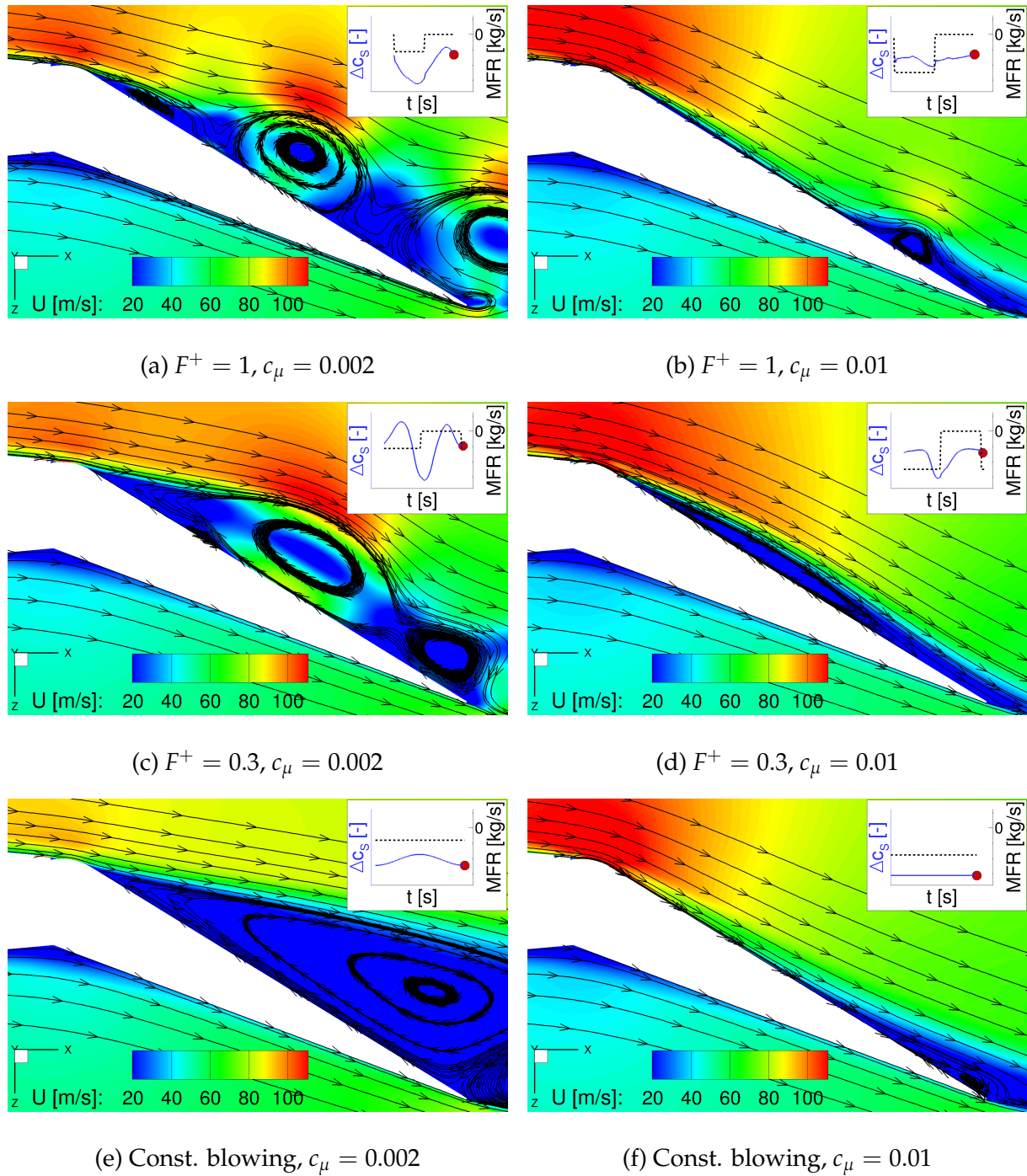


Fig. 4.21 Flow field showing the velocity magnitude distribution and streamlines in the vicinity of the rudder for different pulsed and constant blowing results at instantaneous snapshots.

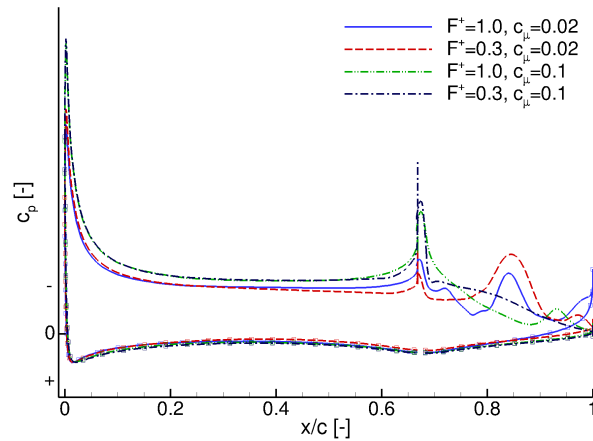


Fig. 4.22 Pressure coefficient distribution of instantaneous snapshots at the end of an actuation period for a variation of the dimensionless frequency and c_{μ} .

inactive for $\Delta t = T/2$. When blowing is activated, at some point in the period the flow is attached on almost the complete rudder. For the mean distribution, this leads to a smaller area of reversed flow than with constant blowing at the same c_{μ} , explaining the higher side force coefficient overall. This again coincides with the findings regarding Δc_S shown in Fig. 4.19(a).

Variation of the Dimensionless Frequency at Two Fixed Momentum Coefficients

In Fig. 4.23 F^+ is varied between 0.1 and 2 corresponding to frequencies between 42 Hz and 840 Hz for two momentum coefficients. Results are presented for a higher $c_{\mu} = 0.01$ and a lower $c_{\mu} = 0.003$. As expected, a higher c_{μ} leads to a larger increase in the side force coefficient. For each c_{μ} a change in the side force and drag coefficient just by varying the dimensionless frequency can be observed. For $c_{\mu} = 0.01$, $F^+ = 0.3$ leads to the highest side force coefficient. For larger F^+ the curve decreases gradually. With increasing F^+ and thus frequency the pulses are shorter but more often during a certain time interval. Here the dependency of the side force coefficient on F^+ is relatively small. This behavior coincides well with other numerical and experimental findings [95]. For the smaller $c_{\mu} = 0.003$ the relatively large separation on the rudder also leads to an increased variation of side force and drag coefficients when changing the frequency. The curve shows a more pronounced peak around $F^+ = 0.6$ with a stronger decrease of the side force coefficient for lower and higher F^+ . Thus, the maximum side force coefficient is not only dependent on the frequency itself but also on the momentum coefficient which is used and the degree of success in reducing the separation.

For the higher value of $c_{\mu} = 0.01$ mean pressure coefficient distributions averaged over one period are presented in Fig. 4.24. With blowing activated not only an increased suction peak at the rudder shoulder and a reduced separation on the whole rudder can be noticed but also an upstream effect with a clearly decreased pressure on the fin suction side and an increased leading edge suction peak. For different F^+ the changes on the fin are quite small and more pronounced on the rudder. Here the rudder shoulder suction peak increases with increasing F^+ and the pressure coefficient tends to be more positive towards the rudder trailing edge showing a better pressure recovery. This agrees with the somewhat reduced c_S for the higher F^+ because the area between upper

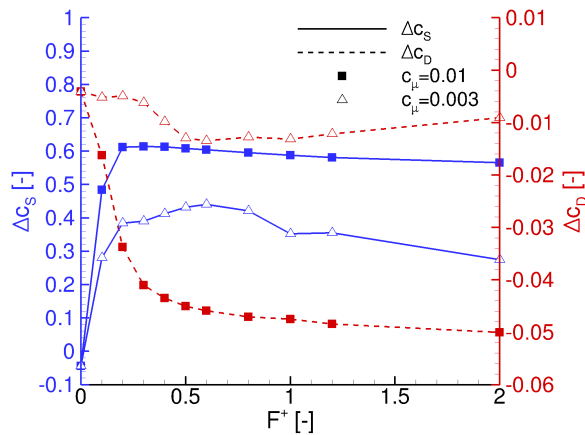


Fig. 4.23 Side force and drag coefficient increment versus a variation of the dimensionless frequency for two momentum coefficients.

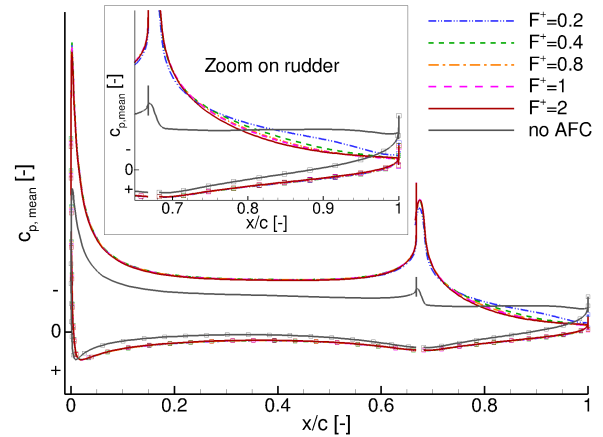


Fig. 4.24 Mean pressure coefficient distribution for $c_\mu = 0.01$ and a variation of the dimensionless frequency.

and lower C_p -curve reduces.

4.1.8 Summary

For these investigations, a 2D section of the 3D vertical tail with deflected rudder is used. The investigations with constant tangential blowing show that the separated flow on the rudder can be fully attached with sufficiently high jet velocity or momentum coefficient c_μ . A dimensionless slot height of $h_{\text{slot}}/c = 0.0006$ leads to the highest increase in the side force coefficient for medium to large c_μ values and is therefore used for the subsequent investigations. Concerning the variation of the geometry in the vicinity of the slot it was shown that the use of the original rudder is beneficial for c_s compared to a rudder thinned by the thickness of the slot at the rudder shoulder. The original thickness rudder geometry will therefore be used for the following investigations. Some changes in the orientation of the slot and its angle to the rudder shoulder were found to have only a minor impact on the side force coefficient. Recirculation areas due to a thick fin trailing edge or a large step below the slot towards the rudder shoulder have a larger impact, reducing the side force gain. The slot orientation approximately parallel to the fin surface is selected for the following investigations (comp. Fig. 4.8(b)). When using a pulsing instead of a constant blowing jet some interesting effects could be observed with a significant increase in c_s for small c_μ or blowing velocities. This will be investigated also in the next section which deals with the 2.5D geometry.

4.2 Investigations on an Infinite Swept Vertical Tail Segment

The 2.5D investigation uses an infinite swept vertical tail segment and is based on the outcome of the 2D study of the tangential blowing slot. Again the section at 50% span of the 3D VTP with deflected rudder is extracted. This section is then extruded in spanwise

direction as shown in Fig. 2.4 (Sec. 2.2). This allows to include the effect of the large sweep angle of the VTP leading edge of 44° and to assess the effects of varying the slot length and the number of slots in spanwise direction. The span of the computational model is kept constant during the investigation. In onset flow direction the airfoil corresponds to the one of the 2D investigation. The slot height is kept constant at the value derived from the 2D investigations with $h_{\text{slot}}/c = 0.0006$.

In the following, first a continuous slot is investigated which covers the whole span. In a next step it is replaced by discrete slots. The intention is to make the blowing more efficient by achieving a decrease in the required mass flow rate for the same or a similar increase of the side force coefficient. Since the sweep angle of the VTP varies from the leading to the trailing edge, a change in the sweep angle is examined as well. Finally, pulsed blowing is investigated for selected discrete slot configurations and the effect on the mass flow rate and the resulting side force coefficient is analyzed. A part of the results presented in this chapter were published in [96] for the assessment of constant blowing and in [97] for pulsed blowing.

4.2.1 Continuous Slot

Since the continuous slot extends over the whole span it also has the largest slot area. This means that it requires the largest mass flow rate for a given jet velocity which can be calculated by multiplying the velocity and density of the jet with the area of the slot orifice. The results of the continuous slot are used in the following as a reference for the side force coefficient C_S which can be reached and the mass flow rate which is required.

Without blowing the flow on the rudder is separated as it is the case in 2D. In 2.5D this becomes apparent by skin friction lines going in spanwise direction. With blowing activated the skin friction lines on the rudder are at first oriented in the blowing direction of the slots which is perpendicular to the hinge line as can be seen in Fig. 4.25. Since the jet velocity or momentum coefficient is not large enough to achieve attached flow on the whole rudder, the skin friction lines again turn in spanwise direction further downstream towards the trailing edge. Here the flow is separated. With a further increase in jet velocity the flow can be kept attached up to the trailing edge at a C_μ of 1%. With blowing activated the surface pressure coefficient shows two suction peaks: one at the leading edge of the fin and one at the rudder shoulder. With increasing jet velocity the suction peak at the rudder shoulder grows. Since information is propagated in all directions in subsonic flow, the flow upstream at the leading edge of the fin is also affected. Downstream on the rudder the area with flow separation is reduced. In the top view in Fig. 4.25 the high sweep angle of the incoming flow is visualized approximately by the skin friction lines on the fin. The behavior of side force and the drag coefficient are depicted in Fig. 4.26. The progression of the curves is similar to the ones obtained for the 2D geometry. For the 2D geometry the C_μ at which the flow can be attached up to the trailing edge is 1.4% while it is 1% in case of the 2.5D geometry. The factor between them is about the difference in length of the rudder in blowing direction, i.e. perpendicular to the hinge line. In this direction the 2D rudder is longer by a factor of $1/\cos(44^\circ) = 1.39$ than the 2.5D one.

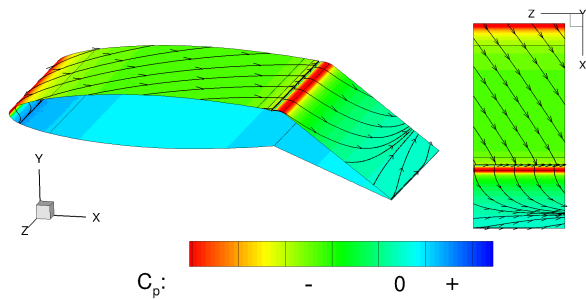


Fig. 4.25 Surface pressure coefficient and skin friction lines for the continuous slot, $C_{\mu} = 0.08$, Left: view from top aft, right: top view with the onset flow coming from the top left

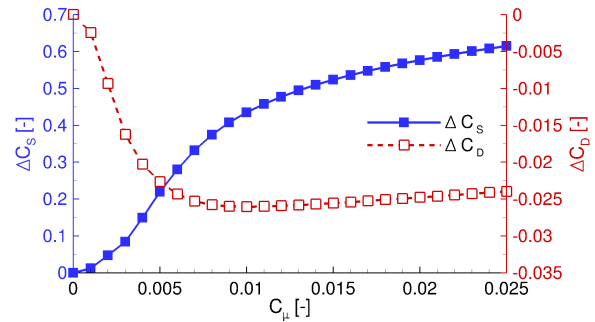


Fig. 4.26 Side force and drag coefficient increment versus momentum coefficient for the continuous slot.

4.2.2 Discrete Slots

Using discrete slots, just part of the span is covered by slots. Three example configurations are depicted in Fig. 4.27. This reduces the total orifice area in comparison to the continuous slot. Since the span of the wing section is kept constant during the whole investigation, the width of the slots is selected to enable a uniform distribution for a specified number of slots along the given span.

A comparison of the different discrete slot configurations is done for three different jet velocities. These jet velocities are 169 m/s, 207 m/s and 239 m/s. They correspond to the ones for the continuous slot at momentum coefficients of 1%, 1.5% and 2%. Since the momentum coefficient also includes the slot area, a better comparison is enabled here when keeping the jet velocity constant. Otherwise, if C_{μ} would be kept constant, a change in the slot area would at the same time also lead to a change of the jet velocity. For a very small slot this could for example lead to a jet velocity beyond the speed of sound if C_{μ} has to stay the same. The geometric characteristics of the different slot configurations are summarized in Tab. 4.1.

Flow Effects with Discrete Slots

Using several discrete slots in comparison to one continuous slot changes the flow topology on the rudder. With discrete slots jets with finite width are blowing downstream over the rudder. At each jet a counter-rotating vortex pair is created which is not present for the full span jet. These longitudinal vortices can be seen in Fig. 4.28. Here field slices are used for the visualization of the vortices which are colored with ω_x , the x -component of the vorticity. In addition, field streamlines are shown in the vicinity of one vortex pair. The view is from the back onto the rudder. From this point of view the blue vortices on the right of each vortex pair with negative ω_x are rotating clockwise and the red ones to their left rotate counter-clockwise.

For the creation of the vortex pairs two effects come into play. The first one is the finite width of the jets and was already mentioned. The second effect is the angle of the jet blowing direction relative to the direction of the flow coming from the fin. At some

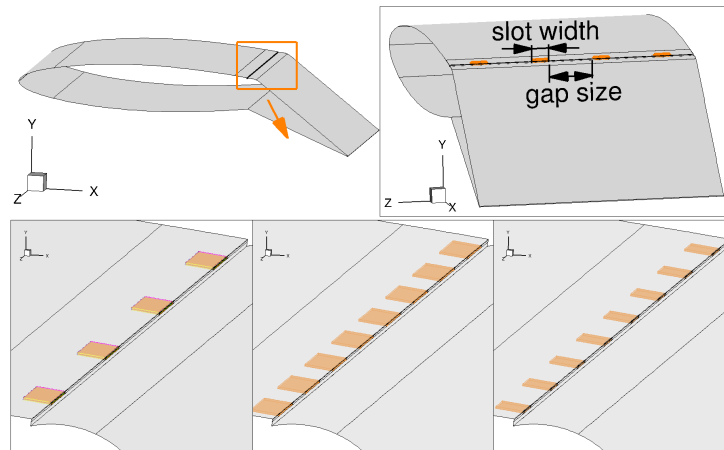


Fig. 4.27 2.5D VTP section with a detail view of three different slot configurations on the bottom (shown in orange including their extension in chordwise direction inside the fin). Left: 4 slots, mid: 8 slots with identical slot width, right: 8 slots with halved slot width; top right: aft view of the 2.5D model

Tab. 4.1 List of slot variations for the 2.5D geometry

Number of slots N	Slot width w [mm]	Gap size between slots g [mm]
1	76.4	76.4
1	38.2	114.7
1	30.6	122.3
1	19.1	133.8
1	9.6	143.3
1	4.8	148.1
2	57.3	19.1
2	38.2	38.2
2	28.7	47.8
2	19.1	57.3
2	9.6	66.9
2	4.8	71.7
4	19.1	19.1
4	9.6	28.7
4	4.8	33.4
8	9.6	9.6
8	4.8	14.3

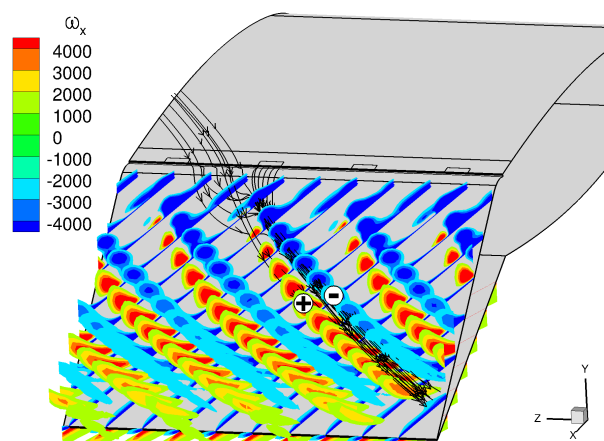


Fig. 4.28 Streamlines and field slices showing the vortices over the rudder

point the flow close to the surface and coming from the fin meets the jet. It first wants to stay in its original direction and tries to push the jet in its direction as well. However, the jet has a higher velocity than the surrounding flow. Due to this, close to the rudder shoulder the flow remains attached in the path of the jet even for lower jet velocities. The flow from the fin, having a velocity component in spanwise direction, tries passing over the jet. This creates shearing with the jet, inducing a rotation leading to the blue vortex in Fig. 4.28. On the side where this vortex is rotating upwards away from the surface the counter-rotating red vortex with positive rotation direction is induced.

Between the two vortices an upwind region is created where fluid is transported away from the surface. Locally this is detrimental and weakens the flow there. Looking at the other side of each vortex where they are rotating towards the surface their effect is beneficial. Here they transport high energy fluid into the near-surface boundary layer stabilizing the flow there. Due to this the flow stays attached between the jets. How effective this works depends on the slot width and the gap between them, the number of slots and on the jet velocity. This is described in more detail in the next sections. Two approaches are used for analyzing the results: first for a constant jet velocity and then for a constant slot width.

Effect of Slot Variations at Constant Jet Velocity

This section discusses the effect of a variation of the number of slots and the slot width on the side force coefficient while keeping the jet velocity constant. The middle jet velocity of 207 m/s is selected. The results are presented in Fig. 4.29 for the increment of the side force coefficient referenced to the value without blowing versus the momentum coefficient. For a specific C_S the most efficient slot configuration is the one requiring the smallest C_μ . Since the jet velocity is constant the momentum coefficient is varying proportionally to the slot area and is thus directly scaling with the mass flow rate. The same slot area can result for example from two wide slots or four slots with halved width. Each curve in the diagram represents a constant number of slots. Due to the fixed jet velocity the slot area increases with increasing C_μ having slots with an increased width and reduced gap size between the slots. In this study the slot area is increased in principle by doubling its width until the cumulated slot width would lead to zero gaps or exceed the overall span of the computational model, but a few intermediate

slot widths were added for some cases. For a given C_μ the cumulative slot area is constant. The dotted line depicts the results for the continuous slot and the full range of jet velocities as reference. The filled circle at $C_\mu = 0.015$ or 1.5% is the data point for the jet velocity considered here.

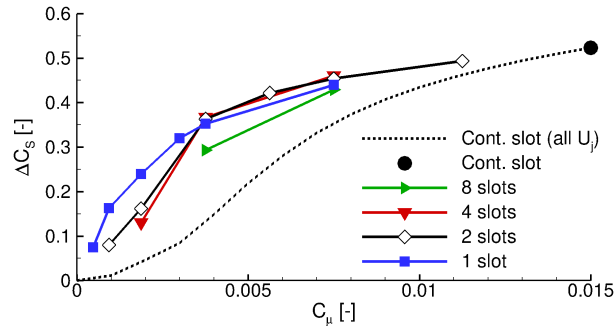
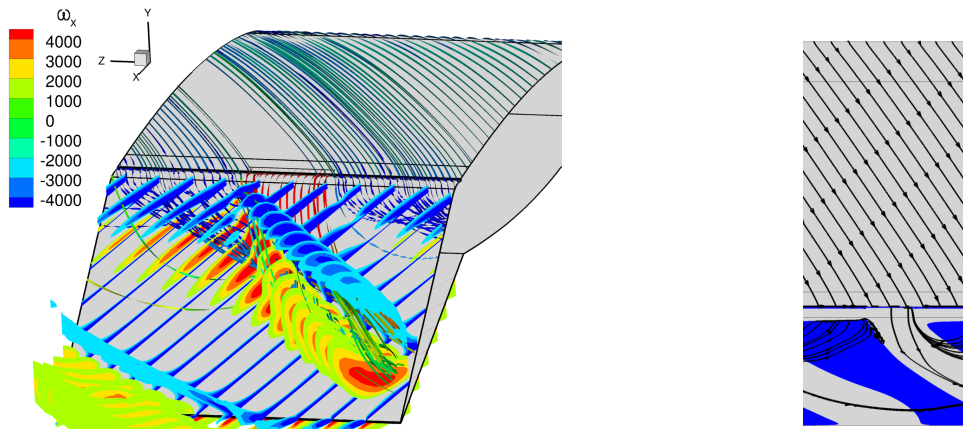


Fig. 4.29 Side force coefficient increment versus the momentum coefficient at $U_j = 207$ m/s

All curves with discrete slots in the diagram lead to higher side force coefficients for the same C_μ than the continuous slot. This holds only as long as an alternative to the continuous slot is possible for the selected C_μ . It can also be observed that the side force coefficient is increasing with increasing C_μ . Because the largest C_μ at fixed jet velocity results from the largest slot area, the largest C_s is generated by the continuous slot.

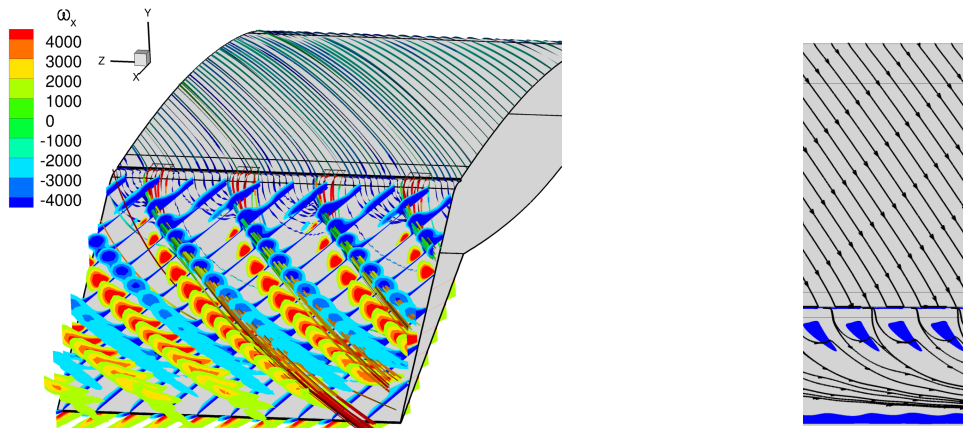
For a momentum coefficient of $C_\mu = 0.38\%$ the results are exemplarily discussed in more detail. Field slices showing the vortices over the rudder colored with ω_x and streamlines are presented in Fig. 4.30, Fig. 4.31 and Fig. 4.32 for 1, 4 and 8 slots. Included in those figures is also a top view of the geometry in part b) which shows the skin friction lines and in blue the areas of reversed flow with negative skin friction coefficient C_{fx} . The latter gives an indication of separated flow. The field streamlines in part a) of the figures are colored with total pressure. Red represents a high and blue a low value. This allows to easily identify the location of the slots due to the red color of the streamlines at the rudder shoulder.

The highest increase in the side force coefficient at $C_\mu = 0.38\%$ can be found for the slot configuration with four slots. It is closely followed by the one-slot configuration. The results for $N = 2$ are in between those of $N = 1$ and $N = 4$, also from the topology of the vortex pattern, and are not shown in detail. The results for eight slots lead to a somewhat smaller C_s . Looking at the one-slot configuration in Fig. 4.30 it can be seen that a large vortex pair is created. It has the largest reach into the flow field perpendicular to the surface and also the largest extent in spanwise direction. It influences a comparatively large area on the rudder and can transport higher energy fluid from farther away into the flow field close to the rudder surface. This makes the one-slot configuration also quite effective for small momentum coefficients. Concentrating all mass flow on one jet leaves a noticeable effect on the surrounding flow while smaller jets tend to be easier influenced, following the outer flow rather quickly. However, the large slot width is also accompanied by relatively large gaps between the slots where the vortex system does not cover the whole span. This leads to areas with separated flow between the jets as can be seen in Fig. 4.30(b), reducing C_s . The flow topology of the two-slot configuration is quite close to the one from the configuration with one slot, but the areas with negative skin friction coefficient are smaller in spanwise direction.



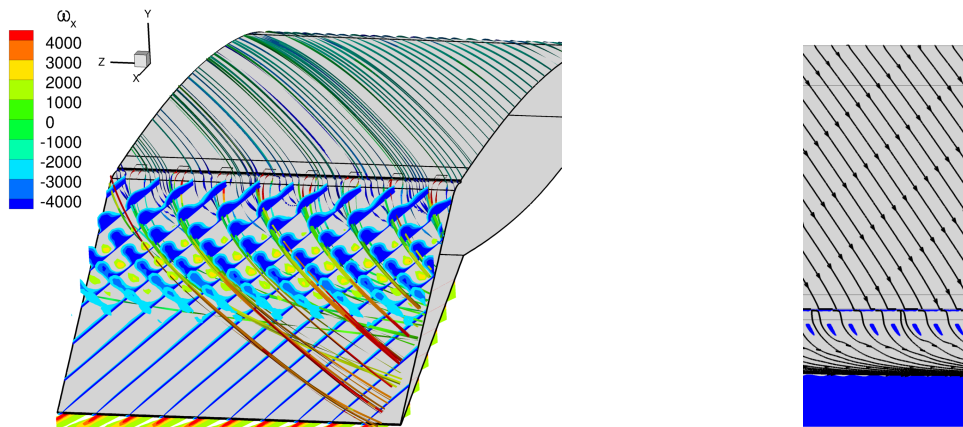
(a) Streamlines (p_t) and vortices (ω_x) (b) $C_{fx} < 0$ (blue) and skin friction lines

Fig. 4.30 $N = 1, w = 38.2\text{mm}, U_j = 207\text{ m/s}, C_\mu = 0.38\%$



(a) Streamlines (p_t) and vortices (ω_x) (b) $C_{fx} < 0$ (blue) and skin friction lines

Fig. 4.31 $N = 4, w = 9.6\text{ mm}, U_j = 207\text{ m/s}, C_\mu = 0.38\%$



(a) Streamlines (p_t) and vortices (ω_x) (b) $C_{fx} < 0$ (blue) and skin friction lines

Fig. 4.32 $N = 8, w = 4.8\text{ mm}, U_j = 207\text{ m/s}, C_\mu = 0.38\%$

For the intermediate arrangement with four slots the combination of slot width and gap width is such that the flow is attached between the jets. Just a small area close to the trailing edge still shows separated flow in Fig. 4.31. Increasing the jet velocity to 239 m/s would add sufficient energy to the boundary layer to lead to fully attached flow also close to the trailing edge (cf. Fig. 4.35). Small blue areas with reversed flow only remain near the rudder shoulder. In this area the flow separation would start without flow control. Since the vortices are not yet fully developed in this region, they do not cover the full span as it is the case further downstream.

In Fig. 4.32 eight blowing slots are distributed along the available span. While the slots were spaced too far apart in the one-slot configuration compared to the four-slot case, their spacing is now too dense. The jets are too close together, hindering the development of sufficiently large vortex structures. The clockwise-rotating vortex in Fig. 4.32(a) is small and weak in its magnitude of ω_x . Since the additional effect of this second vortex is missing, the aft part of the rudder is separated as indicated by the blue area in Fig. 4.32(b). This leads to a noticeably smaller C_S compared to the two other configurations at the same mass flow rate. Increasing the jet velocity would lead in principle to the same picture but now with the streamlines oriented more in the blowing direction. Furthermore, the portion of the chord having separated flow close to the trailing edge would reduce.

Increasing the slot width further and by this the mass flow rate leads to larger regions of attached flow on the rudder and to a further increase in the side force coefficient as depicted in Fig. 4.29. For the four-slot configuration doubling the slot width leads to fully attached flow up to the trailing edge at $C_\mu = 0.75\%$. The same is true for the two-slot configuration but with somewhat larger separation areas between the jets close to the rudder shoulder. For the one-slot configuration a small area of reversed flow between the jets can still be found all the way up to the trailing edge. For this higher momentum coefficient the increment in ΔC_S for a certain increase in C_μ decreases in a similar way as it was observed for the 2D investigation. The side force increments for the different discrete slot configurations do not differ that much any more. The curves of the discrete slot configurations approach the curve of the continuous slot. However, the largest increase in the side force coefficient can only be reached by the continuous slot at the expense of the largest mass flow rate.

Effect of Slot Variations at Constant Slot Width

In the previous section the jet velocity was kept constant. In this section the results with a constant slot width of $w = 9.6$ mm are discussed. This width is selected since it showed the highest gain in C_S with the four-slot configuration at $C_\mu = 0.38\%$ (cf. Fig. 4.29). For higher C_μ it was found that the gradient of the increase in side force coefficient decreased. The parameters which are varied now are the number of slots and with this the size of the gap between the slots. The results are presented in Fig. 4.33. Each curve is composed of data points with varying jet velocity. The point of the curve at the smallest C_μ is the one for a jet velocity of 169 m/s. The jet velocity is then increased to 207 m/s and further to 239 m/s and with this also the increment in the side force coefficient achieved. In Fig. 4.34 the same results are depicted versus the mass flow coefficient. In contrast to Fig. 4.29 now both the slot area and the jet velocity are varied, so that not only the scale on the horizontal axis changes compared to the C_μ -diagram

but also how the curves are positioned with respect to each other.

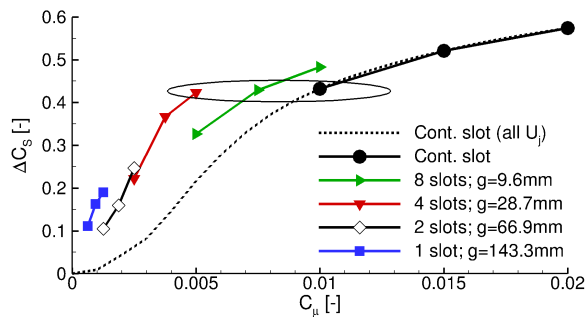


Fig. 4.33 Side force coefficient increment versus the momentum coefficient at a constant slot width $w = 9.6$ mm and varying gap size g

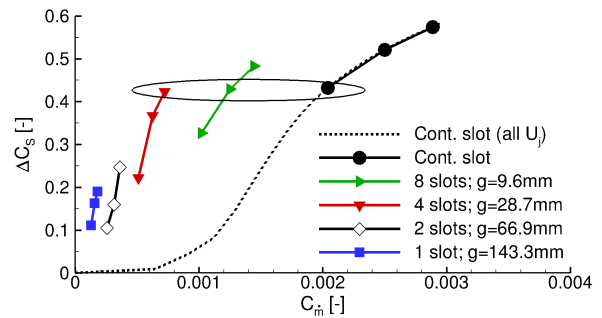
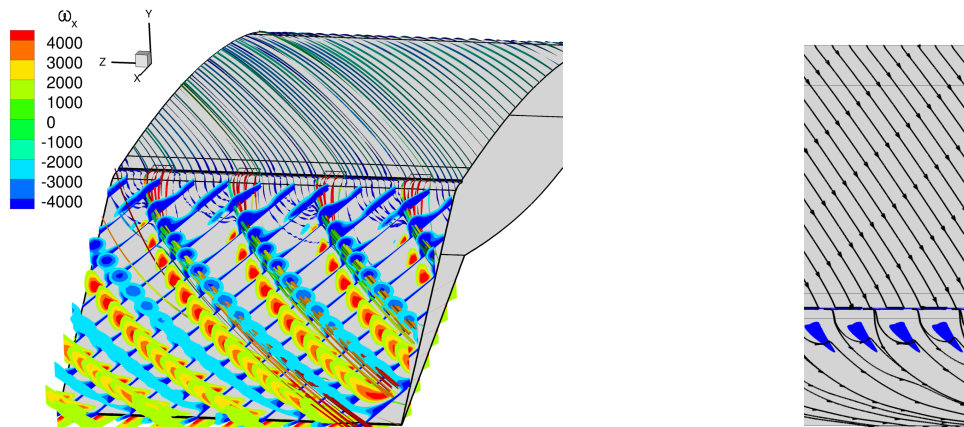


Fig. 4.34 Side force coefficient increment versus the mass flow coefficient at a constant slot width $w = 9.6$ mm and varying gap size g

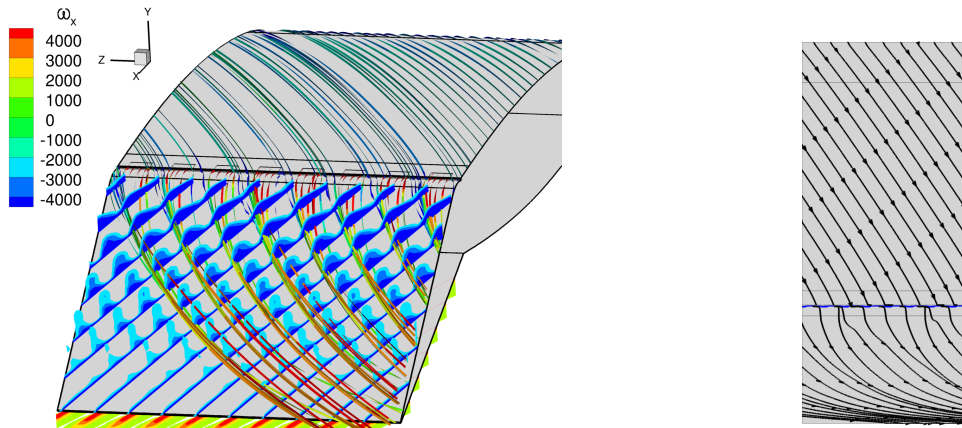


(a) Streamlines (p_t) and vortices (ω_x) (b) $C_{f,x} < 0$ (blue) and skin friction lines

Fig. 4.35 $N = 4, w = 9.6$ mm, $U_j = 239$ m/s, $C_\mu = 0.5\%$

The figures reveal that the more slots are used, the larger the required C_μ and mass flow coefficient for a constant jet velocity become, but also the more the maximum side force coefficient is increased. The maximum side force coefficient for the one- and two-slot configurations are so small compared to the other ones that they are most likely not of interest for application on a 3D vertical tail. The side force coefficient could only be increased by a larger slot width as was seen in Fig. 4.29, but this would also remove the advantage of the low mass flow rate requirement. The largest side force increase can again be found for the continuous slot.

In Fig. 4.33 three data points are encircled which approximately lead to the same ΔC_s of 0.42. These are now discussed in more detail. All encircled configurations show attached flow up to the trailing edge. Varying is the area of separated flow between the jets close to the rudder shoulder where the vortices are not yet fully developed. It is obvious that the four-slot configuration needs the lowest C_μ of only 0.5% to obtain the side force coefficient increment under consideration. At the same time, the mass flow coefficient of 0.0007 is the smallest as shown in Fig. 4.34. Compared to the continuous slot



(a) Streamlines (p_t) and vortices (ω_x) (b) $C_{fx} < 0$ (blue) and skin friction lines

Fig. 4.36 $N = 8$, $w = 9.6$ mm, $U_j = 207$ m/s, $C_\mu = 0.75\%$

configuration which needs $C_\mu = 1\%$, this is a large reduction of 50% in the momentum coefficient and for the mass flow rate a reduction of 65%.

To get a better understanding of the flow field, the vortices on the rudder and the areas of reversed flow are depicted in Fig. 4.35 and Fig. 4.36 for the configurations with four and eight slots respectively. The four-slot configuration shows a good coverage of the rudder surface by the vortex system in the spanwise direction. Compared to the eight-slot configuration the blue areas with reversed flow close to the rudder shoulder are still present, leading to the slightly smaller ΔC_S as shown in Fig. 4.33. In Fig. 4.36(a) the depiction of the vortices for the eight-slot configuration shows that the second, counter-clockwise-rotating vortex is missing. The slots are too close together preventing the development of the counter-rotating vortices. The jet velocity is smaller than for the four-slot configuration at this C_S but the slot area is doubled since the slot width is kept constant. Overall, this leads to an increase in the momentum coefficient and also in the mass flow rate required.

In summary it can be stated that for a specific increase in C_S the slot configuration with the highest jet velocity and the smallest number of slots leads to the lowest mass flow rate requirement and is thus most efficient.

4.2.3 Effect of the Sweep Angle

The four-slot configuration with $w = 9.6$ mm, which was shown to be quite efficient in the previous section, is used for a further investigation on the effect of the sweep angle. For the 2.5D geometry the sweep angle at the leading and at the trailing edge is the same. So far the leading edge sweep angle of the 3D VTP was used. For a 3D vertical tailplane the sweep angle at the leading edge is larger than that at the hinge line where the blowing slots are positioned. The effect of the sweep angle, which corresponds in this investigation to the angle of the incoming flow with the jet blowing direction, is examined in this section.

Using the geometry as it is and then varying the sweep angle would lead to a decreased length in onflow direction which the flow would have to travel over the fin and rudder. Thus it was decided to keep the airfoil in onflow direction constant during this study.

This is sketched in Fig. 4.37. For smaller sweep angles the chord length parallel to the top and bottom boundaries increases, scaling with the cosine of the sweep angle and being largest when it is zero. Since the span of the calculated section is kept constant, the VTP area changes with the sweep angle. For the calculation of the coefficients C_S and C_μ the respective area for each sweep angle is used as reference area.

The results for the side force coefficient increment ΔC_S versus the jet velocity are presented in Fig. 4.38. The increment in C_S is the value of the configuration without blowing from which the result with blowing activated at the same sweep angle is subtracted. Each curve depicts the results for the three jet velocities used before, i.e. 169 m/s, 207 m/s and 239 m/s. The sweep angle is varied from 0° to 40° in 10° -steps. In addition, the results for the sweep angle of 44° used so far are included.

The relatively large variation in the results shows that the sweep angle can have a significant influence on the gain in the side force coefficient. The largest increase is obtained for the configuration with 30° sweep angle. With further increasing sweep angle, the side force coefficient increment reduces. Lowering the sweep angle below 30° also leads to a reduction in C_S , but this time it is even larger. Thus, the larger sweep angles are preferred to the small ones. Without or with only 10° sweep angle the increase in the side force coefficient due to blowing is merely about $1/5^{\text{th}}$ of the result with 30° sweep angle. An increase of the jet velocity leads to an increase of the side force coefficient which is less pronounced for small sweep angles.

With decreasing sweep angle the angle between the incoming flow and the jet direction, which is perpendicular to the hinge line, i.e. parallel to the upper and lower boundaries in Fig. 4.37, reduces. This changes the vortex system over the rudder and is the reason for the considerable difference in the results. In Fig. 4.39 this is exemplarily depicted for the middle jet velocity of 207 m/s by the areas of reversed flow marked in blue and the skin friction lines. The vortices over the rudder are visualized in Fig. 4.40.

For the three larger sweep angles the flow on the rudder is attached up to the trailing edge. Only close to the rudder shoulder areas of reversed flow are present where the

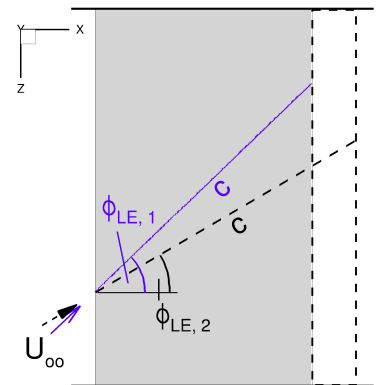


Fig. 4.37 Top view of the VTP section (stretched span) for two different sweep angles

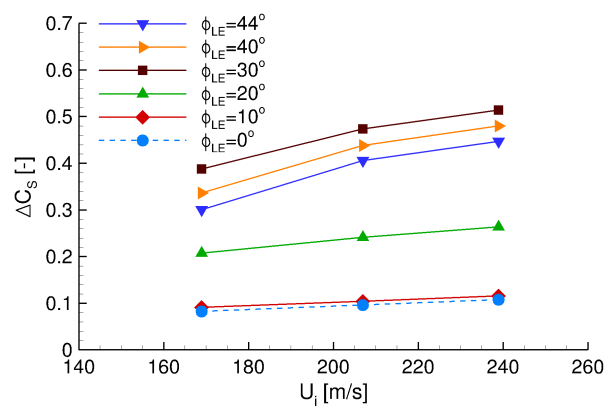


Fig. 4.38 Side force coefficient increment versus jet velocity for a sweep angle variation

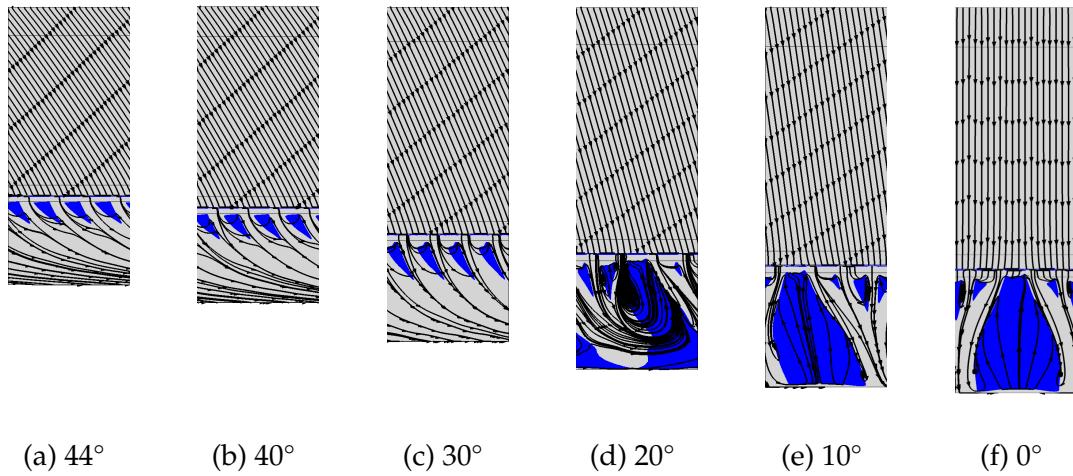


Fig. 4.39 Top view onto the VTP section: skin friction lines and areas marked with $C_{fx} < 0$ (blue) for different leading edge sweep angles, $U_j = 207$ m/s

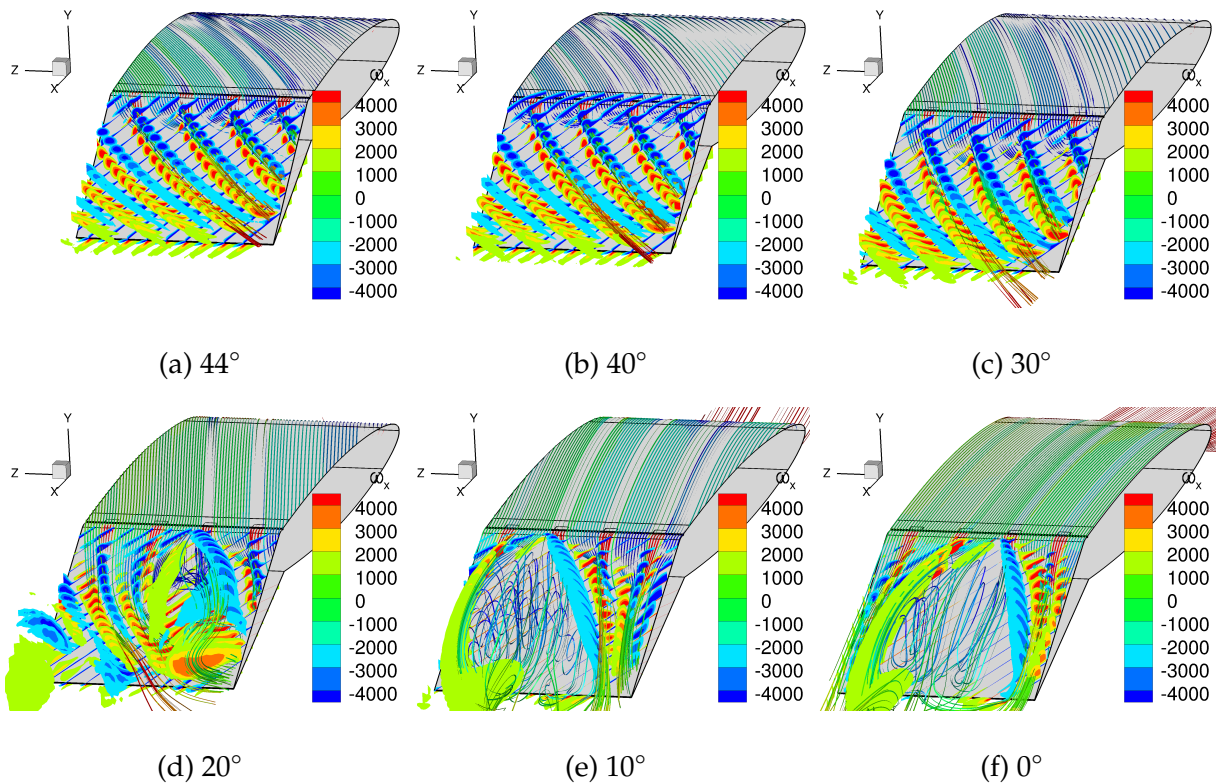


Fig. 4.40 Aft view of the VTP section: field streamlines (p_t) and vortices (ω_x) for different leading edge sweep angles, $U_j = 207$ m/s

vortex system is not yet fully developed (Fig. 4.39 a) to c)). The vortices over the rudder in Fig. 4.40 a) to c) correspond to these figures and show a regular pattern of the vortices traveling downstream. For the configuration with 30° sweep angle the vortices are somewhat larger than those at higher sweep angles. This leads to a better coverage of the span and to the somewhat increased side force coefficient.

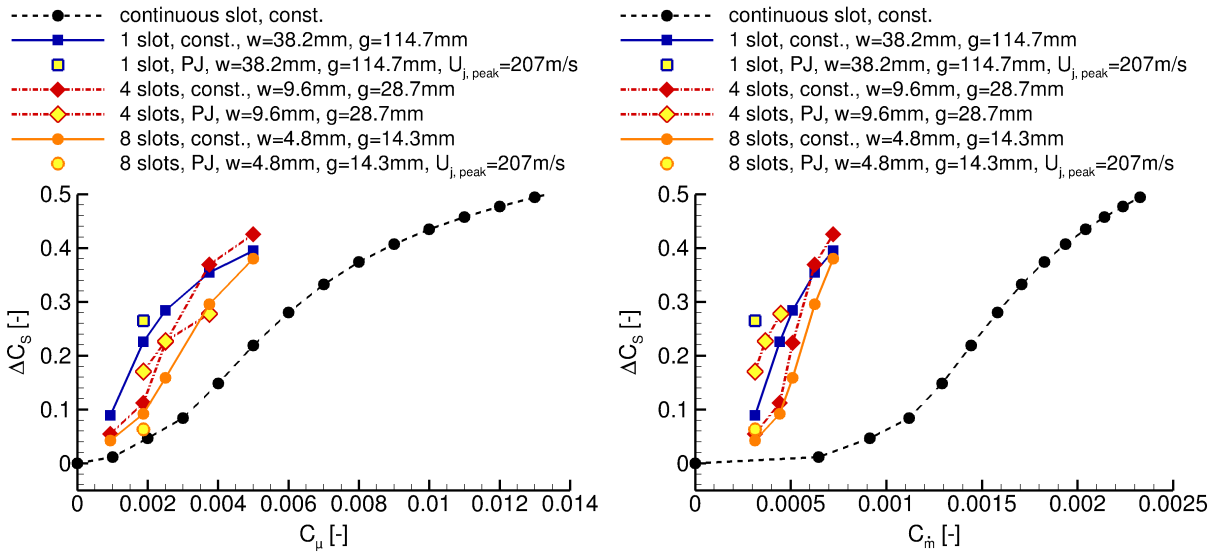
For the three smaller sweep angles of 20°, 10° and 0° with the noticeably decreased side force coefficient in Fig. 4.38 the flow on the surface and the vortices look quite different, too. The vortex system is not regular any more. The jets can create an attached band of flow up to the trailing edge as can be seen in Fig. 4.39 d) to f). However, between these narrow bands the flow is separated on large parts of the rudder. This also explains the loss in C_S . In these cases the angle between the incoming flow and the jets is too small, preventing the development of a regular vortex system. The irregularity of the flow field might also indicate a certain level of unsteadiness which cannot be captured correctly by the steady flow simulation applied here but can be used to verify if a regular pattern of attached flow develops which would indicate an effective blowing configuration. Tangential blowing from discrete slots works best if an angle between the jet direction and the incoming flow exists. For lower sweep angles the flow separation alters the jet path. Due to this the jet direction locally has an angle to the surrounding flow, enabling the creation of the vortices but also leaving regions of separated flow in between.

It can be summarized that the angle of the incoming flow to the blowing direction of the jets has a significant influence on the vortex system and the obtained side force coefficient. A sweep angle of 30° leads to the largest increase in C_S among the cases presented here. This is approximately the sweep angle of the hinge line of the 3D VTP. Thus, blowing perpendicular to the hinge line seems to be the best blowing direction for this 3D VTP.

4.2.4 Effect of Pulsed Blowing

The 2D investigation with a continuous slot as described in Sec. 4.1.7 has shown an increase in side force coefficient when using pulsed blowing compared to constant blowing — especially for low momentum coefficients. The effect of pulsed tangential blowing for the already introduced discrete slot configurations will be investigated in this section. As for most results shown for the 2.5D configuration the sweep angle is 44°. Like in 2D, the investigation is carried out using unsteady RANS (URANS) simulations. Blowing is activated half the time of one period leading to a duty cycle of 0.5. The actuation frequency is 420 Hz, corresponding to $F^+ = 1$ which was also used in the 2D investigation.

In Fig. 4.41 the side force coefficient increment is depicted versus the momentum coefficient. The dashed line shows the results for the continuous slot calculated using the steady RANS equations. Results with constant blowing, partially already presented in Sec. 4.2.2, are depicted and complemented with results from pulsed blowing simulations. The side force coefficient is referenced to the RANS result without blowing for steady and unsteady calculation results. As was already seen in the 2D results, the C_S -value for very low momentum coefficients is a bit smaller when obtained using the URANS compared to the steady RANS approach. The computed difference is 0.03 if no blowing is applied. This introduces an uncertainty in the same order of magnitude or lower and has to be kept in mind. However, since the uncertainty is rather small it does



(a) Side force coefficient increment vs. momentum coefficient (b) Side force coefficient increment vs. mass flow coefficient

Fig. 4.41 Comparison of side force coefficients for constant (const.) and pulsed (PJ) blowing results for the 2.5D geometry for a variation in the numbers of slots

not have an impact on the conclusions drawn from the investigations in this section. Above the dashed line several other curves show the results for blowing through discrete slots. Curves which have symbols in the same color represent constant blowing while yellow-filled symbols represent results with pulsed blowing.

First the four-slot configuration represented by the two red curves with dash-dotted line is considered. With pulsed blowing, results for three different jet velocities are depicted. The peak velocities during one actuation cycle going from smaller to larger C_μ or mass flow rate are 207 m/s, 242 m/s and 292 m/s. The mean jet velocities over one period are half of those values due to the duty cycle of 0.5. The side force coefficient shown is the result of averaging over one period. For constant blowing, since the jets are active all the time, half of the jet peak velocity of the respective pulsed blowing case is used to arrive at the same C_μ . Here, similar to the 2D results, for small C_μ pulsed tangential blowing leads to a larger gain in the side force coefficient than constant blowing. This reverses when increasing C_μ to 0.38%. Thus it appears that pulsed blowing is only superior in terms of side force gain for small C_μ . However, here the magnitude of the C_S -increments is quite low. Consequentially, tangential pulsed blowing is less interesting if higher gains in side force coefficient are required. Two more slot configurations are displayed in Fig. 4.41(a). While some benefit can also be seen for the one-slot configuration when using pulsed blowing for small momentum coefficients, pulsing is detrimental for the eight-slot configuration with its quite densely spaced slots — even at low momentum coefficients.

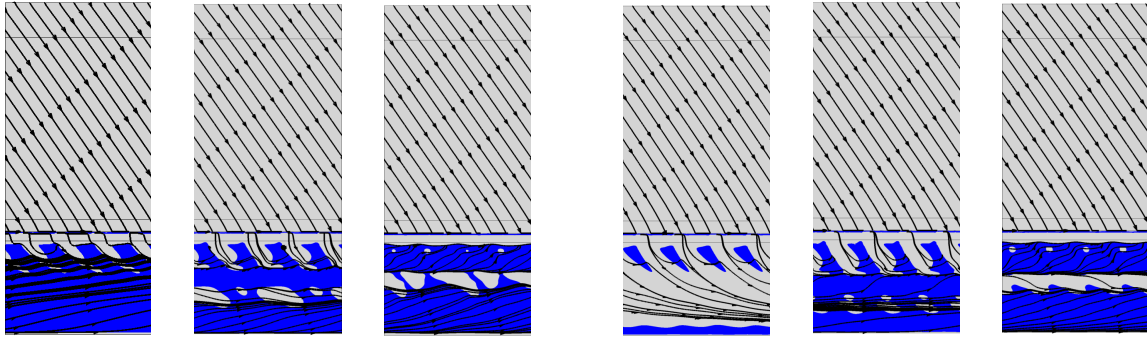
However, the pulsed blowing approach is beneficial when considering the mass flow coefficient in Fig. 4.41(b). Since blowing is only active half the time the mass flow rate reduces. If only very small increments in C_S are sufficient, this approach might be considered, but it has to be kept in mind that the complexity of the blowing system is higher for pulsed blowing due to the required ability to switch the jets off and on with a prescribed frequency.

The four-slot configuration is selected for a deeper analysis of the results at two different momentum coefficients. A comparison of the negative C_{fx} , i.e. areas of reversed flow, at $C_\mu = 0.19\%$ and $C_\mu = 0.38\%$ for constant and pulsed blowing is presented in Fig. 4.42 and Fig. 4.43. In addition, the aft view on the rudder showing the vortices is depicted in Fig. 4.44 and Fig. 4.45 for both momentum coefficients. Except for the constant blowing result for the larger C_μ all configurations have separated flow on large parts of the rudder. The field streamlines bend away from the surface in the first third to half of the rudder chord. With pulsed blowing they are turning towards the rudder surface again a bit further downstream. This corresponds to the spots without separated flow in Fig. 4.42 and Fig. 4.43 showing $C_{fx} < 0$. For the small C_μ the larger jet peak velocity helps to create larger vortices over the rudder than with constant blowing. Due to the pulsing they get smaller during the time without blowing but overall nevertheless result in more attached flow on the rudder and a higher side force coefficient. Since for constant blowing the velocity ratio of the jet to the surrounding flow is rather low, only a small effect on the flow is obtained. For the larger C_μ and constant blowing the jet velocity is already large enough to keep the flow attached along most of the chord, leading to a higher increase in the side force coefficient. Despite the higher jet peak velocity for pulsed blowing, the effect of the vortices in attaching the flow is reduced, resulting in a smaller increase in C_S compared to constant blowing.

The reduction of the effect of the discrete slots with pulsed blowing in comparison to constant blowing for the higher C_μ might be explained as follows. With pulsed blowing the vortex system is more irregular due to turning the jet on and off periodically. At the start of each period the jet has to accelerate the slow, low-energy fluid aft of the slot again which is not the case for constant blowing where the jet remains active all the time. In addition, the vortices created by pulsed blowing seem to interfere with each other in spanwise direction due to the cross flow on the rudder. This reduces the energy remaining to keep the flow attached. Another point to consider is that the vortices are much larger for pulsed blowing than for steady blowing because the jet velocity is much larger. Since the slot spacing was designed for steady blowing, the adjacent vortex pairs with their increased size are now quite close together. In order to show the full potential of pulsed blowing through discrete slots it might be necessary to find a slot spacing which is more optimized for the higher jet velocity in combination with pulsed actuation. This is a whole new optimization task which is not pursued further. Here, it can only be concluded that using the same slot configuration as for constant blowing is not beneficial with pulsed blowing if higher gains in side force coefficient are required. A variation of the blowing frequency might also lead to different results. Using the frequency which was shown to be beneficial for more 2D-like flows might not be beneficial with such a strong cross flow.

4.2.5 Summary

The use of discrete slots compared to a full-span slot leads to the creation of a counter-rotating vortex pair at each jet if the slots have sufficient space between them. Compared to the 2D investigation or the continuous slot, the jet does not only feed energy directly to the boundary layer, but the vortex system leads in addition to an increased mixing of the outer and near-surface flow. This helps increasing the energy of the boundary layer as well, also between the jets, and thereby with keeping the flow on the rudder attached.



(a) Constant blowing (b) Pulsed blowing, AFC on (c) Pulsed blowing, AFC off

Fig. 4.42 Top view of the VTP section: skin friction lines and areas marked with $C_{fx} < 0$ (blue), comparison of constant and pulsed blowing, $N=4$, $C_\mu = 0.19\%$

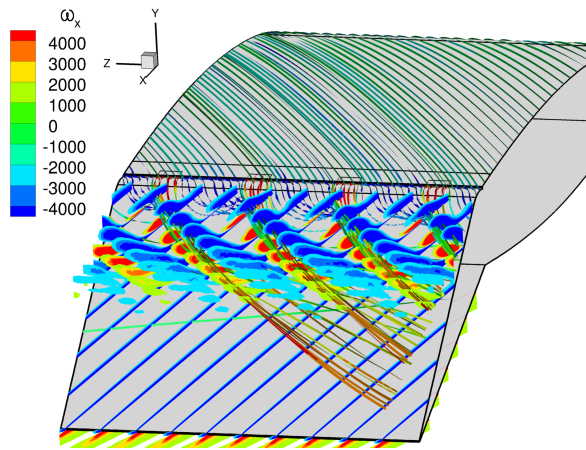
(a) Constant blowing (b) Pulsed blowing, AFC on (c) Pulsed blowing, AFC off

Fig. 4.43 Top view of the VTP section: skin friction lines and areas marked with $C_{fx} < 0$ (blue), comparison of constant and pulsed blowing, $N=4$, $C_\mu = 0.38\%$

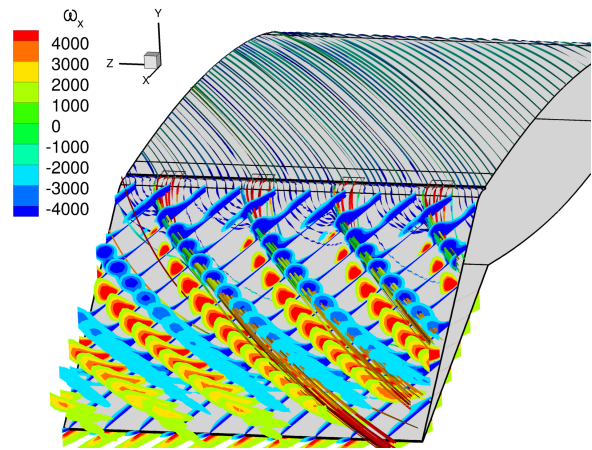
This again makes the discrete slot configurations more efficient than the continuous slot by requiring a smaller mass flow rate for the same increase in side force coefficient. But this entails a much larger jet velocity than for the continuous slot. In this case the speed of sound might limit the achievable side force coefficient increment. If raising the jet velocity does not result in an increase in the side force coefficient, the slot width has to be increased leading to a growth in mass flow rate and momentum coefficient. The maximum side force coefficient is obtained with the continuous full span slot at the expense of the largest mass flow rate.

For an efficient discrete slot configuration a suitable coverage with jets in spanwise direction is needed. Slots being too close to each other suppress the creation of the vortex pairs. Slots being too far apart from each other lead to vortex pairs which do not cover the whole span giving room to separated flow between them. It was found that for a constant slot width and about the same increase in side force coefficient the combination of a smaller number of slots and a higher jet velocity is more efficient, requiring less mass flow rate.

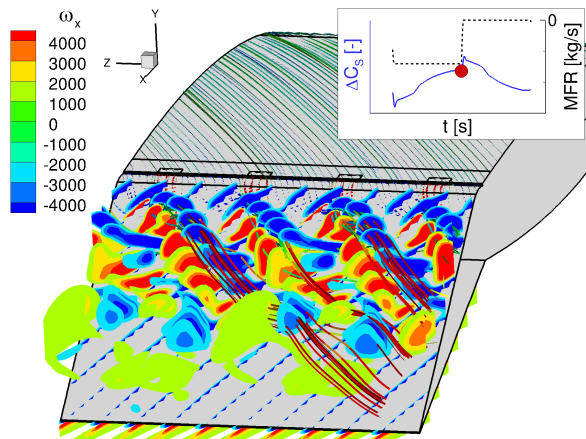
A variation of the sweep angle has shown that a 30° angle between jet and freestream flow direction leads to the highest increment in the side force coefficient. This 30° angle corresponds to the hinge line sweep angle of the 3D VTP, favoring blowing perpendicular to the hinge line. Using pulsed blowing seems to be effective in reducing the momentum coefficient or mass flow rate required even further. However, the side force coefficients which can be reached by this approach are relatively small. As such small increments are not thought to be of interest for practical applications, this type of blowing is not further investigated for the 3D case.



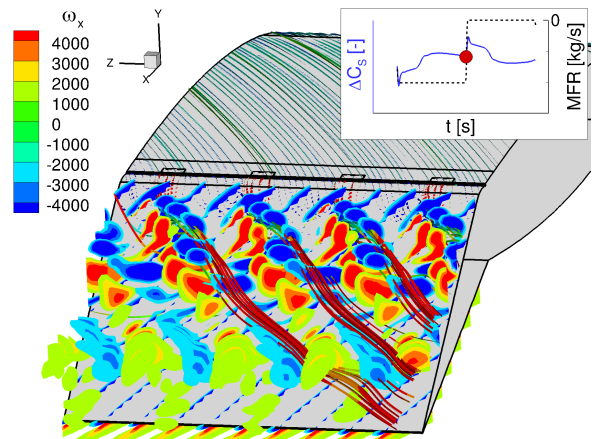
(a) Constant blowing



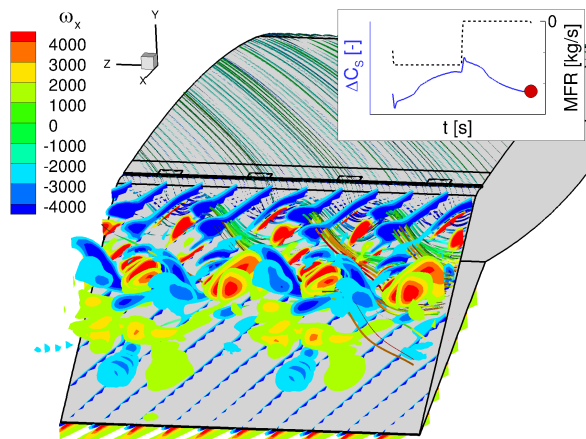
(a) Constant blowing



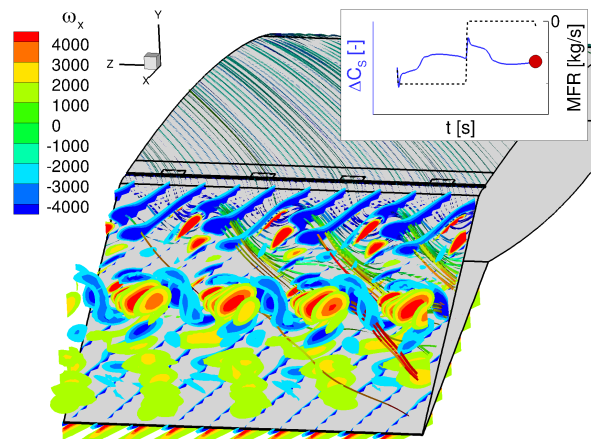
(b) Pulsed blowing, AFC on



(b) Pulsed blowing, AFC on



(c) Pulsed blowing, AFC off



(c) Pulsed blowing, AFC off

Fig. 4.44 Aft view of the VTP section: field streamlines (p_t) and vortices (ω_x), comparison of constant and pulsed blowing, $N=4$, $C_\mu = 0.19\%$

Fig. 4.45 Aft view of the VTP section: field streamlines (p_t) and vortices (ω_x), comparison of constant and pulsed blowing, $N=4$, $C_\mu = 0.38\%$

4.3 Investigations on a Full 3D Vertical Tail

The results from the 2D and 2.5D studies are now brought together for studying the mechanisms and effects of tangential blowing on a full 3D vertical tail. For the aerodynamic design of a tangential blowing system both effectiveness and efficiency are considered. Here, for the 3D geometry, not only a cross-flow component exists as for the 2.5D geometry, it also varies along the span as does the side force which is produced in each local spanwise section. In the following, first the baseline aerodynamics without blowing is described. A continuous slot is added in a next step which covers most of the span from root to tip. This should give the highest possible side force increase due to blowing since the slot area at fixed slot height is the largest and with this the momentum coefficient at fixed jet velocity. Going further, the most promising discrete slot configuration from the previous studies is now transferred to the 3D geometry. The effects analyzed and described include a variation of the jet velocity, the number of slots and the slot width in spanwise direction. A part of the results shown here were already presented in [98].

To allow a good comparison with the data from the validation experiment carried out at the TU-BS (e.g. [85]) the onflow velocity is slightly reduced. The resulting Reynolds number is $1.885 \cdot 10^6$ based on the VTP mean aerodynamic chord length of 0.5285 m at a wind tunnel velocity of 57 m/s, corresponding to a Mach number of 0.16 at a wind tunnel temperature of about 30 °C. The VTP reference area is 0.4217 m². Up to now it was assumed for most of the work that a step behind the slot exit towards the rudder surface exists, as it is assumed to be necessary for structural design (cf. discussion in Sec. 4.1.4). For the 3D geometry this step is omitted to replicate the condition of the wind tunnel model. This leads to a further increase in the side force coefficient as described in Sec. 4.1.4. The corresponding geometry in the vicinity of the step is shown in Fig. 4.46.

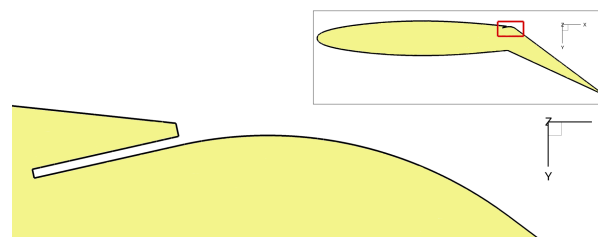


Fig. 4.46 Geometry in the vicinity of the blowing slot shown in a slice perpendicular to the rudder hinge line through the 3D VTP with the rudder deflected 30°

4.3.1 Baseline Flow

The baseline case without blowing will be described first. It already has the slot integrated in the geometry, but blowing is not active. The effect of the existence of the slot on the flow field and side force coefficient at the flow conditions considered is negligible. During the OEI maneuver where maximum side force is required, usually medium to large sideslip angles occur. Due to this, a variation in the sideslip angle β , corresponding to the angle of attack of a wing, will be discussed here as well. The simulation of each configuration is started from scratch at $\beta = 0^\circ$, with subsequent sideslip angles thereafter calculated as restarts from the previous angle.

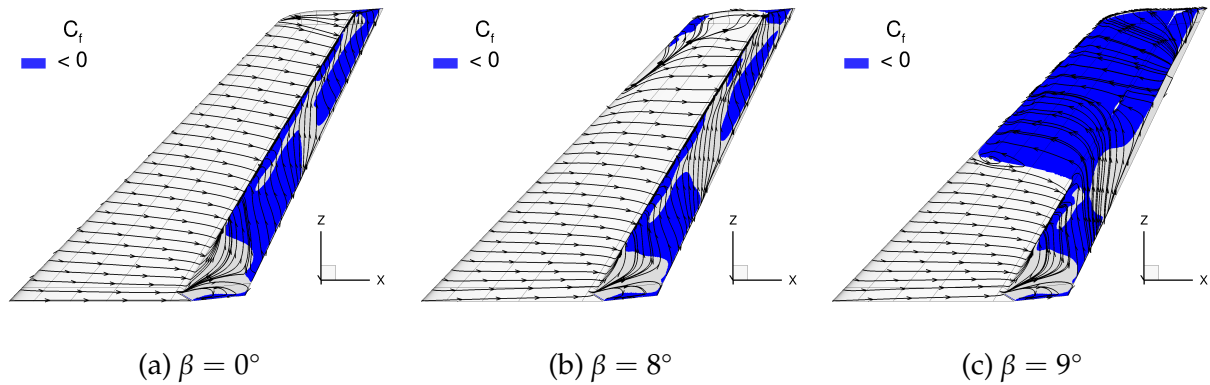


Fig. 4.47 Areas with negative skin friction coefficient (blue) and skin friction lines, baseline configuration, suction side

For a VTP with a symmetric airfoil and zero twist, the adverse pressure gradient triggering at some point the start of flow separation is influenced by several factors: the airfoil shape and thickness, the angle of sideslip, the rudder deflection angle and the planform. For the VTP at hand, the airfoil relative thickness is constant, but the point of maximum thickness moves aft from root to tip, increasing the adverse pressure gradient in the rear part of the VTP. The spanwise side force coefficient distribution of such an untwisted, tapered and highly swept planform without rudder deflection has its maximum at approximately 70% of the span, aggravating the adverse pressure gradient from the root to this point even further. Finally, the adverse pressure gradient caused by a rudder deflection has to be added. Once the strain on the flow is so high that it cannot overcome the adverse pressure gradient any more, the flow starts to separate.

Fig. 4.47 shows the skin friction lines and marked in blue areas with negative skin friction coefficient on the suction side of the vertical tail. The sign of the skin friction coefficient is taken from the x -component. At $C_f = 0$ the boundary layer profile has a vertical tangent, indicating flow separation. This is usually followed by areas with reversed flow, i.e. with $C_f < 0$. Due to the high rudder deflection of 30° , this is true for large parts of the rudder as shown in Fig. 4.47(a) already for the case with zero sideslip angle. The skin friction lines on the fin are approximately parallel to the onflow direction. On most of the rudder they are turned towards the tip and run approximately in z -direction. This results since the chordwise flow component is decelerated and has reduced to almost zero so that the spanwise component of the flow velocity due to the large sweep angle prevails. Would only the streamlines be considered it might appear as if the flow characteristics are relatively uniform over the whole span of the rudder.

However, looking at the surface pressure distributions in Fig. 4.48 shows that the characteristic rudder shoulder suction peak of a deflected control surface with the dark red color can be found in the lower part of the vertical tail but not in the upper part. The reason for this can be derived from Fig. 4.49, where the extent of the separation into the flow field is visualized by the Mach numbers below the onset flow Mach number of 0.16, and from Fig. 4.50 which shows the field streamlines over the suction side of the VTP. The outer flow coming from the fin is passing above this low velocity region when moving downstream. The recirculation area over the rudder is rather thin in the lower part of the VTP, increasing considerably in thickness at approximately 50% of the span. For the flow coming from the fin the separation area on the rudder has an effect which is

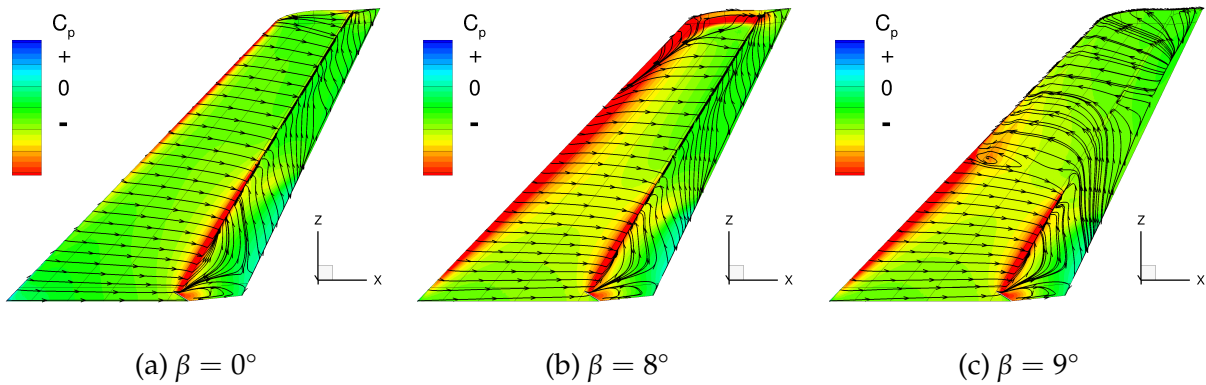


Fig. 4.48 Surface pressure coefficient and skin friction lines, baseline configuration, suction side

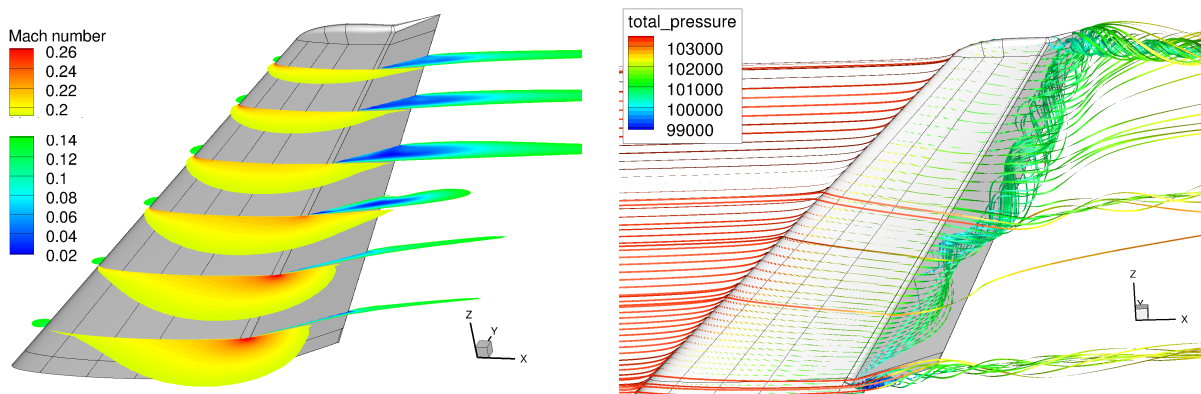


Fig. 4.49 Field slices along the VTP span colored with Mach number, baseline configuration, $\beta = 0^\circ$

Fig. 4.50 Field streamlines, baseline configuration, $\beta = 0^\circ$

similar to a thickening of the geometry itself. The outer border of the recirculation area is now relevant over which the flow coming from the fin is passing. Since the separation is thin in the lower part of the VTP, it only reduces the flow turning angle induced by the rudder deflection a bit. The remaining flow deflection is sufficient to generate the strong suction peak at the rudder shoulder.

In the upper half of the rudder the size of the separation area normal to the rudder surface increases. Due to this, the turning of the flow, which would normally be induced by the rudder deflection, decreases now to almost zero, leading to the absence of the rudder shoulder suction peak in Fig. 4.48 in the upper half of the VTP. As a consequence, the field streamlines in Fig. 4.50 pass almost straight over this separation area.

The rather sudden change in the local side force coefficient at about 50% span is accompanied by a corresponding sudden change in circulation and thus in the spanwise load distribution which is shown in Fig. 4.51. This causes the emerging third vortex at this position as seen in Fig. 4.50. Both tip and root vortex develop for similar reasons — due to the equalization of the pressures from the suction and the pressure side of the vertical tail and the corresponding strong change in circulation.

With increasing sideslip angle the fin leading edge suction peak starts to get larger (cf. Fig. 4.48(b)). When the stall of the fin occurs, here at $\beta = 9^\circ$ as depicted in Fig. 4.48(c),

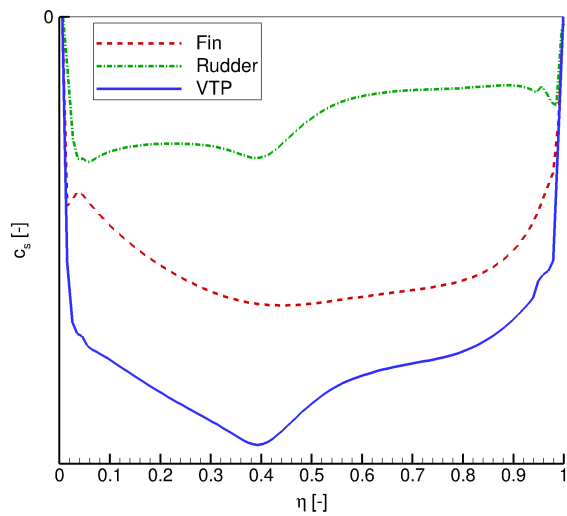


Fig. 4.51 Side force coefficient vs. normalized span coordinate η , baseline configuration, $\beta = 0^\circ$

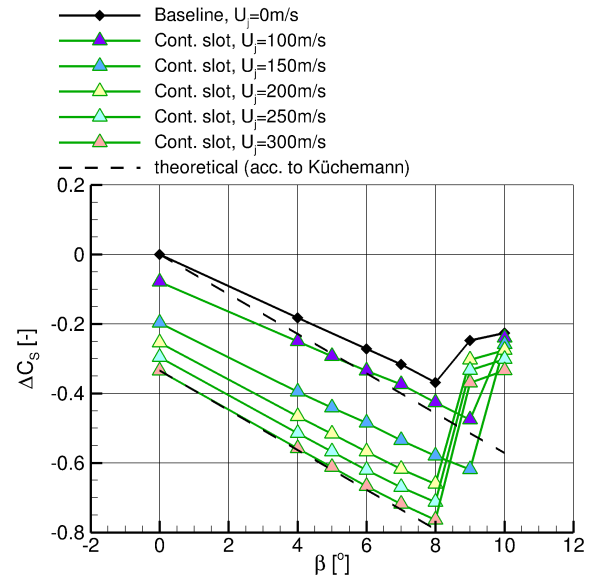


Fig. 4.52 Side force coefficient vs. sideslip angle, 3D VTP, baseline and full span slot with jet velocity variation; dashed lines: theoretical lift curve slope according to Küchemann [99] (Eq. 111)

this suction peak at the leading edge vanishes like for the rudder in the region with a thick recirculation area, accompanied by a drop in C_S . The behavior of the side force coefficient over the sideslip angle in Fig. 4.52 is similar to that of a wing where C_S increases approximately linear with increasing sideslip angle up to the stall.

The flow field characteristics just described give an impression about the complexity of the baseline flow which shall now be influenced and improved by tangential blowing.

4.3.2 Continuous Slot

Applying tangential blowing at the end of the fin with a full span slot can increase the side force coefficient in the linear range. The larger the jet velocity, the larger is the increase in C_S as shown in Fig. 4.52. With sufficient blowing the flow on the rudder remains completely attached. The drop in C_S is also caused by a leading edge stall of the fin. This is shown in Fig. 4.53 by means of the skin friction coefficient and in Fig. 4.54 through the surface pressure coefficient exemplarily for a jet velocity of 200 m/s. In the latter figure it can also be seen that not only the rudder shoulder suction peak has increased due to the effects of blowing but also the fin leading edge suction peak resulting from an upstream effect since in subsonic flow information is propagated in all directions. The skin friction lines on the rudder are approximately perpendicular to the rudder hinge line and thus parallel to the jet blowing direction. Even after the fin has stalled the jet blowing with 200 m/s can keep the flow on most of the rudder attached. For even higher jet velocities, the rudder would be fully attached. Before stall at $\beta = 8^\circ$ the separated area at the fin leading edge at the tip in Fig. 4.53(b) is a bit increased compared to the case without blowing in Fig. 4.47(b). Due to the increase

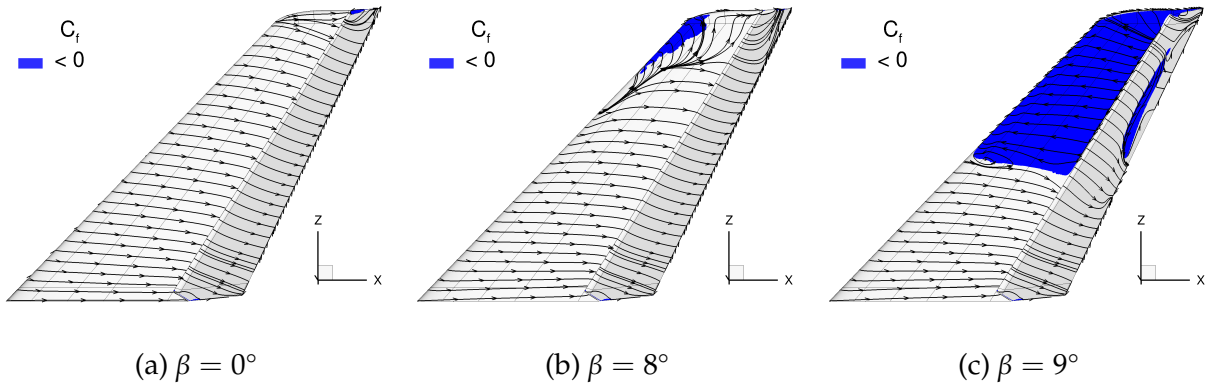


Fig. 4.53 Areas with negative skin friction coefficient (blue) and skin friction lines, full span slot configuration, $U_j = 200$ m/s, suction side

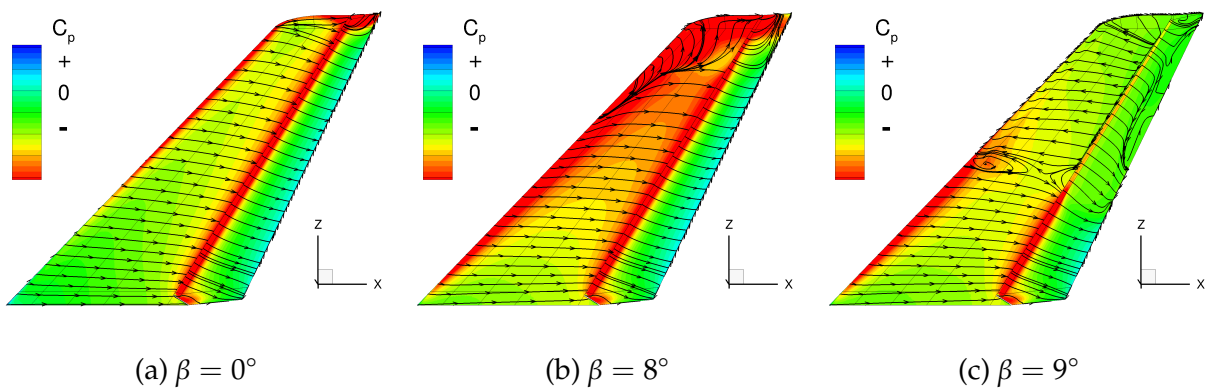


Fig. 4.54 Surface pressure coefficient and skin friction lines, full span slot configuration, $U_j = 200$ m/s, suction side

in the suction peak with blowing active the fin is higher loaded and tends to start separating at a smaller sideslip angle. An increase in the stall angle can be observed for low blowing velocities. This shift in the stall sideslip angle by 1° is equal to the sideslip angle increment used between the data points computed and thus is likely not significant.

Comparing the curve for the baseline configuration and the ones with blowing in Fig. 4.52 it can be observed that the gradients $\delta C_S / \delta \beta$ differ. The gradient increases in principle with increasing blowing velocity. This is due to the change in the separated flow areas. The larger the blowing, the more of the VTP surface features attached flow. That in turn means that a larger percentage of the overall area of the vertical tail can contribute to its full capacity to the side force generation. In the linear range the percentage of separated flow on the VTP is in principle characteristic for each blowing velocity. In line with this reasoning, the relative increase in side force coefficient per degree increase in sideslip is higher for configurations with a larger area of attached flow, leading to the increased side force gradient.

Two dashed lines were added to this diagram: one starting at $\beta = 0^\circ$ and the C_S of the baseline case without blowing and one at $\beta = 0^\circ$ and the C_S of the result for the largest blowing velocity. These curves are parallel to each other and represent the theoretical lift curve slopes as expected for subsonic compressible flow of low-aspect ratio swept wings

according to a formula derived by D. Küchemann ([99], Eq. 111). This theoretical result is valid for lifting surfaces with fully attached flow. Since for the baseline configuration quite some areas of separated flow are present on the rudder, only a significantly smaller gradient can be achieved. For the case with the highest blowing velocity the theoretical expectation and the simulation result coincide for smaller sideslip angles. Here no separation areas are present on the VTP. For larger β the gradient reduces a bit compared to the one expected from the analytical derivation. This is caused by the appearance of a small separation area at the tip of the fin leading edge which already starts to develop at $\beta = 5^\circ$.

4.3.3 Discrete Slots

Instead of a continuous full span slot now discrete slots are used, similar to what was done in the 2.5D investigation. For constant jet velocity the momentum coefficient and the mass flow rate are reduced since the slot area is reduced. The configuration selected is the efficient four-slot configuration from the 2.5D investigation with rounded values for the slot width of $w = 10$ mm and for the gap between the slots of $g = 30$ mm. In total 24 slots are placed along the span. The interaction of the jets with the outer flow is in principle the same as described in Sec. 4.2.2 for the 2.5D investigation. Slices showing the x -component of the vorticity ω_x are depicted in Fig. 4.55. Due to the angle of the incoming flow in relation to the jet blowing direction and the shearing between these two, a vortex pair is created at each jet. The blue vortices with negative ω_x are rotating clockwise about the x -axis and the red ones counter-clockwise. This vortex pair helps to attach the flow not only in the path of the jet itself but also between the jets by enhancing the mixing with the higher-energy outer flow. In the lower part of the rudder the vortices are regular while they get larger and more irregular in the upper part towards the tip. Here the flow is weaker so that the blowing is not sufficient to keep the flow completely attached on the rudder. In addition to adding momentum and enhancing the mixing, the jets also act similar to a boundary layer fence or fluidic fence reducing the spanwise flow.

The phenomena described can also be observed in Fig. 4.56 where already for $\beta = 0^\circ$ some areas of separation can be found in the upper part of the rudder, increasing somewhat with growing sideslip angle. The stall mechanism with the leading edge separation causing the whole upper part of the fin to separate stays the same as for the baseline and full span slot configuration. Comparing the surface pressure coefficient distributions in Fig. 4.57 for the different sideslip angles with those of the full span slot in Fig. 4.54 shows that the rudder shoulder suction peak as well as the one at the fin leading edge are weaker and have a smaller extent in chordwise direction. This is especially true for the area close to the rudder shoulder where separation occurs locally.

From the figures just discussed a lower increase in the side force coefficient is expected than for the continuous slot configuration. This is confirmed in Fig. 4.58 where the discrete jets with $w = 10$ mm can achieve only about 60% of the side force coefficient increase of the continuous slot at the same jet velocity of $U_j = 200$ m/s. The gain in C_S remains smaller even if the jet velocity is increased from $U_j = 200$ m/s to $U_j = 300$ m/s due to the still existing areas of separated flow in the upper region of the rudder. Furthermore, it can be observed for the discrete slots with the smaller jet velocity that the gradient of the curve reduces for intermediate sideslip angles. This is also true if a

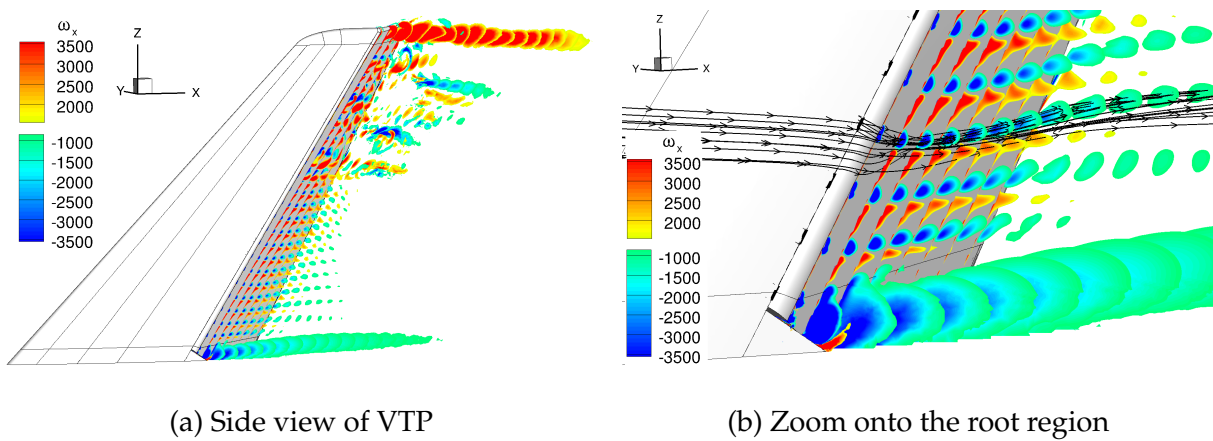


Fig. 4.55 Field slices showing the vortices over the rudder, discrete slots at the 3D VTP, $U_j = 200$ m/s

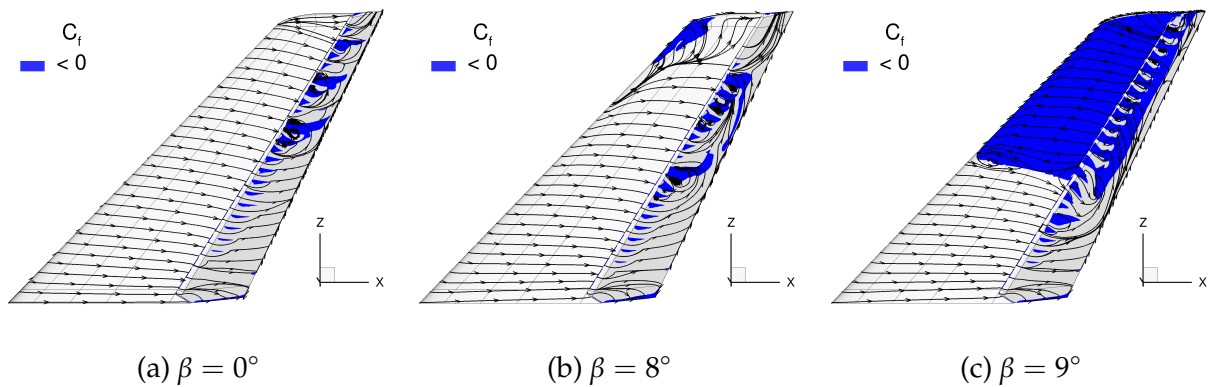


Fig. 4.56 Areas with negative skin friction coefficient (blue) and skin friction lines, discrete slot configuration, $U_j = 200$ m/s, suction side

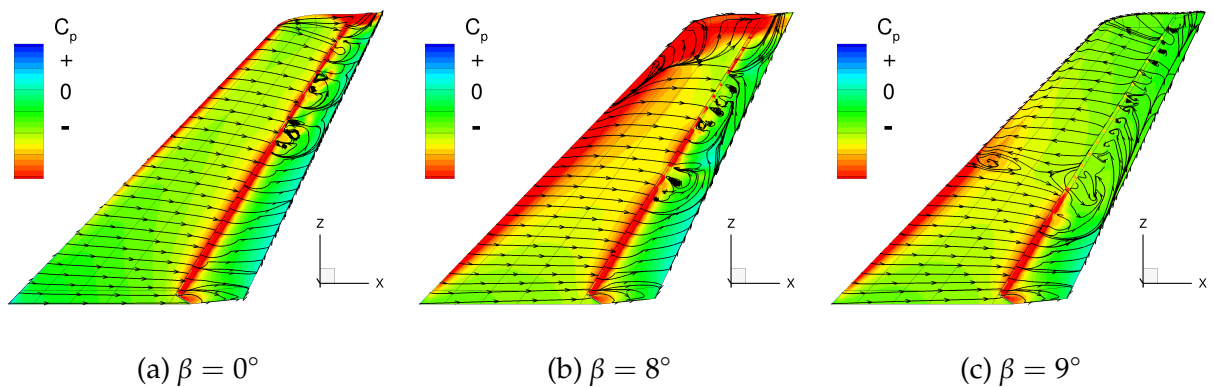


Fig. 4.57 Surface pressure coefficient and skin friction lines, discrete slot configuration, $U_j = 200$ m/s, suction side

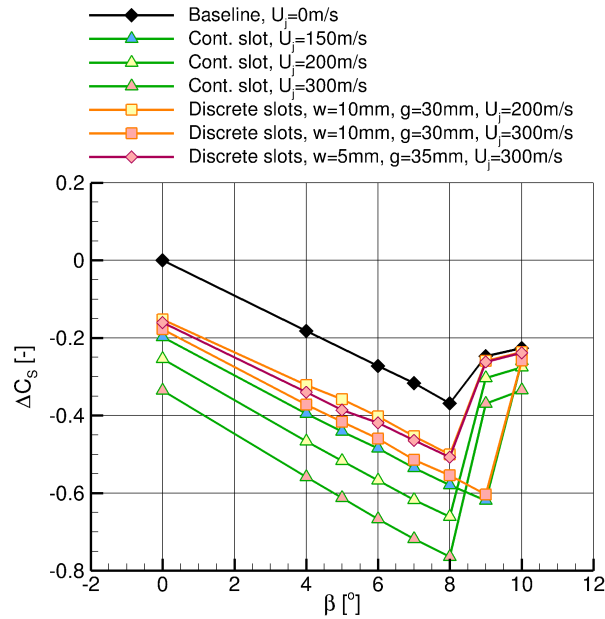


Fig. 4.58 Side force coefficient versus sideslip angle, 3D VTP, baseline, full span slot and discrete slots with jet velocity variation

higher jet velocity but halved slot length is used where the momentum added to the flow on the rudder is a bit higher. From this it becomes apparent that the performance of the slots does not only need to be investigated at zero sideslip angle but also at higher angles in the range which is important for the OEI maneuver.

In Fig. 4.59 the pressure coefficient distributions in six spanwise sections are presented. Here the discrete slot configuration with $w = 10$ mm and $U_j = 300$ m/s is compared to the continuous slot results at $U_j = 150$ m/s which leads to a similar but slightly higher C_s (cf. Fig. 4.58). For comparison also the baseline configuration without blowing is shown. At the section close to the root, where even without blowing only very limited areas of separated flow exist, the effect of blowing on the pressure coefficient distribution is small. Progressing to sections further along the span, the effect of the blowing becomes more obvious. The rudder shoulder suction peak increases significantly, reducing also the pressure level on the fin suction side and increasing the fin leading edge suction peak. Here the continuous slot is more effective, especially in the upper three sections. In the fourth section at $\eta = 0.65$, no slot is present in the direct vicinity for the discrete slot configuration, leading to the relatively large (local) reduction of the rudder shoulder suction peak. Nevertheless, the effect of the blowing is still visible, especially on the rudder where the discrete jets lead to a higher level of negative pressure than the continuous slot, showing the potential of the discrete slots and their benefit with the creation of the vortex system over the rudder enhancing the mixing of the flow.

In addition to the initial discrete slot configuration with $w = 10$ mm and $g = 30$ mm three more were investigated. Since the distribution of the vortex pairs in Fig. 4.55 seems already sufficiently dense, a wider spacing or reduced slot length and with this a reduction in the required mass flow rate is examined. The first of the additional configurations with halved slot length $w = 5$ mm and $g = 35$ mm was already mentioned. For a second configuration each second jet was deactivated leading to $w = 10$ mm and $g = 70$ mm. Starting from this configuration, a third one was derived by doubling the slot width to $w = 20$ mm but also the gap size to $g = 140$ mm so that the mass flow

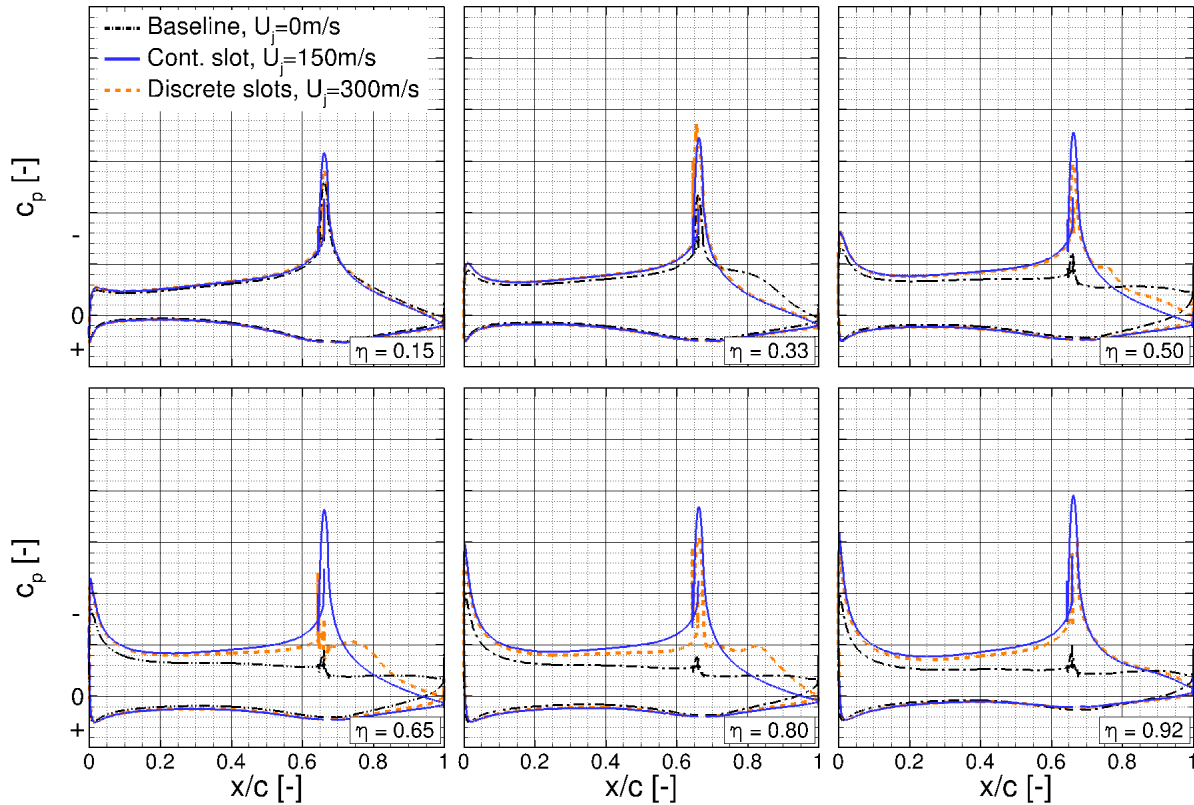


Fig. 4.59 Pressure coefficient distribution in six sections along the span, 3D VTP, baseline, full span slot and discrete slots with $w = 10$ mm, $\beta = 0^\circ$

rate stays about the same and the effect of large but less densely spaced slots can be examined. All configurations with a reduced number of slots or slot length exhibit a reduced gradient of C_S versus β at higher sideslip angles.

These configurations will be compared in Fig. 4.60 at two exemplary sideslip angles, $\beta = 0^\circ$ and the angle before stall $\beta = 8^\circ$, with regard to the momentum coefficient. For each curve the jet velocity increases with increasing C_μ . At $C_\mu = 0$ the result for the baseline configuration without blowing is obtained. For small momentum coefficients all discrete slot configurations are superior to the continuous full span slot, generating a larger side force for the same C_μ . However, at approximately $C_\mu = 0.0045$ most discrete slot configurations are already blowing with a very high jet velocity of $U_j = 300$ m/s — the speed of sound at a temperature of 30°C is 349 m/s. In this C_μ -region the discrete slot configurations approximately double the gain in C_S for $\beta = 0^\circ$. Here only the discrete slot configuration with $w = 10$ mm and $N = 24$ is blowing with merely $U_j = 200$ m/s. Increasing the jet velocity to $U_j = 300$ m/s leads to approximately $C_\mu = 0.009$. The side force coefficient obtained there for the discrete slot configuration is close but a bit smaller compared to the continuous slot with $U_j = 150$ m/s. Since this jet velocity for the continuous slot is still relatively small it can be increased further and shows a large increase in the side force coefficient at $U_j = 300$ m/s or $C_\mu = 0.035$, but also needs about four times the momentum coefficient. This is in principle similar when looking at the higher sideslip angle of $\beta = 8^\circ$. At $C_\mu = 0.0021$ the discrete slots with the large slot length of $w = 20$ mm create the largest increase in ΔC_S relative to the other configurations. This configuration now generates about the same ΔC_S as the other discrete slot configurations at around $C_\mu = 0.0045$ by concentrating its momentum input

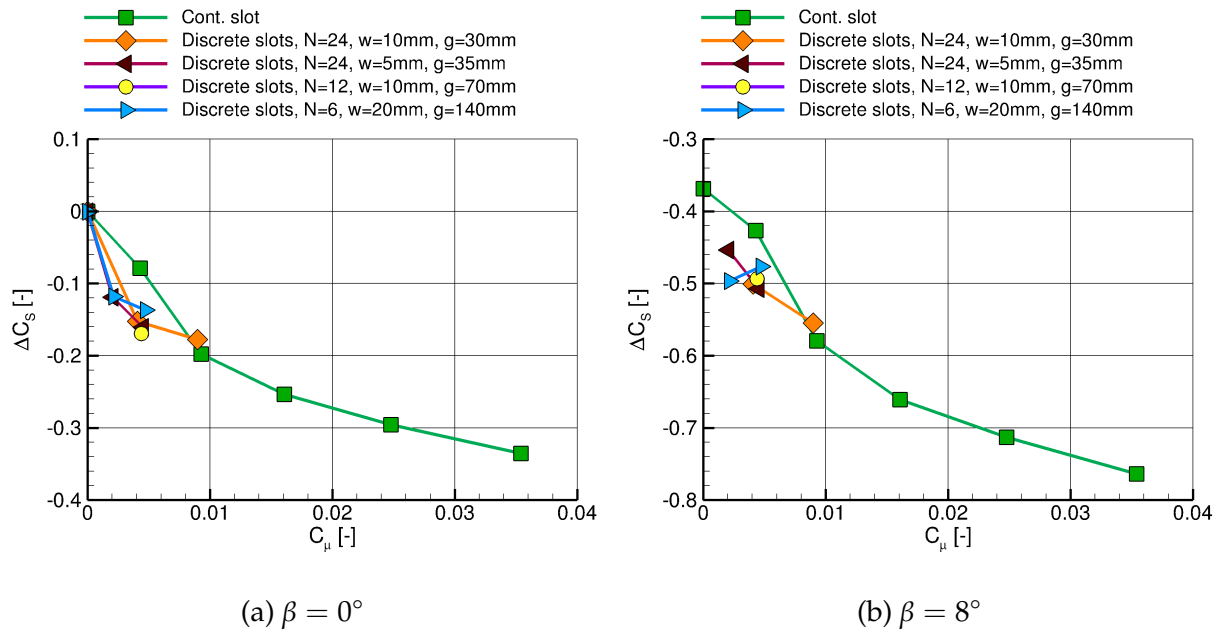


Fig. 4.60 Side force coefficient versus momentum coefficient for the full span slot and the discrete slots configurations for the 3D VTP

in fewer but larger jets. But at approximately $C_{\mu} = 0.0045$ the increase in C_S possible with this configuration is already reduced due to increasing separations. Comparing the results for the discrete slots at a momentum coefficient of about 0.0045, it seems that more but a bit smaller slots are slightly advantageous. However, since they don't have the potential for a significant increase in ΔC_S , a larger slot width might be favored for an actual application.

In Fig. 4.61 the same results are now plotted versus the mass flow coefficient for the same two sideslip angles. The mass flow rate is an important parameter since the airflow has to be provided by some means and the more is required, the more difficult this becomes. The diagrams again show the potential of the discrete slots by reducing the required mass flow rate considerably for about the same increase in side force coefficient. For the encircled points the discrete slot configuration with $w = 10$ mm only needs about half the mass flow rate of the full span slot. While almost the same C_S could also be obtained at $\beta = 0^\circ$ by the discrete slot configuration with $w = 10$ mm but each second slot turned off ($N = 12$), this configuration leads to a much reduced side force coefficient at $\beta = 8^\circ$ in comparison. This means that if a reduction in the mass flow rate is considered more important, the discrete slot configuration with $w = 10$ mm and $N = 24$ would be favored. This, however, just holds if the obtained increase in the side force coefficient is sufficient. Otherwise, the full span slot would also need to be taken into account.

When comparing the savings in the mass flow coefficient with those of the 2.5D investigation for the case where the full span slot has a C_m of about 0.002, it is found that they are reduced for the 3D geometry. For the 2.5D configuration a reduction of 65% could be achieved while it is only about 50% for the 3D VTP when comparing it to the full-span slot with the same C_S . However, a direct comparison of the achieved increase is difficult. The baseline flow for the 2.5D geometry is worse with a fully separated rudder while the flow field on the rudder of the 3D vertical tail is not that uniform and

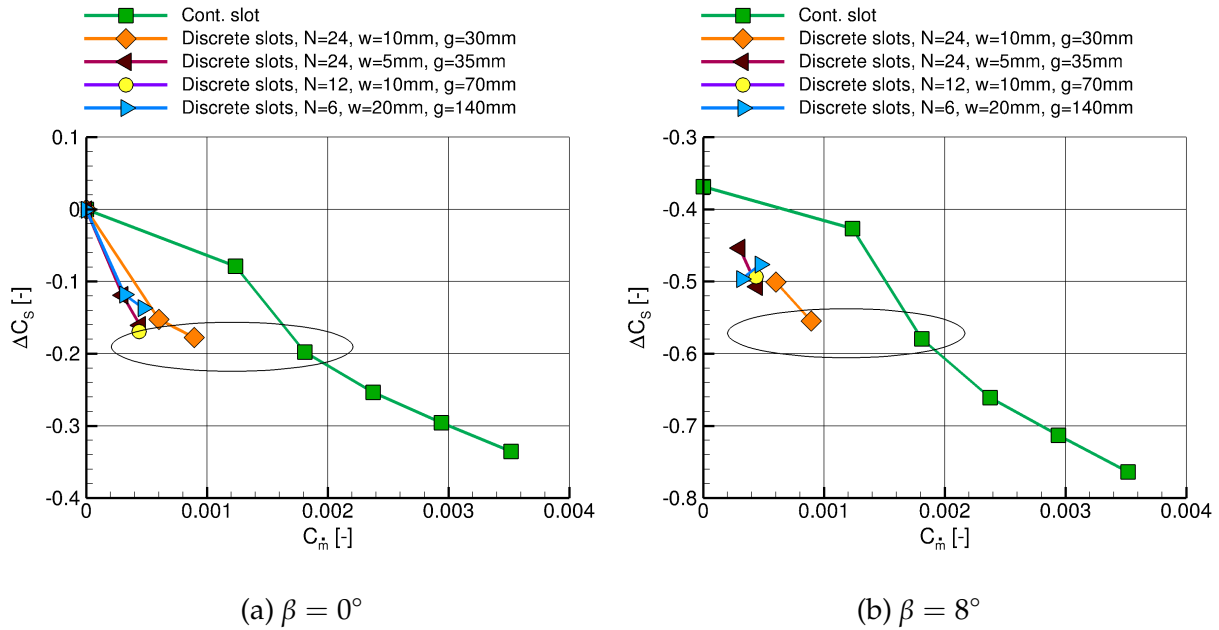


Fig. 4.61 Side force coefficient versus mass flow coefficient for the full span slot and the discrete slots configurations for the 3D VTP

also not fully separated. The worse baseline in 2.5D makes it easier to reach a specific increase when the actuation is active. Due to the root and tip vortex in 3D also not the whole span can be influenced in the same uniform manner as for the 2.5D geometry. This shows that investigations in 2.5D can support the design process with correct and important tendencies but the highly three-dimensional flow on the 3D configuration makes an assessment of the real geometry mandatory for robust and reliable results.

4.3.4 Summary

Lessons learned from the 2D and 2.5D investigations for an efficient tangential blowing design were applied to a 3D vertical tail. The effects on the flow field observed due to the introduction of the discrete slots are similar to the 2.5D design. The creation of the vortex system at each jet of a discrete slot leads to a larger increase in the side force coefficient per invested momentum coefficient or mass flow rate than if using a continuous slot. However, as for the 2.5D results, the maximum achievable side force coefficient is limited if the jet velocity is limited by the speed of sound. The continuous slot on the other hand only needs relatively small jet velocities for similar gains in the side force coefficient compared to the discrete slots since the slot area is considerably larger. By increasing the jet velocity further relatively high gains in the side force coefficient can be achieved at the cost of high momentum and mass flow coefficients.

The efficient four-slot configuration derived from the 2.5D investigation also leads to good results on the 3D VTP. From the configurations tested it gave a good increase in the side force coefficient also at higher sideslip angles. Reducing the slot length with the aim to reduce the mass flow requirement further resulted in decreased performance at a higher sideslip angle.

It could be shown that the design approach from 2D, over 2.5D to 3D for a more efficient

tangential blowing slot configuration generates the understanding and insight required for the design of the AFC system. A significant reduction in the required mass flow rate, a critical parameter for the design of the overall system, can be achieved using discrete slots with a well-defined layout instead of a continuous slot.

Due to 3D effects with strong crossflow on the rudder the weakened and separated flow on the upper part of the vertical tail could not be completely removed with discrete slots. On the other hand the principle behind their effectiveness observed in 2.5D was found to work well in the lower part of the 3D VTP. To further increase the side force, one possibility could therefore be to use discrete slots in the lower part of the vertical tail and a continuous slot in the upper part. This would make the design a bit less efficient but more effective and might be a suitable compromise depending on the design target.

5 Conclusion

This work is built around the flow at the vertical tail(plane) (VTP) of a typical jet-powered transport aircraft which results from the sizing case for the area of the VTP, the one engine inoperative (OEI) maneuver, which is for modern transport aircraft dominating over the area requirement for directional stability. When loaded, the VTP with its large sweep angle and low aspect ratio compared to a wing features a more three-dimensional flow field than known from the latter. During the OEI maneuver, the rudder of the vertical tail is highly deflected, with a representative rudder deflection angle of 30° used in this work. This leads to flow separation on the rudder already at zero sideslip angle. For an actual OEI occurrence in flight, this is usually accompanied by a certain degree of bank and sideslip to help balance the moment due to one engine being inoperative. For the VTP, this additional sideslip angle leads to an increase in the flow separations on the rudder and thus to an increase of the already strong three-dimensional flow behavior with large spanwise velocity components. Based on the understanding of the flow around the VTP just described, the aim of this work is to delay these flow separations by using active flow control. Here, tangential blowing with blowing slots positioned at the end of the fin is selected. It was already shown for other applications that this kind of flow control is capable to achieve the goal specified. However, while tangential blowing is known to be very effective, it is also considered not to be very efficient in accomplishing its task. Therefore different possibilities were investigated on how the efficiency of the tangential blowing approach could be increased without detrimentally affecting the gain in the side force coefficient. To achieve this, a numerical study was conducted and a design for the tangential blowing slots developed, which is both effective and efficient.

The investigation was started with a 2D section of the 3D VTP, mainly used to analyze the effects of geometry changes in the vicinity of the slot. This comprises among other parameters the slot height, the slot angle and the effect of introducing a step from the slot to the rudder shoulder.

The results from the 2D study were then transferred to a 2.5D investigation, where a constant chord geometry with extension in spanwise direction is used. This allows accounting for the large sweep angle of the VTP and opens the possibility to examine apart from a continuous full span slot also discrete slots with a variation of slot and gap width. In addition, the influence of a variation of the velocity of the constant blowing jet is examined. Due to periodic boundaries placed on both sides of this VTP section this corresponds in the simulation to a wing with infinite span. When replacing the full span slot with discrete slots it was observed that the discrete slots lead to the creation of a vortex system over the rudder which helps to attach the flow not only in the path of the jet but also in between the jets in spanwise direction. Thus, not only the momentum of the jets themselves is used but also the beneficial mixing with the outer flow caused

by the vortices. Since the overall extent of the slots in spanwise direction is reduced, a part of the mass flow can be saved. With the use of discrete slots the required mass flow rate and momentum coefficient could be reduced by up to 65% for about the same increase in side force coefficient.

In a last step the outcome from the previous investigations was applied to the full 3D vertical tail with its very three-dimensional flow field. The best discrete slot configuration from the 2.5D study was used, complemented by a few additional variations concerning the slot arrangement. The results show that the best 2.5D slot configuration also performs best on the 3D VTP among all configurations tested. However, the savings in the mass flow rate are smaller than for the 2.5D investigations but at around 50% still significant compared to a full span slot. Depending on the specified design goal the maximum achievable side force coefficient might be a limitation when using discrete slots. If the jet velocity cannot be increased beyond the speed of sound, there is also a natural limit to the side force increment which can be achieved. With increasing side force requirement, the slot width has to be extended more and more at the expense of a reduced efficiency with the full span slot being the upper limit.

As part of the study it was also examined if the efficiency can be increased even further by pulsed blowing using a fixed duty cycle of 0.5. This had led to very promising results for the 2D geometry. For the 2.5D geometry it is still more efficient than constant blowing, but the range of application was limited to rather low gains in the side force coefficient. Thus, pulsed blowing was not further pursued for the 3D geometry. A more comprehensive investigation might be needed to assess the full potential of this kind of blowing. A variation of parameters like duty cycle or frequency could improve the results. In addition, only the slot spacing from the constant blowing approach was used but a spacing optimized for the unsteady pulsed blowing might be more beneficial.

Comparison with Other Research Results

With respect to the work presented especially two points are of interest for comparison with other research results: first, is the baseline flow captured correctly, i.e. does the reference used make sense; and second, how does the efficiency of the AFC system compare to other active flow control methods. While it was shown that the efficiency can be significantly increased using discrete slots, only a comparison to alternative flow control methods is going to reveal if these improvements are sufficient for tangential blowing to be competitive for an actual application.

Concerning the baseline flow without flow control the wind tunnel investigation carried out on the same VTP geometry and described by Scholz et al. in [59] has shown a good agreement of the flow behavior up to the stall compared to the numerical results obtained for the present work. Some of these results were also discussed in Ch. 3. The biggest difference between wind tunnel test and CFD results was found to be the stall characteristics. In the wind tunnel test no abrupt stall was observed for the baseline configuration. The reason for this difference could not be explained conclusively, but deficiencies in the numerical modeling especially related to the turbulence model are likely. Other numerical studies in publicly available literature investigating this behavior and using a vertical tail-type geometry are rare. Besides the one mentioned above, a detailed study by Shmilovich et al. [63] was found. There, the results of a numerical study on a wind tunnel and flight-tested configuration with sweeping jets on the VTP

at the same rudder deflection angle were presented (note opposite sign convention for the sideslip angle compared to this work). The CFD results of Shmilovich for the flow without AFC show a good topological and qualitative agreement in the linear range of the side force coefficient vs. sideslip angle curve as well as in the range of the maximum sideslip angle with the results obtained for this work, judging from surface C_p and field total pressure visualizations. The curve for the side force coefficient C_S versus sideslip angle β is also similar (cp. Fig. 4.52 with [63], Fig. 13). The maximum side force coefficient for the isolated VTP investigated by Shmilovich et al. was found at already $\beta = -5^\circ$, which is a bit earlier but might be attributed to the characteristics of the Boeing 757 vertical tail geometry and the fact that CFD results are only available in 5° increments between $\beta = +5^\circ$ and $\beta = -10^\circ$. While there is a drop in C_S for the isolated VTP when increasing the sideslip angle beyond that, the side force coefficient only levels out for the full aircraft configuration. The surface pressure coefficient distributions presented for the baseline configuration exhibit all features found for the vertical tail in this work as well. Furthermore, in a study by Jansen et al. [66] a vertical tail-like geometry is found where the baseline flow without sideslip angle at the same 30° rudder deflection angle as in this work is discussed. A computationally expensive delayed detached-eddy simulation was performed and just the one sideslip angle is available. The results were validated with a dedicated small-scale experiment which conditions were met as good as possible. Despite the bit larger aspect ratio planform and a different construction in the root region at the transition of the fin to the rudder, the flow field looks quite similar giving also the three characteristic vortices at root, tip and one in between. In summary, the flow around the baseline configuration seems to be captured in a representative manner up to the maximum side force coefficient and thus in the region of interest.

When comparing with other results using active flow control, two investigations are particularly interesting. The first study, already mentioned above in the discussion of the baseline flow, examined the same VTP geometry at the same scale as in this work but also investigated alternative actuation methods allowing a direct comparison of achievable side force increments. The second study was carried out also quite recently in the frame of the NASA Environmentally Responsible Aviation (ERA) project and used vertical tail-like geometries. One result of this study was already described above. Over several years multiple investigations were performed ranging from small-scale wind tunnel tests to a full-scale wind tunnel test and finally a flight test. Here sweeping jets, i.e. another type of active flow control actuators, were used. A lot of data is available from these studies, but no absolute values were ever given. Also, some relevant details of geometry and test setup are not known, but the application case and the rudder deflection angle considered are very similar to what is used in this work. As explained before, the flow characteristics of a vertical tail are a bit different compared to a usual higher aspect-ratio wing-type use case for flow control, making a direct comparison with such results difficult.

Results of the first study, done for three different actuation methods by three partners, was summarized by Scholz et al. [59]. One method is tangential blowing including the discrete slots which are treated in the current work. The two other methods are vortex generating jets (VGJ) and pulsed blowing jets where neighboring slots are blowing alternately. VGJ are much more efficient, i.e. they require less momentum coefficient for the same side force increase, but only much smaller increases in the side force coefficient are possible. This might limit their field of application. Compared to pulsed blowing,

where the actuators have an angle to the surface, tangential blowing leads to a similar gain in side force with respect to the required momentum coefficient C_μ in the region of linear side force increase. For the maximum side force increase before stall this gain in side force with respect to C_μ is partly even larger for medium to large momentum coefficients. This means that tangential blowing is comparable to the pulsed blowing approach described in [57] in terms of results, but since no pulsing is required the actuation system might be simpler, lighter and/or smaller, making its integration easier.

Results of the second study driven by NASA and Boeing where especially sweeping jets were considered and investigated are for example summarized in [33, 53]. In the beginning also synthetic jets were examined, but due to the low jet exit velocity the side force enhancement was considered too limited. Thus, the sweeping jets were selected to go forward. They combine sweeping, which allows them to cover a relatively large range in spanwise direction, with tangential injection of momentum into the flow. The largest amount of data is available for the configuration with sweeping jets used in the full scale wind tunnel test. For the same 20% increase in side force coefficient at $\beta = 0^\circ$ this approach requires about 39% less C_μ than the discrete tangential blowing jets in this work and about 32% less C_μ at $\beta = 7.5^\circ$. The values for the discrete slots at $\beta = 7.5^\circ$ are estimated from an interpolation between the results at 7° and 8° sideslip angle. The effect of the cut-outs for the rudder support mechanism examined in [49] is already accounted for in the values for the comparison. The cut-outs are present at the real full scale vertical tail but not in the current investigation. They lead to a reduced side force capability of the reference configuration without blowing, making it easier to reach the targeted 20% increase in the side force coefficient.

However, there are some differences in the setup which are not accounted for but have an effect on the compared C_μ or side force values. The freestream velocity of the NASA/Boeing investigation is with 51 m/s smaller than in the current study with 57 m/s. For the same jet velocity this would reduce the ratio of jet to freestream velocity, reducing in turn the effect of blowing in the results of this work. The momentum coefficient, which is one measure of the effectiveness of the actuation, is a function of $1/M_\infty^2$. For the same input to the actuators, e.g. the same pressure resulting in the same jet velocity, this would imply a reduction in the actuation effectiveness for the discrete slot investigation by about 17%. Also it has to be taken into account that the model scale differs by approximately one order of magnitude. However, this was found not to be a major driver in the NASA/Boeing investigations. The momentum coefficient required to achieve a specified increase in the side force coefficient in a sub-scale test was about the same as in the full-scale test [49]. Furthermore, it has to be considered that the sweeping jet configuration has already seen some optimization. Removing the two top slots of the discrete slot configuration, which were shown to have no significant impact, would reduce the required C_μ by about 0.05%. That would correspond to a reduction of about 5% in the above mentioned levels of C_μ compared to the NASA/Boeing results. In the end, the difference between both methods might be smaller than the current values suggest. Nevertheless, the sweeping jets are quite efficient due to their sweeping motion and their ability to cover about twice the spanwise extent as a normal steady blowing jet [100]. Thus, the discrete slots might not reach the same efficiency.

However, there is one result from the small-scale wind tunnel investigations with sweeping jets described in [9] (Fig. 9) which could be interpreted in such a way that steady discrete blowing jets in an appropriate setup can be comparable or even

more efficient than sweeping jets for low momentum coefficients. In the sweeping jet investigation one feedback loop of the sweeping jet actuators was blocked, effectively creating a steady jet. This led to one configuration where the jets were inclined to one (extreme) side of the exit nozzle with the jet blowing direction being upward and a second configuration where the jets were pointing downwards. The jets pointing downward, i.e. those with a larger angle to the freestream flow direction, were much more effective. This also corresponds to the findings in the work presented here. Comparing at constant C_{μ} , the same configuration but with sweeping jets had a side force gain in between the two configurations with the steady jet directed upward and downward. At least for this case at 30° rudder deflection and the relatively large spacing between the actuators used there, the steady jets with the appropriate blowing direction were found to be superior to the sweeping jets up to $C_{\mu} = 0.7\%$ which is still inside the area of interest. A direct comparison between sweeping jets and discrete steady jets for the same flow conditions and if possible also with the same geometry would thus be very interesting.

Whalen et al. concluded in [52] that based on the flight test results and scaled extrapolations, an increase in rudder effectiveness of about 14% can be achieved at 30° rudder deflection angle and at relevant sideslip angles up to 7.5° for the maximum mass flow rate possible in this test. This would allow an area reduction of the vertical tail by approximately 12% [53]. With the 14% increase in rudder effectiveness obtained, the value of 20% initially targeted and achieved in the full-scale wind tunnel test was not reached. Thus, when considering the full aircraft system including all components like fuselage, wing and horizontal stabilizer, the expected side force gains might be reduced for the real application in the end compared to an isolated vertical tail in the wind tunnel. This has also to be taken into account when looking at the side force gains from the discrete slots. While a tail area reduction could be achieved using sweeping jets, the vertical tail is just one small part of the aircraft. In an integration study [48] it was concluded that a down-scaling of the VTP by 15% would reduce the total aircraft drag by about 0.4%.

Outlook

Next steps could be a further optimization of the discrete tangential blowing slots from an aerodynamic point of view by improving their adaptation to the 3D configuration. An actuation only in the mid-span region for example leads to an increased efficiency (e.g. [58]) but at the same time also to a reduction in the side force gain possible. At about this mid-span position the C_p -peak at the rudder shoulder ends in spanwise direction for the baseline case without blowing, making an actuation at this position especially beneficial. In addition to energizing the flow, the actuation leads to a reduction in the spanwise flow by acting like a fluidic boundary layer fence. Even a single actuator could inhibit this spanwise flow causing effects which can be seen all the way up to the tip. Thus, actuation in this mid-region should maybe be amplified while it could be reduced, e.g. by coarser slot spacing, in the lower part of the vertical tail. Also approaches like a combination of discrete slots in the lower half of the span and a continuous slot in the upper half could be considered. Further optimizations like a variation of the slot width along the span could be investigated or a variation of the jet velocity. If a maximum available mass flow rate would be known from a system development exercise, this could be taken into account as a constraint as well.

Furthermore, the state of the art with regard to actuator technology needs to be monitored. Other types of actuators might emerge which could be coupled with the current concept, e.g. transverse actuation [101], or synthetic jet actuators might be improved further regarding their possible output velocity. At that point it might be worthwhile from a weight, systems integration and/or mass flow requirement perspective to investigate such actuators in combination with discrete slots further.

The results of the small-scale model presented in this work will have to be transferred to a full-scale application case for which it needs to be ensured that the jets have the same effect on the flow. In the sweeping jet investigation by NASA, Boeing and universities, a good scalability of the momentum coefficient and with this also of the sweeping jet actuators themselves was observed when comparing the results to the full scale test [9, 49]. Also other results from the EU project "AFLoNext" for pulsed blowing actuators [34] make it reasonable to assume that the outcome of this work could be successfully transferred to a full-scale application.

Drag reduction in cruise flight is the motivation for this study. This can be achieved if the vertical tail surface can be reduced by creating more side force with a given tail area — if the resulting direct reduction in drag and weight is not compensated by the additional weight required for the actuation system. A study by NASA and Boeing [48] has shown that the change in the vertical tail area is directly proportional to the improvement in side force generation capability of the vertical tail. But the aerodynamic optimization alone is only one part. The design of the system operating the actuators and the actuator design itself need to be further investigated. This was done by NASA and Boeing in the integration study [48] mentioned above where they investigated a vertical tail equipped with sweeping or synthetic jets. Such a study at aircraft level considering detailed information from all disciplines as far as possible would be needed to assess the overall benefit which could be expected from a VTP enhanced with tangentially blowing discrete slots. Handling qualities considerations would need to be taken into account alongside manufacturing costs, weight, system reliability during long term usage as well as environmental aspects like noise. Blowing air through small slots at high velocity is usually quite noisy. But since they are only required in emergency situations this might not be critical. However, the actuators might need to be checked before each flight which would have to be done while limiting noise pollution. For the installation it has also to be taken into account that since the vertical tail is symmetric and the engine failure can occur on both sides, the actuators need to be installed on both sides as well. When needed, the actuators will only be active at the suction side of the vertical tail where they provide aerodynamic benefit. This means that the mass flow required does not increase only because the system is installed on both sides. Another point is that for the case of sudden failure of one engine the rudder needs to be deflected in a very short time period. The actuation system has to be fully operational before the maximum rudder deflection angle is reached where separations are expected to occur. This highlights that demonstrating the aerodynamic benefit of such an AFC system is only the first step. An aircraft manufacturer will not implement such a system only because it is technically brilliant. It needs to bring benefits which can be translated into a monetary benefit for the aircraft operator. Finally, it has to be kept in mind that with the use of active flow control for the critical one-engine inoperative case other cases in the flight envelope might become critical and that any reduction of the vertical tail size might be limited by these.

While the vertical tail was taken as a use case here, other lifting surfaces could benefit from this work as well. If doing so it has kept in mind that the angle of the incoming flow to the blowing direction of discrete jets plays a crucial role. Thus, for lifting surfaces with less sweep the relative position and angle of the jets to the hinge line might need to be adapted.

Bibliography

- [1] The World Bank. *Air Transport, Passengers Carried, with data from the International Civil Aviation Organization, Civil Aviation Statistics of the World and ICAO staff estimates*. URL: <https://data.worldbank.org/indicator/IS.AIR.PSGR>, visited May 1st, 2020.
- [2] Airbus S.A.S. *Global Market Forecast: Cities, Airports & Aircraft 2019–2038*. Airbus S.A.S., Blagnac Cedex, France, 2019.
- [3] Boeing. *Commercial Market Outlook 2019–2038*. Boeing, 2019.
- [4] P. Argüelles, M. Bischoff, P. Busquin, B. A. C. Droste, R. Evans, W. Kröll, J.-L. Lagardère, A. Lina, J. Lumsden, D. Ranque, S. Rasmussen, P. Reutlinger, R. Robins, H. Terho, and A. Wittlöv. *European Aeronautics: A Vision for 2020: Meeting Society's Needs and Winning Global Leadership*. European Commission, 2001.
- [5] European Commision. *Flightpath 2050, Europe's Vision for Aviation*. European Union, Luxembourg, Belgium, 2011.
- [6] H. Hansen. Laminar Flow Technology — The Airbus View. In *Proceedings 27th Congress of the International Council of the Aeronautical Sciences (ICAS)*, Nice, France, 19 – 24 September 2010. ICAS Paper 2010-1.9.4.
- [7] L. Cattafesta and M. Sheplak. Actuators and Sensors. In R. D. Joslin and D. N. Miller, editors, *Fundamentals and Applications of Modern Flow Control*, volume 231 of *Progress in Aeronautics and Astronautics*, pages 149–176. AIAA, 2009.
- [8] T. M. Crittenden, A. Glezer, R. Funk, and D. Parekh. Combustion-Driven Jet Actuators for Flow Control. AIAA Paper 2001-2768, 2001.
- [9] M. Y. Andino, J. C. Lin, R. Seele, E. C. Graff, M. Gharib, E. A. Whalen, and I. J. Wygnanski. Active Flow Control on Vertical Tail Models. *AIAA Journal*, 57(8):3322–3338, 2019.
- [10] P. Poisson-Quinton and L. Lepage. Survey of French research on the control of boundary layer and circulation. In *Boundary Layer and Flow Control. Its Principles and Application*, volume 1, pages 21–73. G. V. Lachmann, Pergamon Press, New York, 1961.
- [11] V. Brunet, J. Dandois, and C. Verbeke. Recent Onera Flow Control Research on High-Lift Configurations. *Journal AerospaceLab, Issue 6, AL06-05*, pages 1–12, 2013.

- [12] R. Radespiel, M. Burnazzi, M. Casper, and P. Scholz. Active Flow Control for High Lift with Steady Blowing. *The Aeronautical Journal*, 120(1223):171–200, 2016.
- [13] V. Ciobaca and J. Wild. Active Flow Control for Aircraft Wings. In S. Lavagnoli, editor, *Active Flow Control: Techniques and Applications*, Lecture Series 2017-04. von Karman Institute for Fluid Dynamics, Rhode St. Genèse, Belgium, 2017.
- [14] M. Bauer, I. Peltzer, W. Nitsche, and B. Gölling. Active Flow Control on an Industry-Relevant Civil Aircraft Half Model. In R. King, editor, *Active Flow Control II*, volume 108 of *Notes on Numerical Fluid Mechanics and Multidisciplinary Design*, pages 95–107. Springer, 2010.
- [15] B. Nishri and I. Wygnanski. Effects of Periodic Excitation on Turbulent Flow Separation from a Flap. *AIAA Journal*, 36(4):547–556, 1998.
- [16] A. Seifert, A. Daraby, B. Nishri, and I. Wygnanski. The Effects of Forced Oscillations on the Performance of Airfoils. AIAA Paper 93–3264, 1993.
- [17] L. Prandtl. Über Flüssigkeitsbewegung bei sehr kleiner Reibung. In *Verh. III Internationaler Mathematiker Kongress*, pages 484–491. Heidelberg, Germany, 1904.
- [18] A. Baumann. Tragflügel für Flugzeuge mit Luftaustrittsöffnungen in der Außenhaut. Deutsches Reichspatent 400806, 1921.
- [19] E. G. Reid and M. J. Bamber. Preliminary Investigation on Boundary Layer Control by Means of Suction and Pressure with the U.S.A. 27 Airfoil. NACA TR 286, National Advisory Committee for Aeronautics, 1928.
- [20] M. Knight and M. J. Bamber. Wind Tunnel Tests on Airfoil Boundary Layer Control Using a Backward Opening Slot. NACA TR 323, National Advisory Committee for Aeronautics, 1929.
- [21] J. N. Nielsen and J. C. Biggers. Recent Progress in Circulation Control Aerodynamics. AIAA Paper 87-0001, 1987.
- [22] V. E. Lockwood, T. T. Turner, and J. M. Riebe. Wind-Tunnel Investigation of Jet-Augmented Flaps on a Rectangular Wing to High Momentum Coefficients. NACA TN 3865, National Advisory Committee for Aeronautics, 1956.
- [23] J. M. Riebe. A Correlation of Two-Dimensional Data on Lift Coefficient Available With Blowing-, Suction-, Slotted-, and Plain-Flap High-Lift Devices. NACA RM L55D29a, National Advisory Committee for Aeronautics, 1955.
- [24] R. J. Englar. Circulation Control for High Lift and Drag Generation on STOL Aircraft. *Journal of Aircraft*, 12(5):457–463, 1975.
- [25] G. K. Korbacher. Aerodynamics of Powered High-Lift Systems. *Annual Review of Fluid Mechanics*, 6:319–358, 1974.
- [26] R. J. Englar. Circulation Control Pneumatic Aerodynamics: Blown Force and Moment Augmentation and Modification; Past, Present and Future. AIAA Paper 2000-2541, 2000.

- [27] A. Seifert, T. Bachar, D. Koss, M. Shepshelovich, and I. Wygnanski. Oscillatory Blowing, a Tool to Delay Boundary Layer Separation. *AIAA Journal*, 31(11):2052–2060, 1993.
- [28] G. S. Jones and R. J. Englar. Advances in Pneumatic-Controlled High-Lift Systems Through Pulsed Blowing. AIAA Paper 2003-3411, 2003.
- [29] M. Bauer, J. Lohse, F. Haucke, and W. Nitsche. High-Lift Performance Investigation of a Two-Element Configuration with a Two-Stage Actuator System. *AIAA Journal*, 52(4):1307–1313, 2014.
- [30] R. Seele, P. Tewes, R. Woszidlo, M. McVeigh, N. Lucas, and I. Wygnanski. Discrete Sweeping Jets as Tools for Improving the Performance of the V-22. *AIAA Journal of Aircraft*, 46(6):2098–2106, 2009.
- [31] E. Graff, R. Seele, J. C. Lin, and I. Wygnansk. Sweeping Jet Actuators — A New Design Tool for High Lift Generation. NASA Technical Report NF1676L-16485, 2013.
- [32] A. Seifert and C. P. Tilmann. Control of Flow Separation for Fixed Wing Airfoil Applications. In *Flow Control: Fundamentals, Advances and Applications*, Lecture Series 2009-02. von Karman Institute for Fluid Dynamics, Rhode St. Genèse, Belgium, 2009.
- [33] J. C. Lin, M. Y. Andino, M. G. Alexander, E. A. Whalen, M. A. Spoor, J. T. Tran, and I. J. Wygnanski. An Overview of Active Flow Control Enhanced Vertical Tail Technology Development. AIAA Paper 2016-0056, 2016.
- [34] P. Schloesser, V. Soudakov, M. Bauer, and J. Wild. Active Separation Control at the Pylon-Wing Junction of a Real-Scale Model. *AIAA Journal*, 57(1):132–141, 2019.
- [35] A. M. Honohan, M. Amitay, and A. Glezer. Aerodynamic Control Using Synthetic Jets. AIAA Paper 2000-2401, 2000.
- [36] T. Van Buren, E. Whalen, and M. Amitay. Achieving a High-Speed and Momentum Synthetic Jet Actuator. *Journal of Aerospace Engineering*, Volume 29, August 2015.
- [37] P. Weigel, M. Schueller, A. Gratiyas, M. Lipowski, T. Meer, and M. Bardet. Design of a Synthetic Jet Actuator for Separation Control. In *Proceedings of the 6th CEAS Air and Space Conference — Aerospace Europe 2017*, Bucharest (Romania), 2017.
- [38] *Proceedings of the 2004 NASA/ONR Circulation Control Workshop*, NASA/CP-2005-213509/PT1 and NASA/CP-2005-213509/PT2. National Aeronautics and Space Administration, NASA Langley Research Center, Langley, Virginia, USA, 2005.
- [39] C. L. Rumsey, T. B. Gatski, W. L. Sellers III., V. N. Vatsa, and S. A. Viken. Summary of the 2004 Computational Fluid Dynamics Validation Workshop on Synthetic Jets. *AIAA Journal*, 44(2):194–207, 2006.
- [40] V. Ciobaca. *Validation of Numerical Simulations for Separation Control on High-Lift Configurations*. PhD thesis, DLR (German Aerospace Center), April 2014.

- [41] R. Seele, E. Graft, M. Gharib, L. Taubert, J. Lin, and I. Wygnanski. Improving Rudder Effectiveness with Sweeping Jet Actuators. AIAA Paper 2012-3244, 2012.
- [42] R. Seele, E. Graft, J. Lin, and I. Wygnanski. Performance Enhancement of a Vertical Tail Model with Sweeping Jet Actuators. AIAA Paper 2013-0411, 2013.
- [43] N. W. Rathay, M. J. Boucher, M. Amitay, and E. Whalen. Performance Enhancement of a Vertical Stabilizer using Synthetic Jet Actuators: Non-zero Sideslip. AIAA Paper 2012-2657, 2012.
- [44] N. W. Rathay, M. J. Boucher, M. Amitay, and E. Whalen. Performance Enhancement of a Vertical Stabilizer using Synthetic Jet Actuators: No Sideslip. AIAA Paper 2012-0071, 2012.
- [45] N. W. Rathay, M. J. Boucher, M. Amitay, and E. Whalen. Performance Enhancement of a Vertical Tail Using Synthetic Jet Actuators. *AIAA Journal*, 52(4):810–820, 2014.
- [46] N. Rathay, M. Boucher, M. Amitay, and E. Whalen. Parametric Study of Synthetic-Jet-Based Control for Performance Enhancement of a Vertical Tail. *AIAA Journal*, 52(11):2440–2454, 2014.
- [47] N. Rathay, M. Amitay, and E. Whalen. Flow Physics Associated with the Performance Enhancement of a Vertical Tail using Synthetic Jet Actuators. AIAA Paper 2013-2797, 2013.
- [48] H. P. Mooney, J. B. Brandt, D. S. Lacy, and E. A. Whalen. AFC-Enabled Vertical Tail System Integration Study. NASA CR 2014-218168, 2014.
- [49] M. Y. Andino, J. C. Lin, A. E. Washburn, E. A. Whalen, E. C. Graff, and I. J. Wygnanski. Flow Separation Control on a Full-Scale Vertical Tail Model using Sweeping Jet Actuators. AIAA Paper 2015-0785, 2015.
- [50] E. A. Whalen, D. Lacy, J. C. Lin, M. Y. Andino, A. E. Washburn, E. C. Graff, and I. J. Wygnanski. Performance Enhancement of a Full-Scale Vertical Tail Equipped with Active Flow Control. AIAA Paper 2015-0784, 2015.
- [51] E. A. Whalen, A. Shmilovich, M. Spoor, J. Tran, P. Vijgen, J. C. Lin, and M. Andino. Flight Test of an AFC Enhanced Vertical Tail. AIAA Paper 2016-3927, 2016.
- [52] E. A. Whalen, A. Shmilovich, M. Spoor, J. Tran, P. Vijgen, J. C. Lin, and M. Andino. Flight Test of an Active Flow Control Enhanced Vertical Tail. *AIAA Journal*, 56(9):3393–3398, 2018.
- [53] J. C. Lin, E. A. Whalen, J. L. Eppink, E. J. Siochi, M. G. Alexander, and M. Y. Andino. Innovative Flow Control Concepts for Drag Reduction. AIAA Paper 2016-0864, 2016.
- [54] M. G. Alexander, F. K. Harris, M. Spoor, S. R. Boyland, T. Farrell, and D. Raines. Active Flow Control (AFC) and Insect Accretion and Mitigation (IAM) System Design and Integration on the Boeing 757 ecoDemonstrator. AIAA Paper 2016-3746, 2016.

- [55] D. Cafarelli, T. Arnold, J. Nippard, A. Kwong, S. Gurung, and M. Jabbal. Performance Enhancement of a Vertical Tail Model with Active Flow Control Technology. In *Proceedings of the Royal Aeronautical Society Conference on Advanced Aero Concepts, Design and Operations*, Bristol, UK, 2014.
- [56] V. M. Singh and P. Scholz. Comparison of Different Vortex Generating Devices for Flow Control on a Vertical Tail. AIAA Paper 2018-4023, 2018.
- [57] S. Löffler, M. Staats, T. Grund, and J. Weiss. Increasing the Effectiveness of a Vertical Stabilizer by Combining Pulsed Jet Actuation at the Leading Edge and the Rudder Hinge Line. AIAA Paper 2018-2845, 2018.
- [58] S. Löffler, S. Rohlf, M. Staats, T. Grund, and J. Weiss. Flow Field Investigation on a Vertical Stabilizer with Pulsed Jet Actuation by Means of PIV Measurements. AIAA Paper 2019-3499, 2019.
- [59] P. Scholz, V. M. Singh, A. Gebhardt, S. Löffler, and J. Weiss. A Comparison of Different Active Flow Control Methods on a Generic Vertical Tail. AIAA Paper 2020-1537, 2020.
- [60] V. N. Vatsa, D. Casalino, J. C. Lin, and J. Appelbaum. Simulation of a High-Lift Configuration Embedded with Fluidic Actuators Using PowerFLOW Code. *International Journal of Flow Control*, 6:147–170, 12 2014.
- [61] R. E. Childs, P. M. Stremel, J. A. Garcia, J. T. Heineck, L. K. Kushner, and B. I. Stormsk. Simulation of Sweep-Jet Flow Control, Single Jet and Full Vertical Tail. AIAA Paper 2016-0569, 2016.
- [62] P. G. Buning, I. T. Chiu, S. Obayash, Y. M. Rizk, and L. Steger J. Numerical Simulation of the Integrated Space Shuttle Vehicle in Ascent. AIAA Paper 1988-4359, 1988.
- [63] A. Shmilovich, Y. Yadlin, and E. Whalen. Active Flow Control Computations: From a Single Actuator to a Complete Airplane. *AIAA Journal*, 56(12):4730–4740, 2018.
- [64] A. Shmilovich and E. Whalen. A Technique for Low Input Flow Control Actuation. AIAA Paper 2017-3040, 2017.
- [65] A. Shmilovich, Y. Yadlin, and E. Whalen. Computational Evaluation of Flow Control for Enhanced Control Authority of a Vertical Tail. *AIAA Journal*, 54(8):2211–2220, 2016.
- [66] K. E. Jansen, M. Rasquin, J. A. Farnsworth, N. Rathay, M. C. Monastero, and M. Amitay. Interaction of a Synthetic Jet with Separated Flow over a Vertical Tail. *AIAA Journal*, 56(7):2653–2668, 2018.
- [67] T. Gerhold. Overview of the Hybrid RANS Code TAU. In N. Kroll and J. Fassbender, editors, *MEGAFLOW — Numerical Flow Simulation for Aircraft Design*, volume 89 of *Notes on Numerical Fluid Mechanics and Multidisciplinary Design*, pages 81–92. Springer, 2005.

- [68] D. Schwamborn, T. Gerhold, and R. Heinrich. The DLR TAU-code: Recent Applications in Research and Industry. In *Proceedings of the ECCOMAS 2006 CFD Conference*, The Netherlands, September 2006. ISBN: 90-9020970-0.
- [69] DLR. Technical Documentation of the DLR TAU-Code — Release 2015.1.0. DLR Technical Report, Institut für Aerodynamik und Strömungstechnik, 2015.
- [70] T. Knopp. The Actuation Boundary Condition for Flow Control in the DLR TAU Code. Technical Report IB-Nr. 224-2010 A44, 2010.
- [71] A. Jameson. Time Dependent Calculations Using Multigrid, with Applications to Unsteady Flows Past Airfoils and Wings. AIAA Paper 91-1596, 1991.
- [72] P. R. Spalart and S. R. Allmaras. A One-Equation Turbulence Model for Aerodynamic Flows. AIAA Paper 92-0439, 1992.
- [73] M. L. Shur, M. K. Strelets, A. K. Travin, and P. R. Spalart. Turbulence Modeling in Rotating and Curved Channels: Assessing the Spalart-Shur Correction. *AIAA Journal*, 38(5):784–792, 2000.
- [74] K.-C. Pfingsten, C. Jensch, K. W. Körber, and R. Radespiel. Numerical Simulation of the Flow around Circulation Control Airfoils. In *Proceedings of the 1st CEAS European Air and Space Conference*, Berlin, Germany, 2007. CEAS Paper 2007-377.
- [75] B. J. Daly and F. H. Harlow. Transport Equations in Turbulence. *The Physics of Fluids*, 13(11):2634–2649, 1970.
- [76] A. Kröhnert. Numerical Investigation of Tangential Blowing at the Rudder of a Vertical Tailplane Airfoil. AIAA Paper 2014-2143, 2014.
- [77] CentaurSoft. Centaur Hybrid Grid Generation System. Information and documentation online at <http://www.centaursoft.com>. Visited May 1st, 2020.
- [78] J. L. Thomas and M. D. Salas. Far-field boundary conditions for transonic lifting solutions to the Euler equations. *AIAA Journal*, 24(7):1074–1080, 1986. <https://doi.org/10.2514/3.9395>.
- [79] V. Ciobaca, T. Kühn, R. Rudnik, M. Bauer, B. Gölling, and W. Breitenstein. Active Flow-Separation Control on a High-Lift Wing-Body Configuration. *Journal of Aircraft*, 50(1):56–72, 2013.
- [80] L. F. Richardson. The Deferred Approach to the Limit. In *Philosophical Transactions of the Royal Society of London, Series A: Mathematical and Physical Sciences*, volume 226, pages 299–361. The Royal Society, 1927.
- [81] P. J. Roache. *Verification and Validation in Computational Science and Engineering*. Hermosa Publishers, Albuquerque, New Mexico, 1998.
- [82] J. Kirz. *Numerische Strömungssimulation von Schlitzvariationen bei tangentialem Ausblasen über dem Ruder an einem gepfeilten Seitenleitwerk unendlicher Streckung*. Master Thesis (supervised by the author), Technische Universität Braunschweig, Institute of Fluid Mechanics, Braunschweig, Germany, 2016.

- [83] Military Standard Gage Inspection. MIL-STD 120, Munitions Board Standard Agency, Department of Defence, Washington D. C., USA, 1950.
- [84] R. Swanson, C. Rumsey, and S. Anders. Progress Towards Computational Method for Circulation Control Airfoils. AIAA Paper 2005-0089, 2005.
- [85] V. M. Singh and P. Scholz. Circulation Control Experiments on a Vertical Tail. In R. Radespiel and R. Semaan, editors, *Fundamentals of High Lift for Future Civil Aircraft*, volume 145 of *Notes on Numerical Fluid Mechanics and Multidisciplinary Design*, pages 107–122. Springer, 2021.
- [86] J. B. Barlow, W. H. Rae, and A. Pope. *Low-Speed Wind Tunnel Testing*. John Wiley & Sons Inc., New York, USA, 1999.
- [87] V. M. Singh and P. Scholz. Measurements on a Vertical Tail with Vane Vortex Generators. In *Proceedings 66. Deutscher Luft- und Raumfahrtkongress*, Munich, Germany, September 2017.
- [88] V. M. Singh and P. Scholz. Circulation Control Experiments on a Vertical Tail. Presentation, Final Symposium of the Collaborative Research Centre 880, Braunschweig, Germany, December 2019.
- [89] K.-C. Pfingsten and R. Radespiel. Experimental and numerical investigation of a circulation control airfoil. AIAA Paper 2009-533, 2009.
- [90] Y. Liu, L. N. Sankar, R. J. Englar, K. K. Ahuja, and R. Gaeta. Computational Evaluation of the Steady and Pulsed Jet Effects on the Performance of a Circulation Control Wing Section. AIAA Paper 2004-56, 2004.
- [91] M. Burnazzi and R. Radespiel. Design of a Droopnose Configuration for a Coanda Active Flap Application. AIAA Paper 2013-0487, 2013.
- [92] A. Shmilovich, Y. Yadlin, E. D. Dickey, P. M. Hartwich, and A. Khodadoust. Development of an Active Flow Control Technique for an Airplane High-Lift Configuration. AIAA Paper 2017-0322, 2017.
- [93] A. Seifert and L. G. Pack. Oscillatory Control of Separation at High Reynolds Numbers. *AIAA Journal*, 37(9):1062–1071, 1999.
- [94] A. Kröhnert. Numerical Investigation of Unsteady Tangential Blowing at the Rudder of a Vertical Tailplane Airfoil. In A. Dillmann et al., editor, *New Results in Numerical and Experimental Fluid Mechanics X*, volume 132 of *Notes on Numerical Fluid Mechanics and Multidisciplinary Design*, pages 39–49. Springer, 2016.
- [95] V. Ciobaca and J. Wild. An Overview of Recent DLR Contributions on Active Flow-Separation Control Studies for High-Lift Configurations. *Journal AeroSpaceLab*, (6):1–12, 2013.
- [96] A. Gebhardt and J. Kirz. Numerical Investigation of Slot Variations on the Efficiency of Tangential Blowing at a Vertical Tailplane with Infinite Span. *CEAS Aeronautical Journal*, 9(1):195–206, 2018.

-
- [97] A. Gebhardt and J. Kirz. Numerical Investigation of Slot and Configuration Impact on the Efficiency of Tangential Blowing at a Vertical Tailplane with Infinite Span. In A. Dillmann et al., editor, *New Results in Numerical and Experimental Fluid Mechanics XI*, volume 136 of *Notes on Numerical Fluid Mechanics and Multidisciplinary Design*, pages 3–14. Springer, 2018.
- [98] A. Gebhardt. Numerical Investigation of Tangential Blowing over the Rudder of a Vertical Tailplane. *CEAS Aeronautical Journal*, 11(2):487–499, 2020. DOI 10.1007/s13272-019-00427-9.
- [99] D. Küchemann. A Simple Method for Calculating the Span and Chordwise Loading on Straight and Swept Wings of any Given Aspect Ratio at Subsonic Speeds. R & M No. 2935, 1956. A.R.C. Technical Report.
- [100] J. C. Lin, E. A. Whalen, M. Y. Andino, E. C. Graff, D. S. Lacy, A. E. Washburn, M. Gharib, and I. J. Wygnanski. Full-Scale Testing of Active Flow Control Applied to a Vertical Tail. *Journal of Aircraft*, 56(4):1376–1386, 2019.
- [101] A. Shmilovich and Y. Yadlin. Traverse Actuation Method. AIAA Paper 2016-3309, 2016.